Mass Transport in Single Nanopores

Towards a One-Dimensional State of Neutral Matter

René Michel Savard

Department of Physics
McGill University
Montréal, Québec, Canada

December 2014

Under the supervision of Professor Guillaume Gervais

A thesis submitted to McGill University in partial fulfillment of the requirements for the degree of Doctor of Philosophy.

In Knudsen we trust

ACKNOWLEDGEMENTS

First, I want to extend my gratitude to some of my colleagues whose contribution is overlooked by the author lists of publications and presentations. I simply could not have completed my research without them. Jean-Philippe Massé, from the CM^2 at the École Polytechnique de Montréal, has allowed us to quickly optimize the sample fabrication. He has systematically offered us his services on very short notice and supported us during long troubleshootings, and with our out-of-the-ordinary requests with the transmission electron microscope, focused ion beam and other characterization tools. From the McGill Nanotools Microfab, the team led by Matthieu Nannini and Don Berry gave us key insights to help us get out of seemingly inextricable meanders with the membranes and nanopores. The next person in this list is Pascal Brouseguin, manager of the *McGill Machine Shop*, a patient teacher of his craft and an invaluable colleague to bounce ideas with on all hardware designs. Pascal gave me concrete proof that rushing into fabrication never pays off.

I want to recognize the support the Department of Physics has provided to our group through the facilities and staff of the Center for the Physics of Materials (CPM). To a large extent, this means the help from Richard Talbot, Robert Gagnon and John Smeros. Without regard to his very busy schedule, Richard has always been ready to brainstorm and help me come up with the creative solutions required to make research go forward. Within a moment's notice, I could always count on Robert to assist me with new technical procedures or pick his brains about diverse materials-science techniques. John was always ready to lend me that extra hand for all the handy-work with our

capricious equipment.

I want to thank James Hedberg for his artistic acumen and the way he allowed me to learn, through *intellectual osmosis* and tactful criticism, that attention to details is crucial when you display your data. Two other "lab mates" that deserve my thanks are Benjamin Schmidt and Matthieu Bonin, who were available, day or night, for anything from a quick chat about physics or, more importantly, for motivational support in harder times.

I would also like to thank the many students working directly at my side. First off, Charles Tremblay-Darveau, for his support with sorting out the relevant theoretical framework to use in those early days when I barely understood my experiments. Then Guillaume Dauphinais, for his impressive investigation of nanopore stability and the countless hours he spent becoming our in-house expert on nanopore fabrication. I also thank Sam Neale for being a true lab partner through difficult episodes of our common projects and for his rigorous work ethics in all aspects of laboratory work. Finally, I thank Pierre-François Duc, for his invaluable help with automating data acquisition and making long experiments more manageable.

The last, but certainly not least, of the colleagues I want to thank is my supervisor. Against all odds, Guillaume remained true to his *motto*: "In Gervais' lab, ask for forgiveness, not permission". The truly collaborative and intense atmosphere fostered in his group has allowed me to thoroughly enjoy research, even on late nights and week-ends. As a supervisor, he strove to foster my critical thought processes when looking at any data and supported me through my development as a researcher. Guillaume also trusted me with

all aspects of the project allowing me to gain experience in several areas seldom available to students. This wholistic approach to his supervision is a rare gift I am very fortunate to have received.

I also acknowledge the financial support from the *Natural Sciences and Engineering Research Council of Canada* (NSERC), from the *Fonds de Recherche du Québec - Nature et Technologies* (FRQNT), and from S. Schulich through the fellowships in his name.

ABSTRACT

A mathematical description of one-dimensional (1D) many-body systems has been available for several decades in the form of the Tomonaga-Luttinger Liquids model. The technical means to engineer these 1D systems in the laboratory have, however, only become available recently. Experiments with confined electrons in quantum wires and with anisotropic clouds of cold atoms have yielded promising results, but limitations on the nature and density of these particles have prevented some experimental conditions to be attained. Given this, our purpose here is to develop a new experimental scheme to study the physics of Luttinger Liquids under conditions outside the reach of other methods.

In order to achieve this, we investigated the mass flow of helium through solid-state nanopores. Using a highly-focused electron beam, we fabricated these nanopores by locally ablating the surface of thin silicon nitride membranes. This tailored approach gave us the ability to produce nanopores as small as ∼0.5 nm in diameter. We induced flows of helium through these pores by applying a pressure differential, as large as 50 bar, and we measured the flow by mass spectroscopy.

The first results I present in this thesis were taken in the gas phase, at a temperature between 77 and 295 K. In order to demonstrate the feasibility of the detection of mass flow through single nanopores, we investigated the conductance of pores in a wide range of diameters, from over 100 nm down to ∼15 nm. We showed how the fluid undergoes a transition from free-molecular Knudsen effusion to a collective viscous flow as the mean-free-path of the

helium decreases. Modeling of the mass flow is shown to be an accurate method to quantitatively determine the dimensions of nanopores and thus provides an *in situ* tool for subsequent experiments at lower temperatures.

In the second half of this thesis, I present our low-temperature results on the flow of liquid helium in nanopores with diameters of 45 and 16 nm. For all samples, we detected the onset of superfluidity as a sudden rise in the flow. Using a two-fluid model of helium, we extracted the superfluid component of the flow by substracting the contribution of the normal component calculated with a short-pipe viscous flow equation. This superfluid contribution to the flow was assumed to be moving at a critical velocity. We found this critical velocity to be nearly linearly-dependent on temperature and with amplitudes as large as 20 m/s. These are the largest velocities measured in channel flows of superfluid, as well as the smallest pores used for strictly direct-current measurements.

Recent quantum Monte Carlo simulations predict the emergence of Luttinger Liquid behavior in solid-state nanopores only a factor of five smaller than our smallest successful sample. Our experiments therefore represent a significant step towards a realization of 1D systems of spinless neutral condensed matter particles. Our experimental scheme is also ideally positioned to compare the behaviour of ^{3}He and ^{4}He and thereby investigate the disappearance of bosonic and fermionic quantum statistics in 1D.

ABRÉGÉ

Une description mathématique des systèmes à plusieurs corps unidimensionnels (1D) a été disponible depuis plusieurs décennies sous la forme du modèle des liquides de Tomonaga-Luttinger. Les moyens techniques pour effectuer l'ingénierie de ces systèmes 1D en laboratoire ne sont cependant devenu disponible que récemment. Des expériences utilisant des électrons confinés dans des fils quantiques, ou encore des nuages anisotropes d'atomes froids, ont produit des résultats prometteurs, mais certaines limitations sur la nature et la densité de ces systèmes de particules ont empêché l'atteinte de certain régimes expérimentaux. De ce fait, notre but ici est de développer un nouveau procédé pour l'étude de la physique des liquides de Luttinger dans des conditions hors d'atteinte des autres méthodes.

Pour ce faire, nous avons investigué l'écoulement massique d'hélium à travers des nanopores fait de matière solide. En utilisant un faisceau hautement-focalisé d'électrons, nous avons fabriqué ces nanopores en effectuant une ablation locale de la surface de membranes minces de nitrure de silicium. Cette méthode nous a donnée la capacité de produire des nanopores aussi petit que $\sim$0.5 nm de diamètre. Nous avons ensuite induit un écoulement d'hélium à travers ces pores en appliquant un différentiel de pression, jusqu'à 50 bar, et avons mesuré cet écoulement massique par spectroscopie de masse.

Les premiers résultats que je présente dans cette thèse ont été obtenus dans la phase gazeuse, à une température entre 77 et 295 K. De manière à démontrer la faisabilité de la détection d'un écoulement massique à travers un trou unique, nous avons investigué la conductance de pores de diamètres très variés, de 100

nm à ∼15 nm. Nous avons montré comment le fluide passe par une transition entre une effusion Knudsen de particules libres à un écoulement collectif visqueux lorsque la libre-parcours-moyen d'hélium rapetisse. Nous avons démontré que la modélisation de cet écoulement massique est une méthode précise pour déterminer quantitativement les dimensions de nanopores et qu'elle offre ainsi un outil *in situ* pour les expériences subséquentes à basses températures.

Dans la seconde moitié de cette thèse, je présente nos résultats à basse température des écoulements d'hélium liquide dans des nanopores ayant un diamètre de 45 et 16 nm. Dans les deux cas, nous avons détecté l'émergence de la superfluidité sous la forme d'une augmentation soudaine de l'écoulement. En utilisant un modèle à deux-fluides de l'hélium, nous avons extrait la composante superfluide de l'écoulement en soustrayant la contribution normale calculée avec une équation d'écoulement visqueux dans des tuyaux-courts. Nous avons pris pour acquis que cette contribution superfluide de l'écoulement se déplaçait à une vitesse critique. Nous avons trouvé que cette vitesse critique dépendait presque linéairement sur la température et que son amplitude pouvait être aussi large que 20 m/s. Ce sont les vitesses les plus larges mesurée pour des écoulements superfluides dans des canaux. Ce sont, de plus, les nanopores les plus petits ayant été utilisés pour des mesures de courant directes.

Récemment, des simulations Monte Carlo quantiques ont prédi l'émergence de comportements de liquide de Luttinger dans des nanopores de matière solide à seulement un facteur cinq des dimensions de nos plus petits pores. Nos expériences représentent donc une étape importante vers la réalisation de

systèmes 1D pour des particules neutres sans moment angulaire dans la matière condensée. Notre procédé expérimental est, de plus, positionné idéalement pour comparer le comportement des atomes ^{3}He and ^{4}He et ainsi investiguer la disparition en 1D des statistiques quantiques tels que les bosons et fermions.

STATEMENT OF ORIGINALITY

This thesis contains work that is considered original scholarship and constitutes a genuine contribution to condensed matter physics. All results previously published are duly cited and the following list presents the contribution of authors:

- *Apparatus:* The author (MS) performed the design of all experimental cells with the help of Guillaume Gervais (GG). MS and GG designed the experimental procedure and MS perfomed the implementation of the measurement apparatus. Filters and other customized components of the gas handling system were, in large part, machined, designed and prepared by MS. While all the cooling-specific hardware of the cryostat was built by Janis Inc., other parts required for mass flow measurement, including thermometry and heat sinking components, were mounted and built by the author. The details of the equipment and components are presented in chapter 4.

- *Sample preparation:* The silicon nitride membranes were purchased as ready-to-use substrates and the drilling/imaging of nanopores was accomplished either by students from our group or by the TEM technicians. Specifically, Charles Tremblay-Darveau (CTD) drilled the sample for the 45 nm nanopore used in the *Phys. Rev. Lett.* ***103****, 104502 (2009)* publication (chapter 5), and Guillaume Dauphinais (GD) drilled the sample used in the *Phys. Rev. Lett.* ***107****, 254501 (2011)* publication (chapter 6). MS handled the large majority of the nanopore preparation after fab-

rication, in particular the mounting within the experimental cells. Most sample fabrication explanations were presented in both publications and discussed in detail in chapter 4.

- *Gas flow measurements:* The author participated in all discussions on the elaboration of experimental protocols, on the interpretation of results and on the selection of experiments to perform. MS performed most data acquisition for the gas flow experiments as well as all data analysis for each sample. GD helped with measurements shown in last section of chapter 5. The characterization of the 101 nm sample and the modeling in the transition regime were published, with MS as first author (*Phys. Rev. Lett.* **103**, 104502 (2009)) and CTD contributed to the development of the theoretical model. This portion of the thesis represents a first demonstration of direct mass transport detection in single nanopores and our samples are the smallest ever studied in continuous channel flow experiments.

- *Superfluid measurement and critical velocities:* MS has performed the data acquisition and analysis for all samples in the superfluid and participated to all discussions on the interpretation of results with GG. Significant contributions to the field of quantum fluid transport include:

  - The smallest singular aperture ($\sim$15 nm) allowing a direct detection of superfluid transport.

  - The largest critical velocities observed in channel flow of superfluid helium.

- The elaboration of an experimental scheme capable of detecting mass transport in channels small enough to reach the 1D limit.

The superfluid flow results and other characterization of the 45 nm sample were published as original work, again with MS as first author (*Phys. Rev. Lett.* **107**, 254501 (2011)).

Contents

List of Figures

Chapter 1

Introduction

This thesis constitutes the first few chapters of a larger body of work aimed at unraveling the physics of a one-dimensional (1D) system in the quantum regime. The ultimate goal is to find a suitable solid state system to confine test particles in a way for them to experience one-dimensional confinement. Specifically, any measurement of the properties of a one-dimensional quantum system is of great importance to determine whether the longstanding theoretical prescriptions given by Tomonaga-Luttinger liquids theory indeed constitute a viable model.

In the search for materials where one-dimensional quantum systems could be realized, promising results have been obtained with electrons propagating in carefully engineered materials. These heterogeneous crystalline substrates allow charge carriers to propagate in very thin regions and the application of additional electric fields can further restrict the areas accessible to the carriers, such that they can be confined to narrow transport channels. Transport of electrons in sufficiently narrow channels is expected to lead to behavior

described by the Tomonaga-Luttinger liquids theory [1].

Electrons in a semiconductor structure are however not the only test particle that can be confined to low dimensions. In fact, recent studies [2, 3] have shown, using quantum Monte Carlo simulations, that neutral atoms confined in a solid state nanopore can interact such that key parameters of the Tomonaga-Luttinger theory can be extracted. These computations were inspired by the experimental work described here and have predictive power in the limit where one-dimensional behavior is expected to occur.

The atom of choice for these experiments is helium, in large part because its large zero-point motion prevents solidification, even at zero Kelvin, thus allowing experiments with a strongly interacting quantum liquid. Helium is also available as two isotopes (^{4}He and ^{3}He), which are respectively bosons and fermions. Helium thus offers the promising possibility to conduct an experiment with either one of the atomic species, and compare behavior of particles with fundamentally different quantum statistics.

1.1 Outline of the Thesis

The overarching goal of the experiments presented in this thesis is to implement an experimental scheme where helium atoms would be confined in solid state nanopores and their physical properties probed by measurement of the mass transport. Chapter 2 presents the motivations behind this work as well as a broad overview of the history of theoretical investigations of physical systems confined to a single dimension. The prevalent experimental attempts to create a tangible 1D system are also described, as well as a comparison of their

strengths and weaknesses with respect to our proposed experimental scheme. The different avenues available to manufacture a highly confined system are also discussed, along with the rationale behind the choice of the solid state nanopores used in this thesis. Selected results from extensive computational studies by our collaborators are also presented in order to offer strong quantitative expectations.

The subsequent chapter is designed to lay down the theoretical background necessary to complete the analysis of the mass transport in channels. First, I describe the dynamics of fluid in the different flow regimes as it transitions from a rarefied effusion to a high density viscous flow. A hydrodynamic model tailored to the particular geometry of solid-state nanopores is also developed. Second, I give a simple description of the characteristics of helium at low temperatures and provide the key knowledge for the interpretation of liquid and superfluid helium transport.

In chapter 4, I describe the experimental techniques and apparatus required to implement our measurement scheme. Special attention is given to the sample fabrication process and how it influences the nanopore geometry. Indeed, the specific dimensions of the nanopores directly affect the interpretation of the results obtained. The principles underlying our main measurement tool, namely a helium mass spectrometer, are then presented alongside a description of the experimental equipment developed for the sensitive detection of helium flows. A specific section is also devoted to the cryogenic aspect of the experiments since working at low temperatures imposes several stringent constraints on the design of an experimental cell and on the protocol of exper-

iments. The chapter ends with a description of the thermometry apparatus and thermalization hardware designed for experiments at low temperatures.

The following two chapters are devoted to the presentation of selected experimental data and results we obtained throughout our investigations. The first is composed of results from gaseous flow of helium and serves as a stepping stone for the understanding of the liquid flow experiments presented in the chapter that follows. The gas flow results of chapter 5 first focus on experiments with large nanopores, acting as a proof-of-concept for the experimental scheme proposed here. Then, a series of experiments that slowly bridge the gap towards the quasi-1D regime is shown for increasingly small nanopores.

Since the realization of a 1D quantum state requires both low temperatures and highly confined geometries, the results of chapter 6 are presented in two parts. First, I show results from experiments that probe the flow of liquid helium both in the normal and superfluid phase in a 45 nm pore where a fully 3D behavior is expected. Then, in order to approach the 1D limit, I present results from a nanopore of only ~ 15 nm across.

The results presented in both chapters 5 and 6 are then summarized and discussed with respect to future avenues of investigation opened up by this work. Finally, I also present in the appendix some critical results regarding the stability of solid-state nanopores. These preliminary findings are relevant to our efforts to reach the 1D limit.

Chapter 2

Motivation and Historical Context

2.1 Fermi Liquids

The many-body interactions between particles in physical systems are often the root of exotic phenomena that spark the interest of condensed matter physicists. Fermi liquid theory is an example of a theory which describes particles with non-negligible interactions and whose predictions have been rigorously tested experimentally. In Fermi liquid theory, the interactions between fermions cannot be ignored, which makes a simple microscopic description with independent particles unsuitable. Without those interactions, the many body system of fermions is simply described by the free-fermion gas model where, at T=0, the occupation $n(k)$ of all available energy levels is $n(k \leq k_F) = 1$ up to the Fermi level and $n(k > k_F) = 0$ above. This is depicted in figure 2.1A. In this non-interacting case, a single fermion can be taken from the Fermi sea

($k < k_F$) and excited into an unoccupied state above the Fermi level. At finite temperatures, this excitation to a higher energy state is only possible for particles near the Fermi energy.

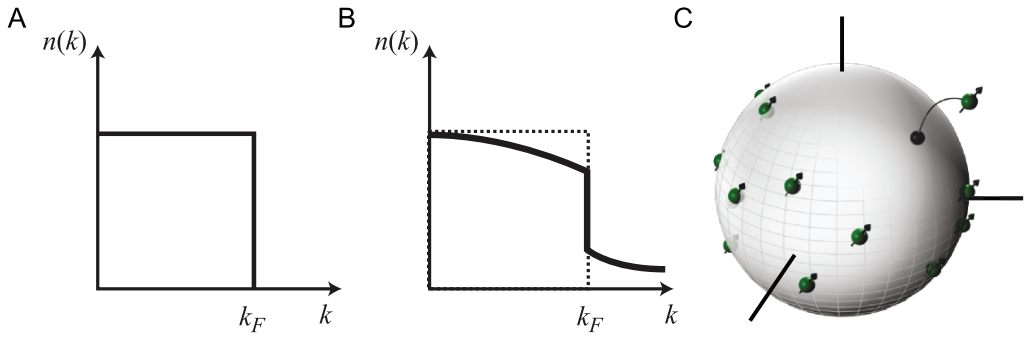

Fig. 2.1 (A) Occupation number of the 1D Fermi system of free electrons at T=0. (B) Occupation number with interactions between the constituent 1D fermions. (C) Schematic representation of the Fermi sphere in 3D where quasi-particles near the Fermi surface can be excited to higher levels. Parts (A) and (B) reproduced from [4].

The key insight behind Landau's Fermi liquid theory is the idea that relevant excitations of a physical system of interacting fermions are also restricted to particles with an energy near the Fermi level. When this is true, the system should be well described by a ground state, a filled Fermi sea (figure 2.1A,C) and a low energy spectrum of excitations near k_F. If the interactions are turned on gently enough (adiabatically), the system's excitations can be mapped one-to-one to the original interacting fermions. Importantly, these new mean-field quasi-particles are non-interacting and the Hamiltonian describing this redefined system is thus more easily solvable. These new quasi-particles are almost identical to the bare fermions except for a renormalization of some dynamical properties such as, for example, the effective mass. The occupation of

states $n(k)$ of a Fermi liquid (figure 2.1B) is thus very similar to that of the free-fermions model and the properties of the system are again defined by the quasi-particle excitations near the Fermi level. While Fermi liquid theory is, strictly speaking, an approximation, it "becomes an asymptotically exact solution for low energies" [5] and its predictions remain very powerful for most fermionic systems.

One dimensional (1D) quantum systems are, however, not well described by Fermi liquid theory. In fact, the Fermi liquid model breaks down in 1D because of a Peierls instability caused by the point-like Fermi surface. A single wavevector ($\pm 2k_F$) can connect the two points of the Fermi surface ($\pm k_F$) and this produces a divergent response under perturbations, so the mean-field description of the system is no longer applicable. A different approach is therefore required to describe the physics of strongly correlated 1D systems. Fortunately, a treatment of 1D interacting fermions similar to the Fermi liquid approach was devised decades ago and can be applied to a large class of 1D systems.

2.2 Tomonaga-Luttinger Liquids

In 1950, a model of interacting fermions in 1D was proposed by Tomonaga [6]. The model's assumptions were later redefined by Luttinger [7] and some subtle mistakes in calculations were eventually corrected by Mattis and Lieb [8] in the 1960s. The model for spinless and massless interacting fermions is constructed by using a bosonization of collective excitations to define a suitable Hamiltonian. Subsequent seminal work by Haldane on spinless 1D

fermions [9] introduced a generalized model giving insights into the dynamics of 1D systems in terms of interaction strength between the particles forming a 1D chain. Importantly, Haldane highlighted the possibility of treating several models of 1D interacting fermions or bosons with the same description of low energy excitations. The Tomonaga-Luttinger "liquid" was thus named in reference to the low-energy excitation of particles in the Tomonaga-Luttinger (TL) model [9]. The process is akin to the emergence of the Fermi liquid model from a modification of the free-Fermi gas model because of added interactions.

2.2.1 The Tomonaga-Luttinger Model

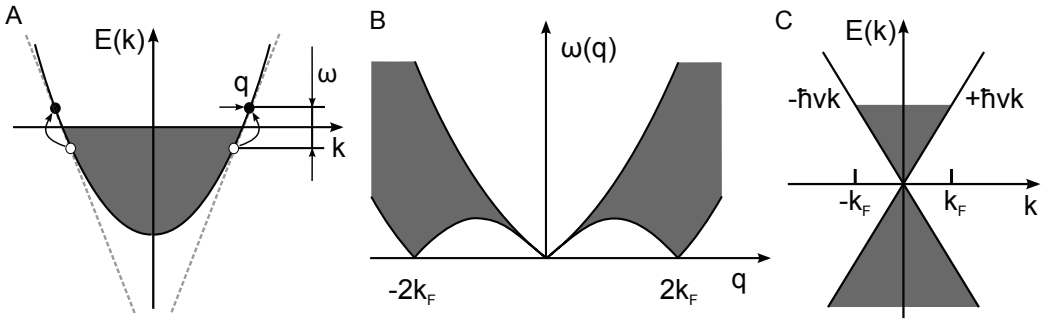

Fig. 2.2 (A) Dispersion relation of fermions in 1D. Particles are excited with momentum q and energy $E = \hbar\omega$ where the allowed excitation spectra (B) is gapless only for $q = 0, \pm k_F$. (C) The simplified dispersion relation assumed within the Luttinger model where the dotted lines in (A) depict the linear dispersion approximation at the region of interest for low-energy excitations exclusively. Two types of particles are presumed, right moving and left moving and the dispersion relation is assumed to be linear with $E = \pm\hbar v k$. Figure based on figures from [5], chapter 3.

The dispersion relation of a 1D fermionic systems is shown schematically in figure 2.2A, where fermions (full dot) can be excited above the filled Fermi sea, thus creating a hole (open circle). For low energy, this particle-hole excitation

is restricted to fermions near the two Fermi points at $\pm k_F$. The excitation spectrum is shown in fig. 2.2B where we note the important gap for $0 \leq q \leq 2k_F$, where the subscript "F" denotes the Fermi level and q is the momentum transfer during excitation. This feature emerges from the fact that the only processes that can excite fermions out of the Fermi sea are for $|q| = 0, 2k_F$ and leads to the nesting behavior alluded to in the previous section when discussing the instability of Fermi liquids in 1D.

The TL model is constructed based on assumptions about the dispersion relation of the fermions near $\pm k_F$. Specifically, the exactly solvable nature of the TL model relies on the linearized dispersion relation $E_r(|k|) \simeq \hbar(rk - k_F)v_F$ extending down to all lower energies (see figure 2.2C) and the presence of two types of particles, namely right ($r = +1$) and left ($r = -1$) moving ones. The dotted lines on figure 2.2A represent this linear simplification for the 1D fermions and figure 2.2C explicitly shows the linear dispersion relation of the TL model.

The Hamiltonian for this simplified system can be built in two parts [5]: the first interactionless Hamiltonian $\mathcal{H}_0$, and the interaction specific $\mathcal{H}_2$ and $\mathcal{H}_4$ such that

$$\mathcal{H}_{TL} = \mathcal{H}_0 + \mathcal{H}_2 + \mathcal{H}_4, \tag{2.1}$$

and

$$\mathcal{H}_0 = \hbar \sum_{r,k,s} v_F(rk - k_F) : c^\dagger_{rks} c_{rks} : \tag{2.2}$$

$$\mathcal{H}_2 = \frac{1}{L} \sum_{q,s,s'} \left[g_{2\parallel}(q)\delta_{s,s'} + g_{2\perp}(q)\delta_{s,-s'} \right] \rho_{+,s}(q)\rho_{-,s'}(-q) \tag{2.3}$$

$$\mathcal{H}_4 = \frac{1}{2L} \sum_{r,q,s,s'} \left[g_{4\parallel}(q)\delta_{s,s'} + g_{4\perp}(q)\delta_{s,-s'} \right] : \rho_{r,s}(q)\rho_{r,s'}(-q) : . \tag{2.4}$$

In the previous Hamiltonian $\mathcal{H}_{TL}$, the fermions described by the operators $c^\dagger_{rks}$ have two possible spin states s and propagate in one of two directions $r = +, -$ for right and left moving particles respectively. The system has length L and particles have momentum k up to the Fermi level. The terms within ": ... :" are normal ordered for fermionic operators. The interactions described by $\mathcal{H}_2$ and $\mathcal{H}_4$ are for four-fermions events where a momentum transfer q occurs and the coupling constants $g_2(g_4)$ have the usual meaning of forward scattering between particles of different(same) chirality[1]. The subscript "$_\parallel$" refers to same-spin interaction and the "$_\perp$" one refers to opposite-spins coupling. The Kronecker delta δ has the usual definition of $\delta = 1$ when indices are the same. The density fluctuation operators $\rho_{r,s} = \sum_k : c^\dagger_{r,k+q,s} c_{r,k,s} :$ define particle fluctuations with momentum q restricted to $2\pi m/L$ for an integer m given a finite length system.

The present form of the TL Hamiltonian hints at the nature of the excitations in 1D system being of bosonic nature. Given the previous assumptions about the dispersion of particle-hole pair excitations, the Hamiltonian can in fact be rewritten as a harmonic oscillator where the eigenstates are truly

[1] Chirality in this case refers to whether particles are left-moving or right-moving.

bosonic. This Bogoliubov transformation of the initial, fermionic states into operators with bosonic properties is the historical root of the term "bosonization". The details of the latter transformation of the Hamiltonian are presented in [5, 10].

Looking at the free-fermion case, some important insights can be obtained. The previous form of $\mathcal{H}_0$ in equation 2.1, is equivalent to

$$\mathcal{H}_0 = \frac{\pi\hbar v_F}{L} \sum_{r,q\neq 0,s} : \rho_{r,s}(q)\rho_{r,s}(-q) : + \, constant, \tag{2.5}$$

where any new excitation in the system is added above the Fermi level and this excitation adds a significant amount of kinetic energy to this Hamiltonian. The free-fermion Hamiltonian can be transformed to

$$\begin{aligned} \mathcal{H}_0 =& \frac{\pi\hbar v_s}{L} \sum_{r,q\neq 0,s} : \rho_{r,s}(q)\rho_{r,s}(-q) : \\ &+ \frac{\pi\hbar}{2L} \sum_{s} \left[v_N (N_{+,s} + N_{-,s})^2 + v_J (N_{+,s} - N_{-,s})^2 \right], \end{aligned} \tag{2.6}$$

where $N_{r,s} \equiv \rho_{r,s}$ measures excitations restricted to $q = 0$ and $v_s = v_N = v_J = v_F$ are propagation velocities for these free-fermions. The velocities were labeled differently to highlight the physical distinction for the symmetric combination of $N_s = \sum_r N_{r,s}$ representing charge excitations and the antisymmetric combination $J_s = \sum_r r N_{r,s}$ represents currents. This form of the Hamiltonian is especially insightful because of the introduction of different velocity-like variables v_J, v_N, and how it transforms upon addition of interaction in the model.

The introduction of interactions does not change much in the derivation, except that the bosons of choice in the Bogoliubov transformation are explicitly interpreted as combinations of charge (ρ) and spin (σ) collective fluctuations. The velocities of equation 2.7 are now altered by the coupling constants g_2 and g_4 and the full TL Hamiltonian becomes

$$\begin{aligned}\mathcal{H}_{TL} = \; & \frac{\pi\hbar}{L}\sum_{r\nu q\neq 0} v_\nu(q) : \nu_r(q)\nu_r(-q) : \\ & + \frac{\pi\hbar}{2L}\left[v_{N_\nu}(N_{+\nu}+N_{-\nu})^2 + v_{J_\nu}(N_{+\nu}-N_{-\nu})^2\right],\end{aligned} \tag{2.7}$$

where $\nu = \sigma, \rho$ and the collective excitation velocity becomes

$$v_\nu(q) = \sqrt{\left[v_F + \frac{g_{4\nu}(q)}{\pi}\right]^2 - \left[\frac{g_{2\nu}(q)}{\pi}\right]^2}, \tag{2.8}$$

with $v_{N_\nu}v_{J_\nu} = v_\nu^2$ and $v_{N_\nu} = v_\nu/K_\nu$. The conclusion of this derivation is that interactions between the particle-hole pairs renormalize the velocity of the collective excitations and the velocity (v_ρ) for charge propagation is no longer the same as (v_σ), the spin propagation velocity. This separation of two distinct propagating modes is the well known "spin-charge separation". The parameter K_ν is directly affected by the coupling constants and is sometimes described as the stiffness of the 1D system because it regulates the decay of most correlation functions. Because of its central role in describing the dynamics of excitations within the TL model, it is often called the "Luttinger parameter". Since we will not work with a spin degree of freedom in the rest of this work, we will drop the subscript and only write the Luttinger parameter as K.

2.2.2 A Class of Luttinger Liquids

In his seminal contribution on this subject [9], Haldane recognized that the construction of a harmonic-fluid description to solve electronic 1D systems could be extended to a whole class of interacting particles in highly confined configurations. In fact, the bosonization of 1D systems treats both fermions and bosons similarly and the dynamics of the hydrodynamics of the low-energy excitations can be described by the Hamiltonian derived above [11]. The long-range density fluctuations emerge in all cases and their propagation is described by the velocity v and the Luttinger parameter K. Of particular interest to us is the case of spinless bosons interacting with realistic inter-atom potentials [12]. Using the same derivation as the one shown in the previous section, we can arrive at a very informative effective Hamiltonian [2]

$$\mathcal{H} = \frac{\hbar}{2\pi} \int_0^L dz \left[v_J (\partial_z \phi)^2 + v_N (\partial_z \theta)^2 \right], \tag{2.9}$$

or equivalently

$$\mathcal{H} = \frac{\hbar v}{2\pi} \int_0^L dz \left[\frac{1}{K} (\partial_z \phi)^2 + K (\partial_z \theta)^2 \right], \tag{2.10}$$

where the velocity $v = \sqrt{v_J v_N}$ defines the linearly dispersed density modes with $E(k) = \hbar v k$ and the two phases $\phi(z)$ and $\theta(z)$ are defined by the particle field operator $\psi^\dagger = \sqrt{\rho(z)} e^{-i\phi(z)}$. The angular field $\theta(z)$ is a suitable redefinition of the density, such that

$$\rho(z) \equiv \left[\rho_0 + \frac{1}{\pi} \partial_z \theta(z) \right] \sum_{m=-\infty}^{\infty} e^{i2m\theta(z)}.$$

ρ_0 is defined as the T=0 number density. $\partial_z\theta(z)$ is the canonically conjugate momentum to $\phi(z)$ and they must commute as $[\phi(z), \partial_{z'}\theta(z')] = i\pi\delta(z - z')$. The position z is set along the axis of the 1D system and the particle confinement would be applied perpendicular to it. We will return to these equations in section 2.5, where the convenient quadratic structure of the TL effective Hamiltonian will allow for computation of the density-density correlations, leading to predictions of physically measurable quantities.

In most 1D systems, the density correlation functions show a tendency to form density waves, and in particular those correlation functions decay according to power laws that are proportional to the interaction strength between particles. These strong predictions of the similarity of behavior between systems of any quantum statistics and the power-law decay of physical quantities as a function of interaction strength are key signatures for experiments to observe [11]. A few strategies have been explored over the last two decades to implement and measure such 1D systems. The most prominent ones are described in the next section.

2.3 Realizations of 1D Systems

The interest in Tomonaga-Luttinger liquids (TLL) has been largely theoretical for decades and it is only recently that several techniques have allowed for experimental realizations of quasi-1D systems in the laboratory. At its simplest, a 1D quantum system can be created experimentally if test particles can be confined along two axis and remain free to propagate in the third dimension. The application of this confinement potential gives rise to subbands in

the off-axis directions and if the energy of the particles is low enough, motion perpendicular to the free axis is quenched. This remains true for different particles and for various confinement fields, as long as the energy of the particles is lower than those transverse energy levels. There are therefore many physical systems where a realization of a 1D quantum systems could be attempted and groups from several fields have indeed pursued it. For example, early evidence of 1D behavior has been observed in electron gases within semiconducting heterostructures [13, 14, 15, 16, 17], in optical lattices of cold vapor gases [18, 19, 20, 21] and in the T-linear signature of the phonon heat capacity of helium within porous materials [22]. An overview of some of the work done in each of these avenues follows.

2.3.1 Electronic Transport in Quantum Wires

Electronic transport in condensed matter systems is a prime test bed for exotic physical phenomena, and it is therefore no surprise that attempts to detect signatures of TLL happened very early within this field. In particular, measurements [13, 23] of the current tunneling into the edge state of the fraction quantum Hall effect was found to be consistent with the presence of a chiral Luttinger liquid. Realizations of TLL in electronic transport experiments were also devised in systems where the conduction path was engineered to be of very small dimensions. Technically, these are quantum wires where transport is allowed in a limited number of conductance channels.

Using very narrow materials such as carbon nanotubes is one method of obtaining quantum wires [24, 25] where 1D behavior could be observed. A

second noteworthy approach uses confinement of electrons deep within semiconducting heterostructures. This strategy has evolved from the extensive expertise of groups working on two-dimensional electron gases (2DEG), where they can engineer stacks of carefully chosen semiconductors such that electrons are free to move along two directions. Metal gates are then positioned over this heterostructure such that applied voltages deplete the electronic density underneath them, and conduction paths can thus be patterned precisely. Figure 2.3 shows an exampleof such a construction designed in our group .

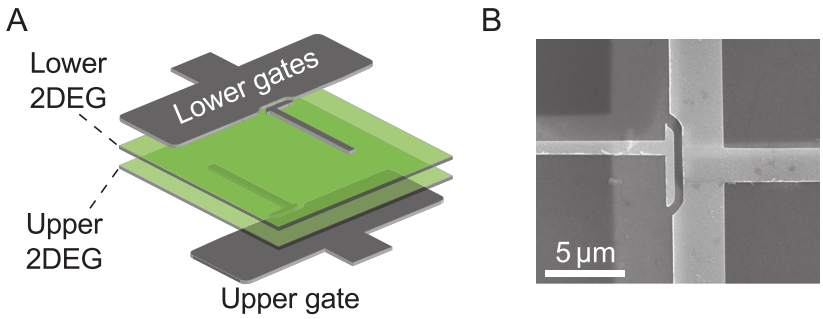

Fig. 2.3 (A) Schematic of the 2DEG within a semiconducting heterstructure (not shown here) and the metallic gates used to depleted the 2DEG in chosen areas. This geometry combines two vertically integrated quantum wires to study the drag signal between the two wires. (B) Scanning electron microscope image of a device. Figure reproduced in part from [26].

Quantum wires made from 2DEGs have evolved into several parallel strategies for the detection of signatures of the TLL. Resonant tunneling into a quantum wire made from the cleaved-edge of a 2DEG [15, 17, 27] has been a method of choice early on to observe TLL power-law behaviors. More recent attempts are using a slightly different approach. By engineering two closely spaced 2DEGs and placing gates such that a quantum wire is created in each

2DEG, the inter-wire interactions can be probed by measuring the Coulomb drag signal between them [26, 28].

Figure 2.3A shows a schematic based on a device where two 2DEGs separated by tens of nanometers each have a pair of metallic gates to shape a quantum wire. These two quantum wires are aligned vertically. Figure 2.3B is an electron microscope image of an actual device where the metallic gates (brighter areas) are clearly visible. These vertically integrated quantum wires (shown in figure 2.3) have been used to demonstrate that the temperature dependence of the Coulomb drag is consistent with having two parallel TLLs [29]. Using similar experimental techniques, other groups have reported the observation of charge fractionalization [30] and spin-charge separation [1, 31] in quantum wires. A more detailed account of the experimental realization of TLL with gated 2DEG systems can be found in the thesis of D. Laroche [32].

2.3.2 Laser Traps and Ultra Cold Atoms

Laser cooling and magneto-optical traps are experimental techniques that allow researchers to slow down atoms and cool them to extremely low temperatures. The optical trapping technique uses a retro-reflected laser beam that interferes with itself to create a standing wave. The atoms develop an induced polarization when interacting with this electric field, and consequently feel a force proportional to its gradient. The laser beam frequency is also tuned with respect to a specific atomic transition such that many photons interact with the atoms and the latter can eventually aggregate in a spacial lattice formed by the standing light pattern. If three such counter-propagating laser beams

are placed perpendicular to one another, then a 3D lattice is created where a dilute gas of atoms can be trapped.

The optical trap can be used in conjunction with a magnetic trap, where the spin of the atoms interacts with an applied magnetic field through the Zeeman effect. Various methods [20, 33] can be used here to magnetically confine the atoms, but the goal remains to trap the cooler atoms while letting the warm ones escape to the vacuum surrounding the trap.

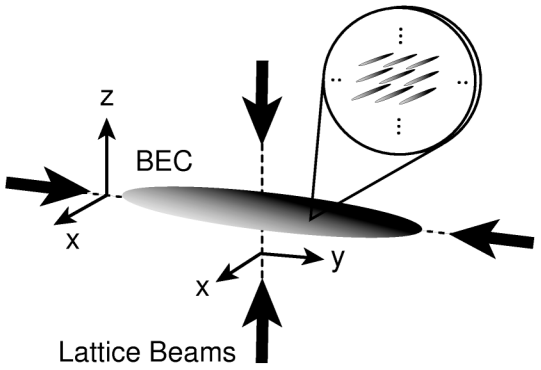

Fig. 2.4 Schematic representation of a 2D optical lattice. The cloud of cold gas is formed with perpendicular lasers beams, here shown as arrows, that create the electric fields forcing the trapping of atoms. (BEC stands for Bose-Einstein condensate). The inset shows how the cloud of atoms is divided in highly asymmetric, elongated "cigar" shaped regions arranged in a 2D lattice. Each "cigar" contains a few thousand atoms that are in a quasi-1D confined state. Reproduced from [18].

Figure 2.4 shows a simplified illustration of the vapor cloud created using magneto-optical traps. Within a vacuum chamber, the cold atoms are confined to the volume at the intersection of the laser beams (here shown as arrows). In this case, the intensity and frequency of the lasers was chosen to create a highly asymmetric trap such that atoms would be confined in a 2D lattice of smaller,

elongated "cigar shaped" traps. The few thousand atoms in each "cigar" are highly confined radially and are assumed to be in a quasi-1D lattice system. The possibility of using bosonic atoms and the inherent low temperatures of such cold gas clouds offers the opportunity to investigate 1D systems of interacting bosons [18, 19, 21] and explicitly test if the TLL description applies.

One key feature of magneto-optical traps is the ability to vary the potential depth that the atoms experience by modulating the intensity and frequency of the laser beams forming the lattice of potentials. It is thus possible, in principle, to effectively tune the interaction strength between atoms sitting in adjacent potential wells and, presumably, be able to observe the dynamics of 1D systems [34] for different Luttinger parameters and compare the results to TLL theory [33, 35, 36].

The tunability of interaction between the constituent particles of cold vapor gases is particularly effective when making a comparison between the many variations of microscopic models [12], such as the hard-core bosons of the Tonks-Girardeau gas or the generic Bose-Hubbard particles in a lattice. As opposed to electronic systems, the nature of inter-atom interaction is not Coulombic and is better described as a short-range interaction leading to weakly coupled system. The very nature of dilute gases imposes a limit on the density of particles accessible and the total sample size is restricted to mesoscopic dimensions. Realizations of bosonic 1D systems with higher densities, strong interactions and Galilean invariant (i.e. without the underlying lattice structure of cold gases) are still lacking [2]. A candidate substrate for the latter requirements is liquid helium confined in nanopores.

2.3.3 Helium Adsorbtion in Porous Media

In the quest for experimental realizations of TLL systems, some groups have investigated the adsorption of atoms inside and outside axi-symmetric porous materials. Porous materials such as zeolites can be chemically tailored to form large arrays of stacked tubes with diameters a only a few nanometers. These *nano*tubes can be very long and have fixed diameters since their chemical composition is the key factor determining their dimension. It is a favorable characteristic of these materials to be able to confine particles over long distances and thus, presumably, preserve the long-range properties of 1D systems.

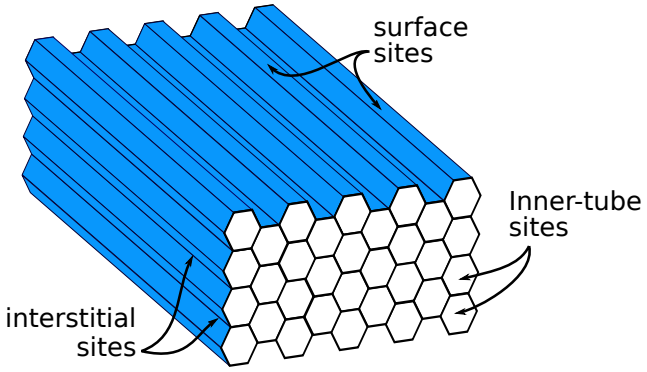

Fig. 2.5 Cartoon of zeolites used in adsporption experiments. The curled-up sheets form bundles of nanotubes with approximate hexagonal stacking. In this drawing, the length-to-diameter ratio is not representative of actual ratios in typical samples, and is depicted here in a very regular and ordered stack, which is an idealization of the actual structure of dry zeolite powder.

Zeolites can be readily synthesized in bulk and transformed to a dry precipitate of fully formed nanotubes (see cartoon in figure 2.5). This powder can then be used in experiments to adsorb atoms on the interstitial sites between adjacent nanotubes and, as is hoped, also within the core of the nanotubes

once all other adsorbtion sites are filled. Torsional oscillator studies of helium atoms adsorbed on such nanotube bundles have been performed and promising results of quasi-1D behavior have been obtained measuring the phonon dissipation in various zeolite geometries [37, 38]. Once again, it is worth mentioning that since these experiments are done with helium atoms as a test particle and ^{4}He is a boson, these experiments are complementary to those performed in electronic quantum wires.

It is important to note that experiments with zeolites are performed with a considerable volume of crushed nanotubes powder. This means that a sample consists of a very large total number of nanotubes, since each bundle can contain any number of them, and those nanotubes are of various dimensions, since each bundle differs greatly in length or width. Another challenge of using channels with a large distribution of sizes is that it is not immediately clear what is the ratio between adsorption sites on the surface of tubes and those sites of interest, where 1D confinement might be observed. Compounding this difficulty is the fact that sites on the surface of nanotubes are populated first and vastly outnumber the "potentially-1D" sites such as the groove between two nanotubes (interstitial sites) or inside the nanotube core (inner-tube sites) [39]. Any signal measured from a powder with *zillions* of tubes will always have a strong component emanating from the two-dimensional surfaces of both the experimental cell and the nanotube's outer surface. It is therefore challenging to extract results specific to the atoms in a quasi-1D state.

The intuitive solution to these challenges is to use a single nanotube. While the ratio of relevant signal over the overall measured signal would be much

more favorable in this case, the measurement techniques used in the torsional oscillator experiments would need to be several orders of magnitude more sensitive and it is therefore necessary to adopt another strategy.

2.4 Helium as a Paradigm

It is in the context of the emergence of the experiments presented in the last section that we attempted to devise a new experimental scheme that would allow us to avoid measurements averaging over a large distribution of nanotubes, but still have the sensitivity to detect signal from helium atoms propagating inside a single nanotube. The use of strongly-interacting particles, such as helium atoms in the liquid phase, is also an asset to complement the laser-trap experiments that use dilute gases. Finally, the ability to repeat an experiment with either fermions or bosons is a powerful tool to verify the predictions that Tomonaga-Luttinger liquids behavior is independent of quantum statistics. The two isotopes ^{4}He and ^{3}He are thus ideally suited for this purpose.

Indeed, helium has been a model system of choice for experiments carried out over a very broad range of conditions and its thermodynamic properties are available at all temperatures and pressures of interest here. Figure 2.6 shows the pressure-temperature phase diagram of ^{4}He with semi-logarithmic axes. The region labeled "He I" represents the liquid phase.

The large zero-point motion of the helium atoms prevents it from ever solidifying at low pressure (< 25 atm), which gives it the unique potential to transition to a quantum mechanically dominated phase at low temperatures: the superfluid phase. This second order phase transition to superfluidity is

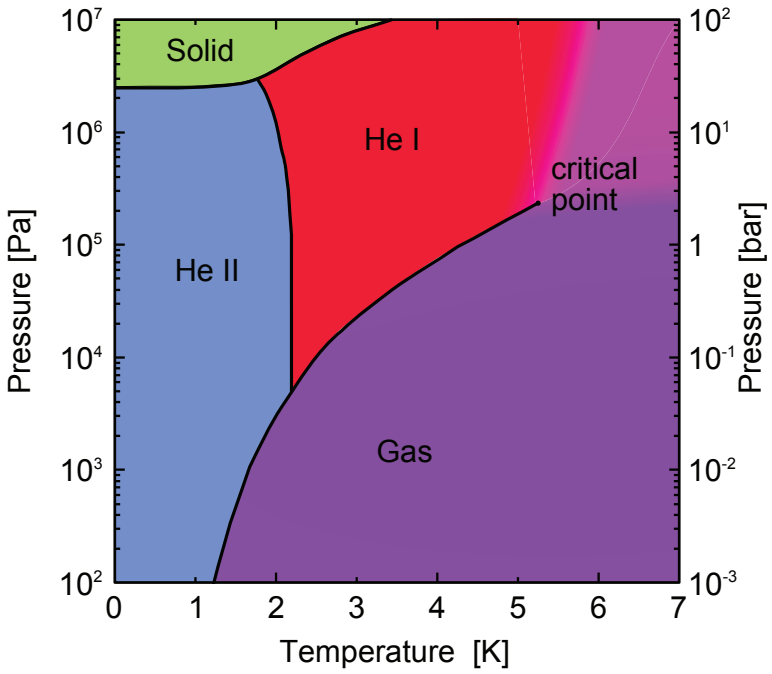

Fig. 2.6 Pressure-temperature phase diagram of bulk ^{4}He. The liquid phase is labeled "He I" and is bounded near 2.17 K by a nearly vertical phase transition line called the "λ-line". The transition over the λ-line leads to the "He II" region where superfluidity emerges. A unique property of helium is the absence of the solid phase at low temperature for pressures below ∼25 atm.

bounded in the P-T diagram by a line quizzically dubbed the "λ-line" due to the similarity between the shape of the ^{4}He specific heat curve and the Greek letter λ. The λ-line, and λ-temperature, are especially relevant in investigations of superfluids. For example, experiments with porous materials such as Vycor and Gelsil [40, 41, 42] found a suppression of superfluidity causing a lowering of the λ-line as a function of pore size. Given these characteristics, helium atoms are paradigm particles to study fluid transport at very low temperatures in highly confined systems [43, 44].

2.5 Quantum Monte Carlo Simulations

Our search for a suitable experimental system optimized to study strongly interacting one-dimensional states of matter is further supported by large-scale numerical simulations of ^{4}He filled nanopores [45]. In this work and in an earlier publication [46], Del Maestro and Affleck show results on large-scale quantum Monte Carlo (QMC) simulations of ^{4}He atoms exhibiting behavior consistent with TLL theory. The simulations used the path integral Monte Carlo method and a "Worm Algorithm" to efficiently explore the paths (worldlines) of each quantum particle evolution during the simulation. The model is built from a generic many-body Hamiltonian within an external potential V_{ext} and inter-particle interactions V_{int},

$$\mathcal{H} = \sum_{i=1}^{N} \left[\frac{-\hbar^2}{2M_{He}} \vec{\nabla}_i^2 + V_{ext}(\vec{r}_i) \right] + \sum_{i<j} V_{int}(\vec{r}_i - \vec{r}_j), \tag{2.11}$$

where the position of each of the N atoms is $\vec{r}_i$ and they have mass M_{He}. The symbol $h = 2\pi\hbar$ represents Planck's constant. In the latest series of simulations, great care was given to the choice of V_{int} and V_{ext}, and in particular, an Si_3N_4 boundary was selected to match as closely as possible the experimental conditions of the work in this thesis. The results of these simulations are considered "exact" in the sense that realistic particle-particle (V_{int}) and particle-wall (V_{ext}) interaction potentials are used and they can be computed for experimentally accessible pressures and temperatures.

One interesting finding from the averaged particle distribution within the nanopores is the formation of concentric shells as shown in figure 2.7. These

cylindrical shells start forming near the nanopore wall, where a large potential induces the formation of a layer of atoms at a distance determined by the minimum in the wall-particle interaction energy. The next layer forms when atoms settle on the first layer at a distance given by the helium-helium interaction potential. This effectively forms an inner cylindrical shell. If the radius of the nanopore is large, many layers can fit concentrically. For multiples of $\sim$3 Å, simulations show that there is sufficient space for an inner core to form in the middle of the nanopore, as can be seen in the insets of each graph in figure 2.7. For example, with a radius of 6 Å, there is one cylindrical sheet of atoms surrounding an inner core. The atoms located within that inner core were, in fact, found to be the best candidates to study the 1D system.

2.5.1 Comparison to the Luttinger Liquids Model

The results of the QMC simulations are then compared with predictions of the Tomonaga-Luttinger Liquid (TLL) model. Writing the bosonic many-body Hamiltonian of equation 2.11 in second quantized notation can help one see the emergence of the 1D signatures of the TLL model. We get

$$\mathcal{H} = \int_0^L dz \left[\frac{\hbar^2}{2M_{He}} \partial_z \Psi^\dagger(z) \partial_z \Psi(z) + \frac{1}{2} \int_0^L dz' \rho(z) V_{1D}(z - z') \rho(z) \right], \quad (2.12)$$

where the bosonic creation operator $\Psi^\dagger(z) = \sqrt{\rho(z)} e^{-i\phi(z)}$ has the usual commutation relation $[\Psi(z), \Psi^\dagger(z')] = \delta(z - z')$. We recognize the presence of the density operator $\rho(z)$ and the phase operator $\phi(z)$, and using the tools of section 2.2, we can easily return to the Hamiltonian shown in equation 2.9:

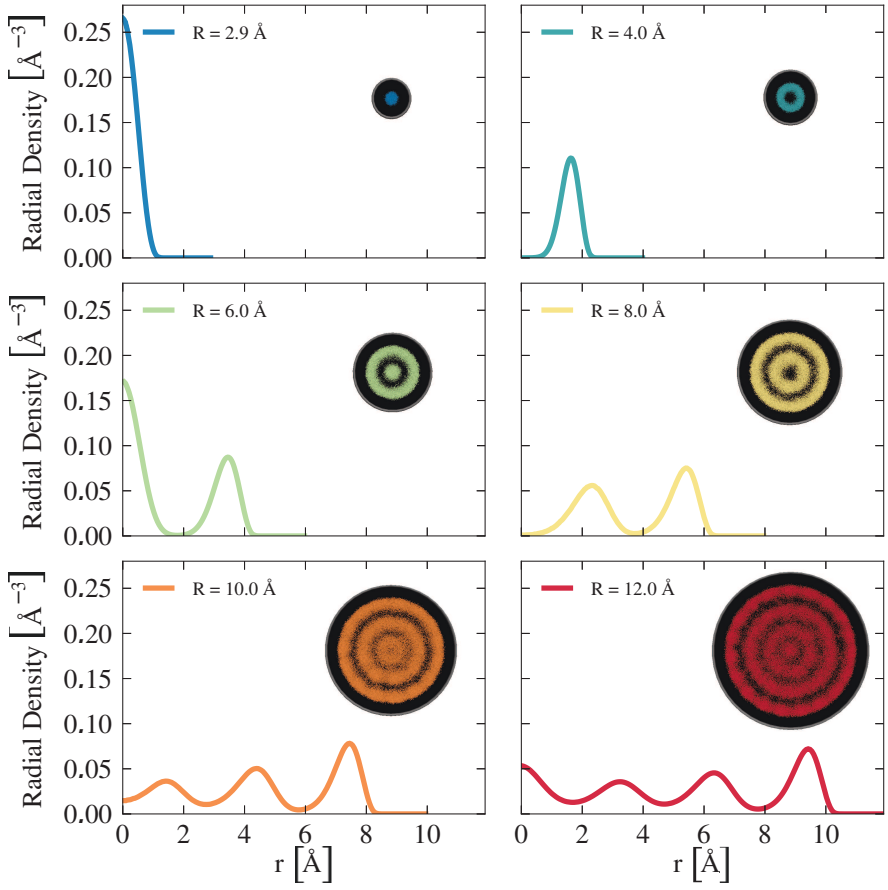

Fig. 2.7 Radial density of helium atoms inside nanopores of radius between 2.9 and 12 Å. Insets shows atoms on a black background seen looking along the nanopore axis. Reproduced from [2].

$$\mathcal{H}_{TLL} = \frac{\hbar}{2\pi} \int_0^L dz \left[v_J (\partial_z \phi)^2 + v_N (\partial_z \theta)^2 \right] . \tag{2.13}$$

The transformation of the interacting 1D boson Hamiltonian into a quadratic form has the immediate benefit that many thermodynamic quantities can be computed [2] from a very limited number of input parameters such as the temperature T, the propagation velocity v and the Luttinger parameter K.

For example, density correlations can be computed for the atoms within the inner cores and compared to predictions from TLL theory as seen in figure 2.8. The results of the fit of the Luttinger liquid theory to the QMC data show a strong tendency to form ordered density waves along the length of the nanopore for the smallest pores. The fit yields a value for the Luttinger parameter $K = 6.0(2)$, a value associated with a system with low interactions and a tendency to localize and develop density wave order (figure 2.8a).

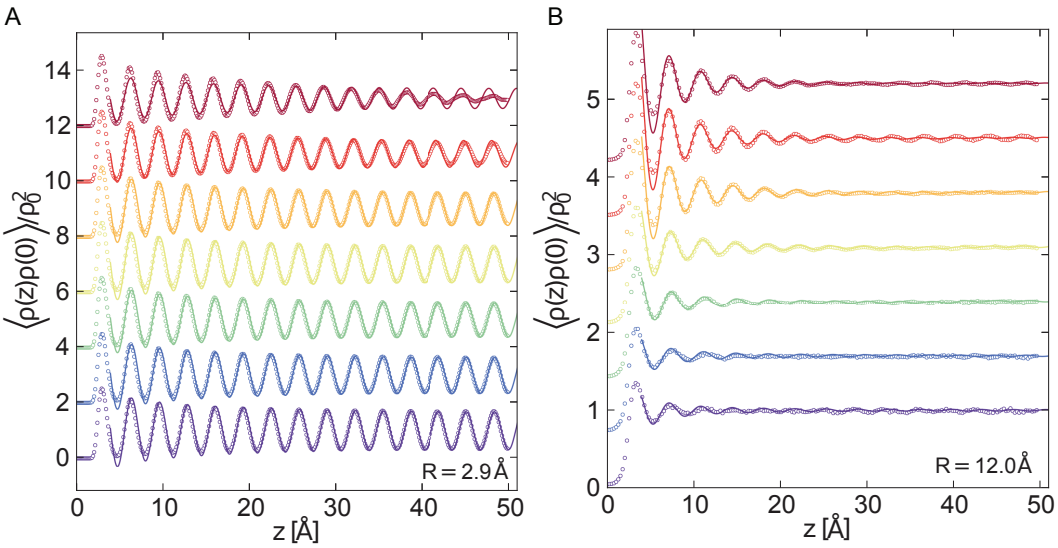

Fig. 2.8 Density correlation of helium atoms along the channel axis for a nanopore of radius R=2.9 Å (a) and R=12 Å (b). The decay of the long range order is characterized by an interaction that corresponds to Luttinger parameters K= 6.0 and 1.3 respectively. Curves are manually offset for clarity with the bottom data simulated at T=0.5 K increasing up to 2.0 K for the data at the top. Reproduced from [2].

The same analysis applied to the larger pore with radius 12 Å shows damped oscillations possibly due to inter-layer coupling increasing the effective interactions between atoms of the core. The increased effective interac-

tions between particles in the core channel are characterized by a fit parameter $K = 1.3(2)$ which describes a system incrementally dominated by superfluid fluctuations (see figure 2.8B). The smooth crossover from a phase dominated by fluctuations to one where density wave ordering is present is expected in TLL theory. The possibility of tuning the interaction strength by testing different pore sizes is thus an important asset to probe this crossover and determine whether or not a quantum phase transition occurs.

One important conclusion drawn from the results of density wave ordering as the pores decrease in size is that there is a decrease of the effective superfluid fraction within the pore correlated to the rise of density wave order, which may be observed experimentally. Indeed, experiments of transport through nanotubes are very sensitive to the emergence of superfluidity in liquid helium and represent, historically, a prominent method to determine the superfluid fraction of helium under different conditions (see for example review of superfluid helium in porous media [40]). As an example, Del Maestro has calculated in [2] that at 1.0 K the superfluid fraction inside the nanopore is close to 20%, where the vast majority of superfluid is in the inner core.

The measurement of the superfluid fraction within nanopores is particularly relevant to the experiments we developed in this thesis. Recent work by Kulchytskyy *et. al* [3] shows that QMC computation of helium within nanopores has a unique superfluid signature. Figure 2.9 shows the temperature dependence of the superfluid fraction inside nanopores. The absolute fractions were renormalized by introducing an *ad hoc* cut-off radius to exclusively count the atoms within the inner core. The inset shows the phase

velocity v_J found in the TLL model of equation 2.13 as a function of the radius of nanopores.

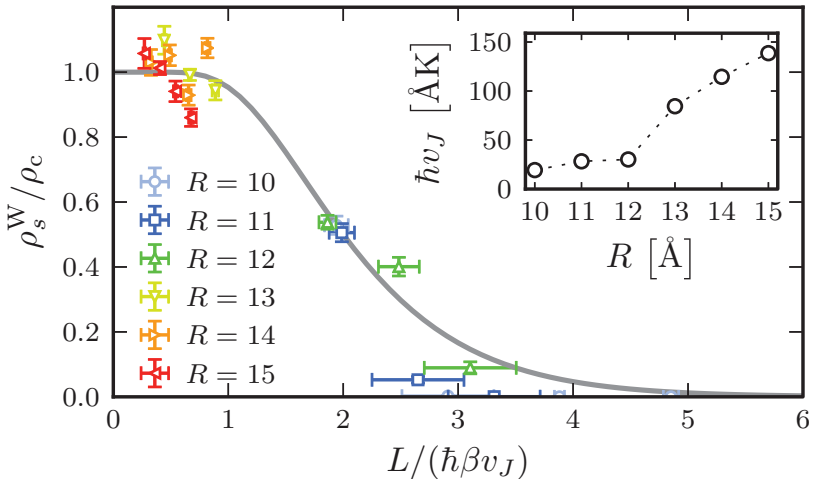

Fig. 2.9 Superfluid fraction inside the core (subscript "c") of nanopores of various radii R as a function of temperature ($\beta \equiv 1/k_B T$). The nanopores in the simulation had length L and radius R. Inset shows the phase velocity extracted from a fit to TLL theory. Reproduced from [3].

Again, the good agreement of the QMC simulations with the predictions of TLL theory (solid grey line) for atoms confined within the nanopore speaks to the potential of observing 1D signatures in liquid helium transport measurements. In other words, for a sufficiently narrow and long transport channel at sufficiently low temperature, the simulation results predict that ^{4}He atoms should behave as a strictly 1D system with the nature of the inter-particle interactions well described by the TLL theory.

Chapter 4 will describe how we integrated some of the strengths and alleviated some of the drawbacks of existing experiments to develop a new experimental scheme in the search for an experimental realization of Luttinger liquids. Prior to the exploration of the experiment design, a chapter is devoted

to present an overview of the theoretical foundations required to interpret the data in the thesis.

Chapter 3

Theory of Mass Flow in Short Pipes

The physics of fluidic systems has attracted the interest of generations of scientists and engineers both for the breadth of physical phenomena it encompasses and for the critical knowledge that modelization provides to several industries. In fact, key insights into the physics of fluids can be obtained by making a few assumptions, however, the Navier-Stokes equations are complex and still famously carry a *Clay Mathematics Institute* prize for the generic proof of their solvability. The experiments I present in the next chapters are conducted over a wide range of thermodynamic conditions and span different regimes of mass transport. Since the dynamics of fluids are strongly affected by the physical characteristics of the fluid, several simplified models are required to explain the fluid behavior over the whole thermodynamic range. For example, the assumptions built in a model for low-density fluids are not necessarily valid at

higher density and a new model must be used instead.

3.1 Knudsen Number As an Indicator of Flow Regimes

A good indicator of the appropriate model to choose to describe the flow in a given system is the Knudsen number Kn. This dimensionless parameter is defined as the ratio of the mean-free-path (λ) of a particle to the characteristic length scale of the environment in which it propagates. In the case of mass transport through circular apertures, the convention is to compare the mean-free-path to the diameter (D) of the pore.

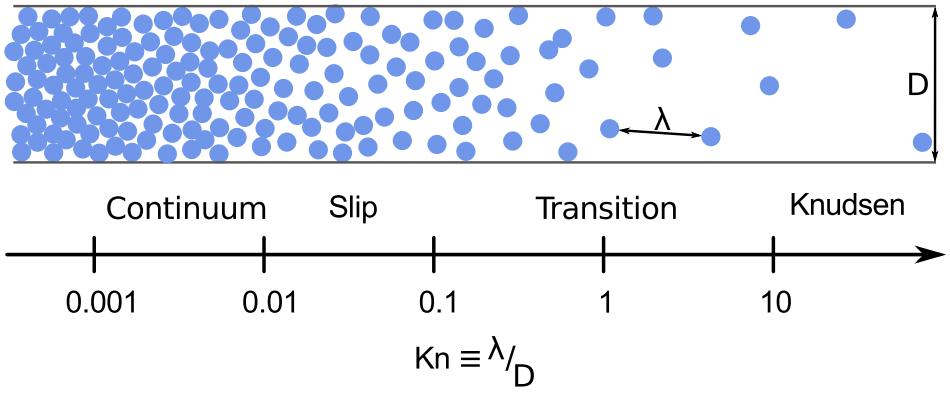

Fig. 3.1 The Knudsen number scale indicates the regions of applicability of different fluid dynamics models.

3.1.1 Mean-Free-Path of a Gas

The mean-free-path is the distance a particle can travel between interactions, averaged over the entire velocity distribution of the particles in the system. Given a gas with a Maxwellian distribution of velocities and concentration n in units of atoms per cubic meter, the mean-free-path is:

$$\lambda = \frac{1}{\sqrt{2} n \pi \sigma^2}. \tag{3.1}$$

Here, the factor of $\sqrt{2}$ comes from averaging collisions between particles with a Maxwell distribution of velocities and σ is the collision cross section. This latter equation assumes an homogeneous gas at equilibrium and, using the ideal gas law[1], $n = \frac{P}{k_B T}$, we obtain

$$\lambda = \frac{k_B T}{\sqrt{2} \pi \sigma^2 P}. \tag{3.2}$$

The symbols k_B, T and P are the Boltzmann constant, the thermodynamic temperature and pressure respectively. Finally, the cross section diameter is well known for helium and is equal to 2.18 Å (table 1.2-2 in [47]).

3.2 A Continuum of Flow Regimes

3.2.1 Knudsen Effusion of Simple Gases

A statistical approach can be used to treat gas particles interacting only through elastic collisions if they have a well defined distribution of velocities. Taking an arbitrary surface A and integrating, over the whole solid angle, all velocity vectors of particles with a Maxwell-Boltzmann distribution [48], one finds an average flux through a given surface:

[1]The ideal gas law is, in principle, only accurate at low gas densities. Given that we only use the ideal gas law to find the mean-free-path λ, which gives us the Knudsen number Kn, any deviation of the physical mean-free-path at high-density from equation 3.2 is not problematic in our modeling. The small error in our calculated λ only modifies the position of data on the abscissa. The flow computed from theoretical models is also displayed for Kn computed with equation 3.2 and the fit to the data is therefore not affected by this small offset.

$$Q^{pinhole} = \frac{1}{4} n \bar{v} A. \tag{3.3}$$

Here, the solution is expressed with the average particle velocity $\bar{v} = \sqrt{\frac{8k_BT}{\pi M}}$, where M is the mass of the particles. If one considers an enclosure with a single opening and defines that opening as the surface A, then the flux of atoms out of the enclosure is given by equation 3.3. We obtain the mass flow through an aperture of area A by substituting the average velocity $\bar{v}$ and the atom concentration n in equation 3.3 such that

$$\begin{aligned} Q_m^{pinhole} &= Q^{pinhole} \cdot M \\ &= \left(\frac{1}{4} n \bar{v} A\right) \cdot M \\ &= \frac{1}{4} \left(\frac{P}{k_B T}\right) \left(\sqrt{\frac{8k_B T}{\pi M}}\right) (\pi R^2) \cdot M \\ &= \left(R^2 \sqrt{\frac{\pi M}{2k_B T}}\right) \cdot P \qquad \equiv G^{pinhole} \cdot P \end{aligned} \tag{3.4}$$

and R is the radius of a circular aperture. Here, the subscript "m" denotes a flow in units of kg/m^3 and $G^{pinhole}$ is the conductance of a pinhole in the Knudsen effusion regime when a pressure head P is applied.

Gas Flow in Short Pipes

The assumption of a pinhole geometry is an approximation valid only when the pore diameter is much larger than the pore length ($D \gg L$). Solid-state nanopores have dimensions that are typically closer to $D \approx L$ and the walls cannot be ignored in the calculation of the pore conductance. Intuitively, one

can imagine how collisions with a pore wall decrease conductance compared to the pinhole case. These collisions are diffusive and can cause particles to bounce back towards their origin. Longer pores increase the probability of collisions and thus reduce the conductance of the pore. Figure 3.2 shows a cartoon representation of this situation, where a longer pore causes more collisions with the walls and leads to a reduced total conductance.

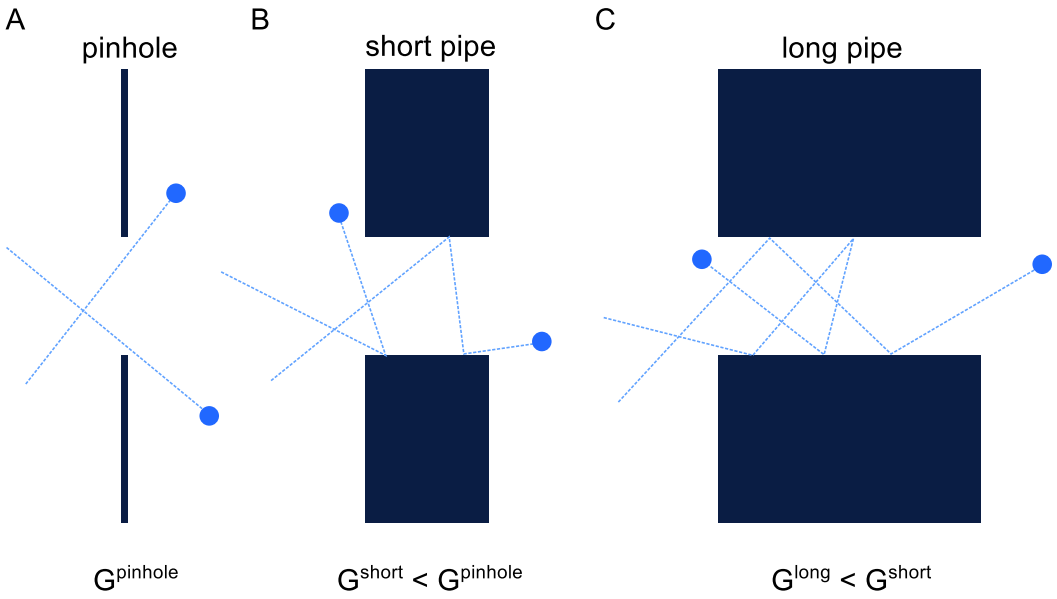

Fig. 3.2 Side view of transport channels with particles diffusing through. The conductance of the pinhole (A) is larger than the short (B) and long(C) pipes because longer pores increase the odds of back reflections due to collisions with the walls.

In fact, the mass transport through a channel of finite length at high Knudsen number can be modeled using a transmission probability $\mathcal{T}$. Both the length of the pore and the nature of the collisions with the wall affect $\mathcal{T}$. Assuming diffusive collisions at the walls allows one to compute the probability that a particle passes from one side of a channel to the other, accounting for all collisions along the way.

The Clausing Factor

The effective conductance of the pore is then reduced by the transmission probability to

$$G \equiv \mathcal{T} G^{pinhole},$$

where $G^{pinhole}$ is the conductance of the entrance of the channel. Clausing first introduced this concept for the effusion of gases through channels and he defined a factor K [49], latter named the "Clausing factor", to account for the reduced conductance. This Clausing factor takes into account the probability of transmission from every cross sectional "slice" along the tube and adds them in series. For cylindrical short tubes, approximate equations have been found [50], and simulations performed [51] such that the total transmission probability can be computed. The solution from Berman [50] is

$$K = 1 + y^2 - y\sqrt{y^2+1} - \frac{\left[(2-y^2)\sqrt{y^2+1} + y^3 - 2\right]^2}{4.5y\sqrt{y^2+1} - 4.5ln\left(y + \sqrt{y^2+1}\right)}, \qquad (3.5)$$

where $y \equiv L/(2R)$ for simplicity.

The Clausing factor varies from perfect transmission of 1.0 to a value of $\frac{8R}{3L}$ as the length-to-radius ratio goes from zero to infinity. In addition, it has been shown [52] that the Clausing factor in pores with elliptical cross-sections has a correction of less than 2% with respect to that of circular pores of the same area. This indicates that small deviations of nanopore cross section from a perfect circle should have little discernible effect on the mass transport

modeling.

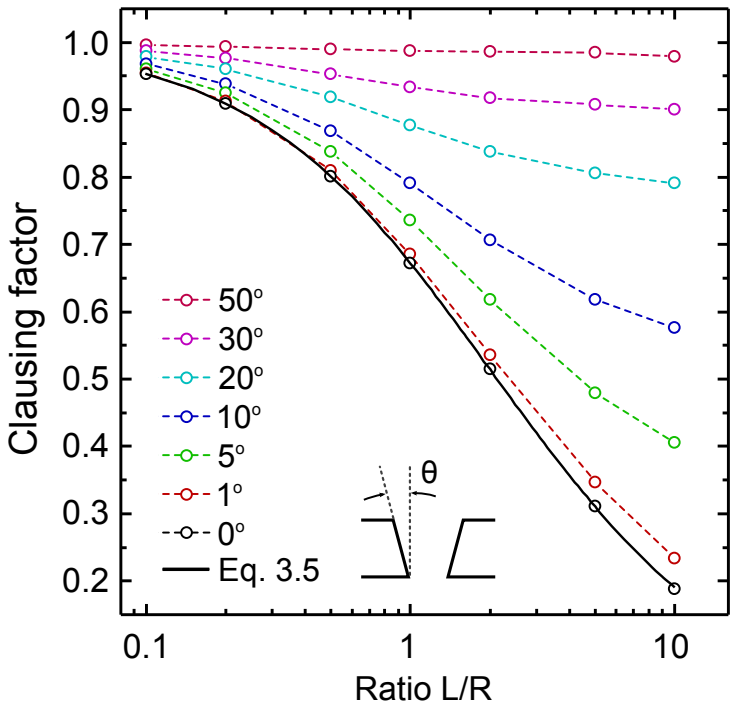

Fig. 3.3 Clausing factor computed by Iczkowski [53] (circles) for a series of angles of the opening of a transport channel. A perfect cylindrical tube has an angle of 0° and a pinhole has an angle of 90°. The dotted lines are guides-to-the-eye and the solid black line is calculated from equation 3.5.

In the earliest computational studies of diffusive transport, the cross section of the channels was kept constant along the length of the channel. This turns out to be a very good approximation for large experimental systems. However, it is not the case for our nanopores since there is usually a ∼10° opening angle between the wall and its axis. Therefore, the constant cross section assumption may no longer be appropriate to model the flow in the smaller pores that we studied. Recent computational work has however been done [53, 54, 55] to account for a non-constant cross section where diffusion in channels with a

conical shape were simulated and the dependence of the Clausing factor on the opening angle was extracted. Figure 3.3 shows the Clausing factor for angles ranging from 0° to 50° as a function of the length-to-radius ratio (L/R)[53]. The angle used in the computation is measured between the pore wall and the pore axis, as seen in the diagram inside figure 3.3. Once the Clausing factor is determined, we can then compute the expected conductance of a pore in the Knudsen effusion regime, which is given by

$$G^{Knudsen} = K\left(R^2\sqrt{\frac{\pi M}{2k_BT}}\right). \tag{3.6}$$

3.2.2 Hydrodynamics of Viscous Flow

The typical mean-free-path of helium at standard pressure and temperature (STP) is, from equation 3.2, $\lambda \approx 10^{-6}$ m, which is comparable to the nanopore dimensions. This makes it experimentally possible to access different flow regimes by a simple tuning of the mean-free-path via a change in pressure. It is usually assumed that mass flow in systems with $\mathrm{Kn} \lesssim 10^{-2}$ are in the continuum regime, and that small corrections accounting for slip behavior at the wall occurs for $10^{-2} \lesssim \mathrm{Kn} \lesssim 10^{-1}$. The regime that bridges the gap from Knudsen effusive flows to viscous flows is referred to as the transitional regime.

We can model viscous fluid dynamics by making three hypotheses regarding the fluid. The first is mass conservation, where by virtue of the continuity equation, a fluid element is preserved in space and time from one position to the next. The second is momentum conservation of the fluid which regulates how forces modify the velocity field. The last one is, as expected, energy

conservation. These three assumptions, once combined, give the Navier-Stokes equation of fluid dynamics. This equation is, however, hard to solve in general and further assumptions must be made to obtain an analytic equation for the flow.

As stated in the section treating Knudsen effusion, the nanopore has a length-to-radius ratio close to unity ($\frac{L}{R} \approx 1$). This prevents us from using the "infinite-length" approximation that gives rise to the well-known Poiseuille flow in long channels,

$$Q^{\infty}_{viscous} = \frac{\pi R^4 \Delta P}{8\eta L}, \tag{3.7}$$

where η is the dynamic viscosity and ΔP is the pressure measured across the pipe. Langhaar [56] has used a linearization of the Navier-Stokes equation to describe the pressure drop in the transition length of a straight tube. In a finite pipe, an additional pressure drop is caused by the acceleration of the fluid at the ends of the channel where a fully-developed flow profile is not yet reached, *i.e.* in the transition length. This additional contribution is proportional to a factor α, and so the pressure drop is given by

$$\Delta P = \frac{32\eta L v}{D^2} + \frac{\alpha}{2}\rho v^2, \tag{3.8}$$

where D is the channel diameter. Solving for the velocity v in the latter equation gives

$$v = \frac{32\eta L}{\alpha \rho D^2}\left(\sqrt{1 + \frac{\alpha \rho D^4}{512\eta^2 L^2}\Delta P} - 1\right), \tag{3.9}$$

and the mass flow is given by $Q_m = \rho v A$, where ρ is the density and the area A is taken as a circle of radius $R \equiv D/2$. The viscous flow in a pore where the transition length is taken into account is thus given by

$$Q_m = \frac{8\pi\eta L}{\alpha}\left(\sqrt{1+\frac{\alpha\rho R^4}{32\eta^2 L^2}\Delta P}-1\right). \tag{3.10}$$

This equation will be further discussed throughout chapter 5.

Reynolds number in Nanopores

Hydrodynamic equations are often described in terms of dimensionless numbers that help separate systems into distinct groups. The Knudsen number used in this chapter is an example of a dimensionless number that classifies different flow regimes. Another useful dimensionless parameter is the Reynolds number, which compares the effect of viscosity to typical system dimensions and thus informs us on diffusive behavior, such as the onset of turbulence. The Reynolds number is defined as

$$Re = \frac{\rho v D}{\eta},$$

for cylindrical pores. Once converted using the definition of mass flow $Q_m = \rho v A$, it readily gives

$$Re = \frac{4Q}{\pi D \eta}. \tag{3.11}$$

Given the non-linear dependence of flow on the diameter of the pore, the highest Reynolds number for gas flow will be obtained in pores with large

diameters and at low temperatures where the viscosity is smallest. In particular, for the ∼100 nm sample presented in chapter 5, the Reynolds number is estimated to be at most $Re \approx \frac{4 \cdot 3\text{x}10^{-11}\text{kg/s}}{\pi \cdot 100\text{x}10^{-9}\text{nm} \cdot 8.8\text{x}10^{-6}\text{Pa·s}} = 43$ at liquid nitrogen temperature and for the highest pressures reached. At the opposite end, small nanopores with diameters of approximately 15 nm have $Re \approx 0.14$ at room temperatures. The same calculation can be accomplished for the liquid helium flow experiments with the $D = 45$ nm pore, where the mass flow was determined to be $5\text{x}10^{-12}$ kg/s and $\eta \approx 3.5\text{x}10^{-6}$ Pa·s, which leads to a Reynolds number of $Re = 47$. The Reynolds number for the liquid helium flow experiments in the smaller nanopore of 15 nm is $Re = 2.8$. Finally, laminar flow is usually expected to be a good approximation for Reynolds numbers below ∼1800. Above this point, turbulence is expected to emerge and the dynamics of the viscous fluid become fundamentally different.

3.3 Liquid Helium Flow

One of the most striking characteristic of helium at low temperature is a second order phase transition at 2.17 K, below which the unusual properties of the liquid prompted Kapitza [57] to name this new state of matter “superfluid”. Above the transition, helium behaves like a normal liquid and its transport properties are characterized by a well defined viscosity. Measurements of viscosity fall into two types of experiments. Either flow is induced in a channel by the application of a pressure head, or the moment of inertia of an oscillating disk is measured. Classical liquids yield the same viscosity with both methods. By contrast, the same experiments conducted with liquid below the superfluid

transition yield strikingly different results. Channel flow measurements of He-II indicate a sharp decrease of the dynamic viscosity as temperature is lowered below T_λ. Meanwhile, the oscillating disks experiments demonstrate He-II possesses a substantial viscosity causing damping of the disk motion. These apparently contradictory results have however been explained successfully by the development of the well-known "two-fluid model". Interesting historical accounts of the discovery and characterization of the properties of the superfluid state of matter are readily available *e.g.* [58, 59] and only relevant results will be presented here.

3.3.1 Two-Fluid Model

In the two-fluid model, the behavior of helium is explained by a dual description of complementary components that are viewed as simultaneously mixed together, but with independent motion. The first component, the normal phase, has physical properties matching the liquid helium of the He-I phase. It also carries entropy and is responsible for the measurable viscosity. The second component, the superfluid, is assumed to be a viscousless fluid undergoing potential flow [60], *i.e.* a flow that is curl free and carries no entropy. The normal component and the superfluid component are related through a flux equation:

$$\vec{J}_{total} = \rho_s \vec{v}_s + \rho_n \vec{v}_n, \tag{3.12}$$

where ρ_s and ρ_n are, respectively, the densities of the superfluid and normal components of He-II, and are related to the total fluid density $\rho = \rho_s + \rho_n$.

The fraction of superfluid composing the He-II phase approaches unity asymptotically as the temperature is reduced from T_λ to T= 0 K. A typical rule of thumb is that He-II is essentially all superfluid below ∼1 K and the normal component has a functional dependence on temperature close to

$$\frac{\rho_n}{\rho} = \left(\frac{T}{T_\lambda}\right)^{5.6}$$

up to T_λ. Figure 3.4 shows the calculated [61] fraction of normal density over total density for bulk liquid helium.

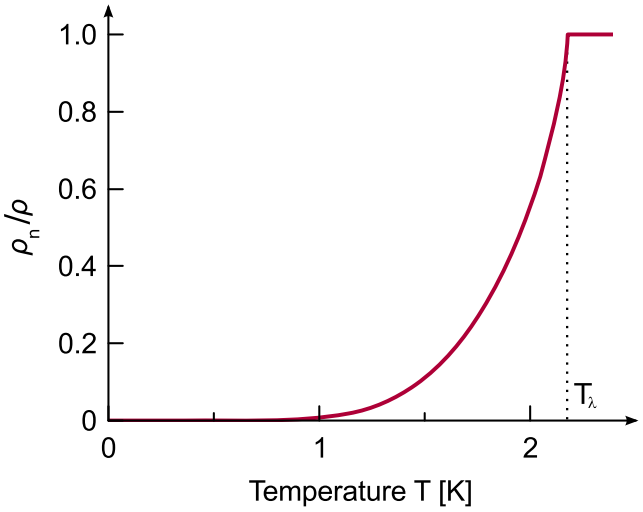

Fig. 3.4 Fraction of normal density over total density of helium in the He-II phase. The sharp decrease of the normal component is observed at the superfluid transition and almost no normal helium remains below 1 K. Data from Brooks [61].

3.3.2 Excitations in Superfluid Helium

While the two-fluid model was initially understood in macroscopic terms, Landau took a different approach and attempted to describe the superfluid state

with respect to its excitations. This microscopic theory of the He II phase was designed semi-empirically to fit experimental data and explain the seemingly intractable characteristics of this unconventional state of matter. Specifically, the low temperature dependence of the specific heat followed a T^3 power law for $T \lesssim 0.6$, and nearly doubled between T = 1 K and T_λ. Such observations, and Landau's strong physical intuition, led him to posit the dispersion relation of figure 3.5.

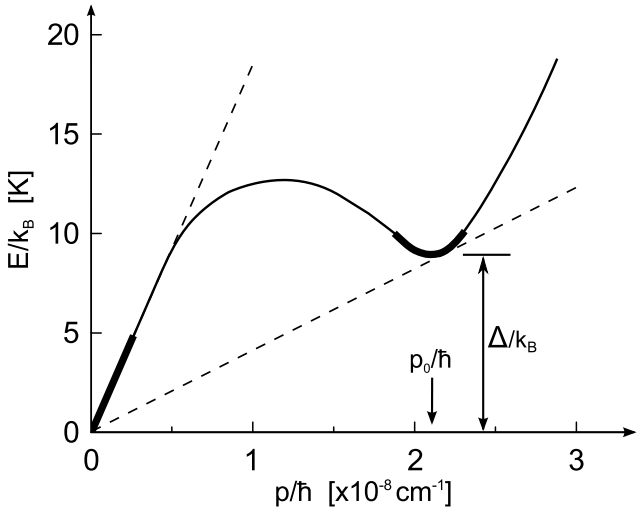

Fig. 3.5 Dispersion relation of the excitations in He-II. The lowest energy excitations are characterized by a linear dispersion of small wave-number. These collective modes are similar to longitudinal phonons in solids. Present at larger momentum p_0 is the "roton" minimum, a collective excitation mode with an energy gap Δ. The excitations described by the convex dispersion relation at p_0 are interpreted as quantized rotational motion of small groups of He atoms. The slope of the dashed and dotted lines give an estimate of the propagation velocity of each dissipation mode. Figure based on figure 1.10 of [58].

At the lowest energy, the dispersion relation $E(p) = pv_{ph} = \hbar k v_{ph}$ has a linear behavior characterized by a large propagation velocity ($v_{ph} \sim 240$ m/s).

These collective modes are extended longitudinal waves similar to the phonon modes in solids. The local minimum centered at $p_0/\hbar$ describes localized excitations called "rotons". Landau envisioned them as small groups of atoms with a rotational motion and carrying an energy

$$E(p) = \Delta + \frac{(p - p_0)^2}{2\mu},$$

where μ is an effective mass and a gap Δ is a thermal barrier limiting the emergence of this dissipation mode. Neutron scattering experiments have confirmed the qualitative shape of this dispersion relation for He II and the free parameters p_0, Δ and μ have been measured as $p_0/\hbar = 19.1$ nm^{-1}, $\Delta/k_B = 8.65$ K and $\mu = 0.16m_4$, with m_4 the atomic mass of helium.

Landau defined a velocity v_L below which superfluid could flow without dissipation. For larger velocities, excitations would be produced and the fluid would dissipate energy. This is known as the Landau criteria for superfluidity and, shown by a dotted line on the dispersion relation of figure 3.5, is given by

$$v_L = \left[\frac{E(\vec{p})}{|\vec{p}|}\right]_{min},$$

where $v_L \approx 58$ m/s in bulk He II. Phenomenologically, the fact that the v_L is not zero in the dispersion relation of figure 3.5 allows the superfluid to propagate without friction up to a critical velocity. All superfluid flow experiments to date however observe a much smaller critical velocity, as seen in figure 3.6. Further refinements were needed to characterize the dissipation in superfluids.

3.3.3 Vortices and Critical Velocity

Feynman suggested a dissipation mechanism where vortices traveling through the superfluid could allow this potential flow to shed energy [62]. He first assumed He II could be described by a macroscopic wavefunction $\Psi = \Psi_0 e^{i\phi}$, where the amplitude $\Psi = \Psi(\vec{r}, t)$ and phase $\phi = \phi(\vec{r}, t)$ are defined at all positions $\vec{r}$ and over time t. The amplitude of the wavefunction is normalized as $|\Psi|^2 = \rho_s/m_4$, for particles with a mass of four atomic mass units. The macroscopic phase ϕ is assumed to vary slowly and is related to the superfluid velocity as

$$\vec{v}_s = \frac{\hbar}{m_4}\vec{\nabla}\phi.$$

A consequence of the macroscopic phase of the quantum fluid being unique at all positions is that the circulation Γ around a closed loop must be quantized,

$$\Gamma = \oint \vec{v}_s d\vec{l} = n\kappa_4, \text{ for an integer } n,$$

where $\kappa_4 = 2\pi\hbar/m_4$ is the quantum of circulation. A quantized circulation also has a secondary consequence on the formation of vortices. In the central region, where the constant-phase lines would meet, the wavefunction must vanish in order for the conditions of the superfluid potential flow to be met. This region, where the Ψ (and thus ρ_s) drops to zero, is labeled the vortex *core*, and has a size a_0. Feynman finally argued that the creation of such a vortex within the superfluid would be energetically favorable when the velocity reaches

$$v_F \equiv \frac{\kappa_4}{2\pi D} \ln\left(\frac{D}{a_0}\right), \tag{3.13}$$

where D is the channel diameter. The core a_0 is approximately 2 Å and grows with temperature up to the superfluid transition temperature. In this picture, the vortex can continuously funnel energy away from the superfluid and keep the flow at a fixed velocity[63]. Interestingly, the critical velocities predicted with this new mechanism are quite close to the experimentally measured ones. Indeed, most experimental critical velocities in larger capillaries ($> \mathcal{O}(10^{-6})$ m) were indeed found to follow roughly the "$1/D$" size-dependence of equation 3.13 (see figure 3.6).

The agreement between experimental critical velocities and the Feynman dissipation model contributed to the rapid acceptance of quantized vortices as an alternative to Landau's roton modes. Some experiments eventually found, however, that in smaller pores, the critical velocities could be much larger, independent of channel size and have a marked temperature dependence [65, 66, 67, 68]. Some of these results are shown in figure 3.6 with the $\circ$ symbol. Importantly, those experiments found a linear temperature-dependence given by

$$v_c(T) = v_{c0}\left(1 - \frac{T}{T_0}\right). \tag{3.14}$$

In this equation, v_{c0} is the critical velocity extrapolated to T = 0 K and T_0 is a fit parameter typically between 2.2 K and 2.8 K.

To further understand the dissipation mechanism behind these new results,

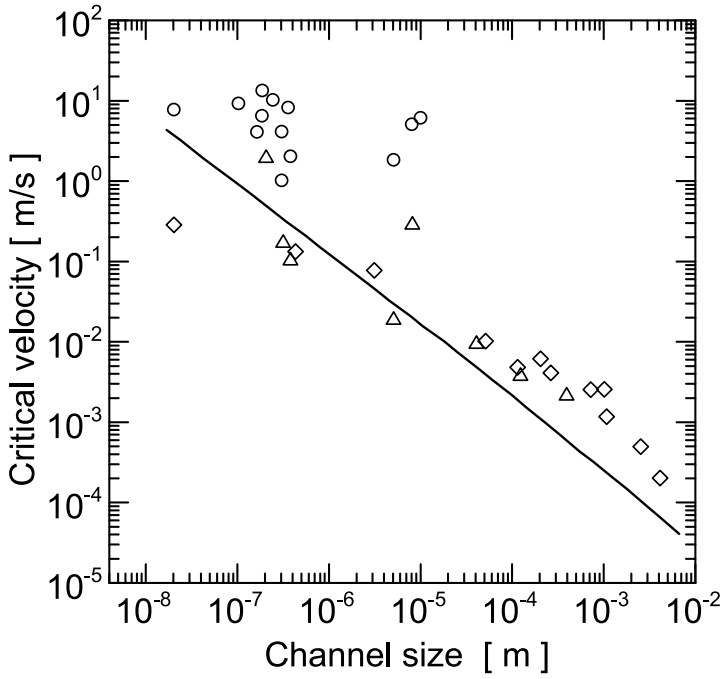

Fig. 3.6 Critical velocity measured in several experiments over the last few decades. Circles (○) are experiments where a temperature dependence was observed. Other symbols represent results of experiments where the critical velocity is temperature-independent but still varies with channel size. The solid line is the Feynman critical velocity of equation 3.13. Points in the nanometer region are from experiments in helium film flow and the smallest systems previously accessible. Reproduced from [64].

very sensitive experiments were designed to measure superfluid flow in micro-capillaries [69, 70, 71]. The results of these experiments are that vortices are nucleated near the channel and the flow effectively experiences "phase-slips". This spontaneously reduces the superfluid velocity and leads to a critical velocity. The nucleation of such vortices was found to be thermally activated following an Ahrhenius-like form,

$$\Gamma = \frac{\omega}{2\pi} e^{-\frac{E_a}{k_B T}}, \tag{3.15}$$

where ω is the attempt frequency of the nucleation and E_a is the activation energy, *i.e.* the energy that must be surpassed by the thermal fluctuations. The specifics of this stochastic nucleation process have been quantified by several authors and thorough reviews of the subject are available [64, 72]. For the purpose of this thesis, the temperature and size dependence of the critical velocity are of particular interest, since they offer important clues about the nature of dissipation in superfluids.

Chapter 4

Sample Preparation and Flow Measurement Technical Details

The development of controlled fabrication of very small pores [73, 74] has been largely driven by research on bio-molecule separation [75, 76, 77], where discrimination of single molecules can be achieved in channel diameters having roughly the same size as the molecules studied. Many techniques have since been developed for fabrication of tailored nanopores with virtually any diameter [78, 79, 80].

In addition to fabrication techniques involving chemical etching [81] or biological structures [82], one strategy has been to use a focused beam of energetic charged particles to gradually remove material in a thin membrane to effectively drill a single aperture. This controlled ablation can be achieved with various ionic species, but the best precision is obtained using the electron beams of field-effect transmission electron microscopes (TEM). This re-

cent development has allowed, for the first time, the controlled production of nanostructures down to less than one nanometer. These approaches for tailored fabrication of nanopores can be compared to the intuitive option of simply using pre-formed nanochannels, such as carbon nanotubes. While these nanotubes have the desired small cross-sectional opening, they are typically produced in large quantity and are thus available as membranes composed of large aggregates of aligned nanotubes[83]. These are therefore not suited for our experiments.

4.1 Sample Preparation

4.1.1 Solid-State Silicon Nitride Membranes

Recent advances in the electronic imaging industry have made it possible to manipulate electron beams with exquisite control. Such precise control allows one to focus the beam on a surface and expose only a few square nanometers. This is the chief method that we have chosen in order to fabricate nanochannels with the required length scale.

As mentioned above, our nanopores were made by electron-beam drilling in a very thin membrane. These free-standing membranes are commercially available, and many companies manufacture them. Unless otherwise noted, all samples used in this thesis were produced using wafers from Silson Inc.®. They were manufactured by low-pressure chemical vapor deposition such that a uniform layer of amorphous Si_3N_4 was grown over the whole silicon surface. These membranes were then formed by chemically etching the silicon within a small area of the 200 μm thick wafer pre-coated with the silicon nitride

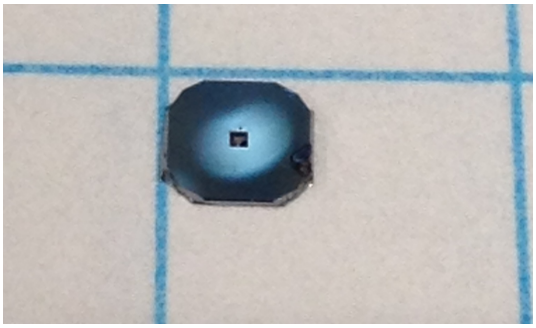

Fig. 4.1 Photograph of a typical wafer used to fabricate nanopore samples. In the center of the wafer, a pyramidal pit can be seen and is the result of the etching of an area of silicon. This selective etching leaves only the free-standing silicon nitride membrane (on the bottom face here).

layers. This etching only removes the silicon and thus leaves a bare, free-standing Si_3N_4 film, covering an empty pyramidal pit, as shown in figure 4.1. The silicon wafers are typically square shaped (2x2 mm) and the free-standing Si_3N_4 membrane are squares 30 to 50 μm wide.

The experiments presented in this work were conducted using membranes with a thickness of 30, 50, 75 or 100 nm. Since nanopores are drilled through the membranes, their thickness *de facto* defines the length of the nanopores. When the length of nanopores is not critical to a given experiment, thinner membranes are usually preferred because they allow much faster nanopore drilling, which reduces the risk of producing irregular-shaped nanopores. The trade-off of using thin membranes is that their low fracture strength limits the maximum differential pressure they can withstand. We have empirically determined that the limiting pressures (*i.e.* membrane-breaking pressure) were $\sim$45 bar for 50 nm thick membranes, and 6.7 bar for 30 nm thick ones. If larger pressure differentials are required in future experiments, stronger membranes

could easily be produced by etching a smaller area of the wafer, effectively decreasing the surface area of free-standing silicon nitride.

The thickness of the membrane has a large impact on the time scale required to ablate and pierce through the SiN. In particular, if the sample stage inside the microscope has no drift and the electron beam stays in one area, a 30 nm membrane will typically be pierced in a few seconds, whereas it would take 60 seconds for a 50 nm one and up to several minutes for membranes 100 nm thick.

4.1.2 Sample Fabrication

We fabricated the nanopores using the field-effect transmission electron microscope JEM-2100F located at the École polytechnique de Montréal. Inside the TEM, the electrons are accelerated by voltages up to 200 kV and are controlled with magnetic lenses. A careful optimization of the beam intensity and focus allows us to achieve a beam spot size of barely a few nanometers wide. If this electron bombardment is maintained on the same area for several seconds or minutes, enough material is removed to form a nanopore in the membrane. Once this initial pore is opened, it is possible to move the sample stage a few nanometers away so that the beam becomes aligned with the edges of the nanopore. This forces the atoms from the pore wall to be removed gradually in a controllable manner. With this technique, the nanopore can be carved out into a cylindrical shape and up to any diameter, from 0 to more than 100 nm. We have fabricated hundreds of such pores during the process of preparing samples for the experiments presented in this thesis and in figure 4.2, I show

a few typical samples.

Finally, I also point out that this technique has a big advantage in that it allows one to "see" the nanopore while it is being drilled. A picture can therefore be taken immediately after fabrication. This direct imaging thus makes it possible to readily determine the dimensions of the nanopore and discriminate samples based on the requirements of each experiment.

Nanopore Geometry

In principle, the precision of the electron beam gives great control over the effective hole size and allows a very careful fabrication of nanopores [84]. While true, there are however practical difficulties in using magnetic lenses to control a beam of charged particles to carve out a hole in an amorphous material like silicon nitride. In particular, slight distortions in the beam's cross sectional profile may affect the resulting nanopore and produce a non-circular cross section; in other words non-gaussian beams can produce irregular drilling. This is especially relevant since the drilling is conducted at high magnification, whereas the pore is imaged at lower magnification. This means that the pore seen during the drilling can appear perfectly circular at high magnification, but upon further imaging at low magnification, the actual shape is usually found to differ slightly. Because of this risk of distortion of the nanopore shape during the drilling procedure, careful images of each nanopores were taken after each fabrication, at a magnification low enough to avoid distortions. Finally, the calibration of these images allowed us to determine the nanopore sizes directly after fabrication.

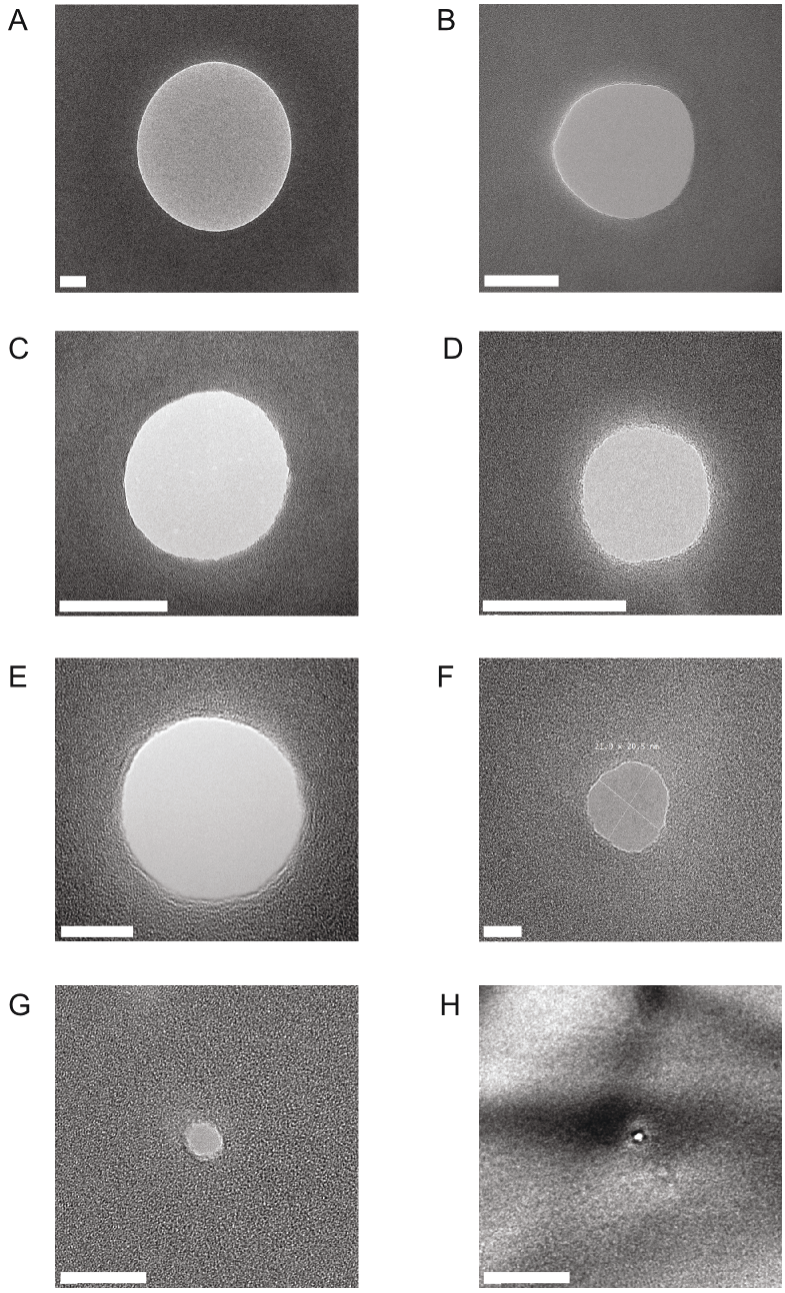

Fig. 4.2 Transmission electron pictures of different nanopores ranging in size from 300 nm to less than 2 nm in diameter. The nanopores were fabricated by electron ablation of a silicon nitride membrane suspended on a silicon wafer. The white bars are respectively 50 nm for pictures A-D and 10 nm for pictures E-H.

Regarding the nanopore profile, it is generally assumed that the ablation of material is initiated simultaneously from both sides of the membrane and continues until the two aligned cavities connect halfway to form a fully opened channel. If one considers the beam cross sectional intensity to be decreasing radially, then the outer edges of the electron beam are less dense and so will not drill as fast as in the center of the beam. This means that the ablation is more efficient along the axis of the electron beam, but also that the area around the nanopores has potentially been bombarded as well, albeit at much smaller intensity. Indeed, 3D tomography analysis of the nanopores [85] shows that the ablation of material with highly energetic electrons does not produce a perfectly cylindrical pore, but rather an "hourglass" shaped one. Despite this, it is possible to alter this initial pore shape with a secondary treatment that straightens the pore walls. This treatment consists of an exposure of the area surrounding the nanopore to a low-intensity beam for a short time [86]. It effectively gives the atoms near the nanopore edge enough energy to redistribute themselves and "flow-back" in the pore. In fact, we have observed repeatedly that this technique has helped stabilize the SiN surface and reduces nanopore deformation over time.

Interestingly, this same method can also be used to shrink the nanopores. In fact, a longer exposure time under low intensity can maintain the fluidization of nearby atoms and keep filling the nanopore until it eventually closes [87, 88]. We have used this method to produce nanopores smaller than 3 nanometers, as can be seen in figure 4.2G,H. The parameters for this procedure are however not always reliable and more work is required to fully capture the subtleties

of the physics at play during the shaping down of solid-state nanopores.

Nanopore Opening Angle

The mass transport experiments described in this thesis are very sensitive to the diameter and opening angle of the nanopore. In essence, the conductance of a pore is intrinsically determined by its geometry and it is therefore important to determine, as much as possible, the three-dimensional shape and profile of pores.

The intensity of the TEM picture can be used to provide an estimate of the shape of the nanopores. To first order, the intensity of the transmitted electrons is proportional to the thickness of SiN. Thus, making use of the average saturation of a group of pixels, a "thickness" can be estimated. We took the average of pixels in the center of the pore as an intensity background to define a thickness of zero. We can do the same for the complete thickness using the pixels away from the pore. This way, a calibration is obtained as a function of the saturation in each point of the picture. If we further assume a symmetric material ablation with respect to the middle plane of the wafer [85], we can reconstruct a 2D profile from the images. In order for the profile to be clear, the high amount of fluctuation in intensity in the TEM picture must be averaged over adjacent pixels. Grey points in figure 4.3B show the equivalent thickness of all pixels without averaging, whereas the black dots show the thickness computed from a local average of pixel intensities.

The power of this relatively simple procedure is to gain information on the shape of the nanopores that ultimately will be used in the mass transport

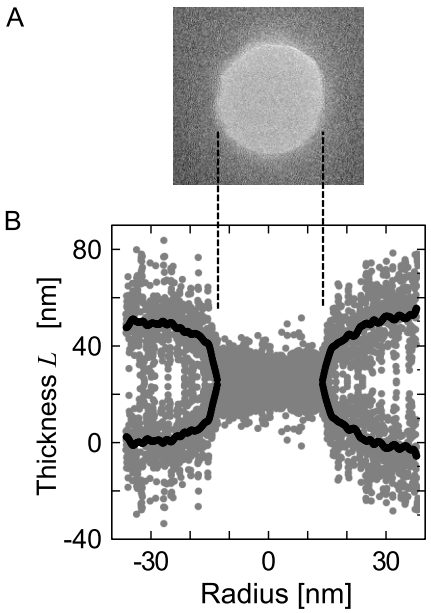

Fig. 4.3 TEM images (A) can be used to infer the thickness of material (B) the electrons go through. The intensity away from the pore is set as the thickness of membrane chosen at manufacturing, (in this case 50 nm), and the intensity in the center of the pore to zero. The intensities in between are normalized to this thickness and we can infer the profile of the nanopore. This profile shows the slight opening angle of $\sim 10^\circ$ with respect the a perfect vertical channel wall.

experiments. Since the true nanopore shape is not perfectly cylindrical, a modified Clausing factor will have to be used to improve the modeling of the data. Judging from nanopore profiles similar to that shown in figure 4.3, it is reasonable to estimate the opening angle with respect to the vertical axis at $\sim 10^\circ$. For that sample, a quantitative comparison with the Knudsen conductance of small pores will be shown in the next chapter.

Nanopore Diagnostics with Electron Microscope

The difference between a partially obstructed nanopore and a fully drilled one can easily be observed in the TEM images. Specifically, the spatial fluctuation in the intensity measured by the CCD camera of the TEM are qualitatively different when the electrons go through either vacuum or the membrane. This means that a visual inspection of the TEM image is sufficient to determine whether the pores remain open or close during storage or post-experiment. Another feature of clean nanopores is the brighter boundary at the perimeter of the nanopore caused by electron diffraction off of the solid pore wall. Figure 4.2A shows this clearly where the low-intensity noise in the center of the nanopore contrasts greatly with the larger intensity fluctuations caused by electron interference in the amorphous SiN. These characteristics in the nanopore images show the focus of the electron beam is optimized and that the surface is free of contaminants. When pores are blocked by contaminants, the electron diffraction and transmission intensity are both affected in a way that the user can readily identify.

Nanopores are at risk of becoming partially or fully blocked by contaminants at any time and the TEM can be used as a diagnostic tool to identify the nature of this contamination. For example, we have used the energy dispersive X-ray spectroscopy (EDX) capabilities of the TEM to determine the nature of the material covering blocked pores. A strong carbon signature was a typical result of this procedure and indicated external contaminants. In these cases, the nanopores could not be redrilled and the whole wafer was assumed to be contaminated, and was therefore discarded.

4.2 Flow Measurements Via Mass Spectrometry

The fabrication technique described in the previous section is very advantageous to create a single nanometric channel inside a solid-state membrane. Historically, the simplest way to measure mass transport was to detect the change in a thermodynamic variable of the fluid within the reservoirs on either side of the transport channel [89]. For example, this could be the pressure change in a fixed volume as some of the fluid inside flows out. This technique is, however, only effective for macroscopic apertures since, in very small ones, the change in pressure becomes smaller than the precision of pressure gauges, due to the large relative size of the *source* and *drain* reservoirs. In other words, enough particles must flow out for the pressure change to be discernible. A quick estimate shows that in a typical experimental enclosure of volume $\mathcal{O}(10^{-5})$ m^3 contains approximately $3{\cdot}10^{20}$ gas particles at standard temperature and pressure. Typical mass flows in small apertures of size 100 nm or less are, at most, of the order of $\mathcal{O}(10^{14})$ atoms/s and, consequently, a 1 % drop would take $\mathcal{O}(10^6)$ seconds, which is experimentally prohibitive.

A more efficient method to measure mass transport is to literally *count* the atoms going through the nanochannel. One way this can be accomplished is by pumping continuously on the drain reservoir below the pore and use a mass spectrometer to analyze the gas flow. In particular, the mass spectrometer inside a helium leak detector is optimized for accurate measurement of helium flows. A similar method that has been shown to work in microchannels is to use a residual gas analyzer [90].

In essence, the underlying measurements of the results I present over the

next few chapters can be described as an accurate determination of a carefully-tailored single leak. The leak detector I used to make all flow measurements was a Pfeiffer Smart Test HLT560, with twelve orders of magnitude range of sensitivity to flow rates. The Smart Test device also has the option to discriminate for the mass of atoms sent to the detectors from 2 to 4 atomic mass units. This means the lighter helium isotope ^{3}He could be substituted in the experiments and be measured in exactly the same way, although it has not yet been attempted.

Mass spectrometers are designed to discriminate charged particles by their mass. For neutral gas atoms, the first step is to pass them through an ionization chamber where filaments emit a stream of electrons that ionize the atoms so they can be accelerated by an electric field. This acceleration voltage V increases the kinetic energy of each atom proportionally to its charge q, so that $qV = m|\vec{v}|^2/2$. The atoms are then passed through a homogeneous magnetic field where they are deflected by the Lorentz force $F_B = q\vec{v} \times \vec{B}$, which is proportional to the speed $|\vec{v}|$ of the atoms and the applied magnetic field B. This perpendicular force induces a curved trajectory, with $F_B = mv^2/r$, such that the radius r of each atom's path is

$$r = \frac{mv^2}{qB} = \frac{1}{B}\sqrt{\frac{2mV}{q}},$$

where the speed v was rewritten with the voltage acceleration equation from above.

Figure 4.4 shows a schematic drawing of a mass spectrometer. The three curved paths represent the paths atoms or molecules of different mass would

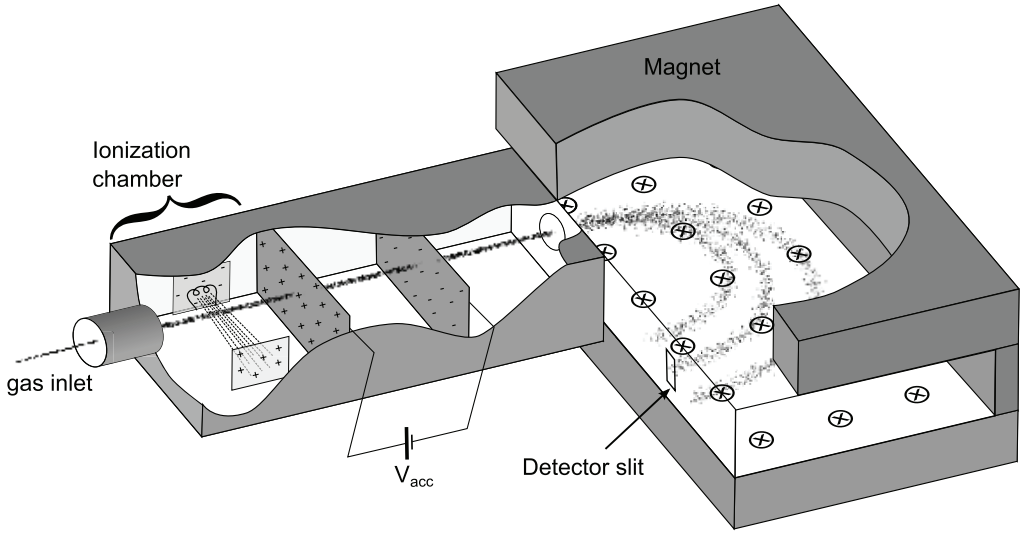

Fig. 4.4 Schematic diagram of a mass spectrometer. The gas is sent through an ionization chamber where it becomes ionized and is accelerated by an electric field towards a region where a magnetic field deflects each ionized atom. The curvature of the path these atoms take is dependent on their mass and a discrimination of the atomic species is achieved by blocking the paths of unwanted atoms, letting only the proper ones through to the detector.

follow when traveling through the magnetic field. The position of a slit can discriminate which ions reach the detector. The ion detector then returns a voltage proportional to the number of atoms with the chosen mass. A calibration of this signal was done regularly over the course of experiments to ensure that the measured flow rate was quantitatively accurate. To do so, we used a calibrated leak certified by the *US National Institute of Standards and Technology* with a value of $2.79{\cdot}10^{-8}\pm$ 10% mbar·l/s. The flow rate of helium gas through a pore can thus be accurately measured if the drain reservoir of the experimental cell is pumped on by the leak detector.

4.3 Measurement Scheme

In the previous two sections I have described the techniques necessary to fabricate nanopores, as well as to measure the mass flows of gas particles in them. I will now describe how to use these two elements to inform the design of an experimental scheme suited for measuring the mass transport inside a single nanopore. The strategy that we have used has great similarities with the measurement of charge transport in simple electric circuits. This is because the physics of electric current propagating in materials is very often described by simple concepts of resistance to flow of an ensemble of electric charges. The description of mass transport of electrically neutral particles can also be described with very similar concepts if we make a direct analogy between charges and mass, as well as electric potentials and pressure differentials. The charge transport in a material with linear resistance R and under a voltage V is described in its simplest form by Ohm's law $I = (1/R)V = G \cdot V$, where $G \equiv R^{-1}$ is the electric conductance of the material. In the case of mass transport in the linear regime, a similar equation holds,

$$Q_m = G\Delta P,$$

where the mass flow Q_m (in kg/s) is proportional to the pressure difference ΔP between the ends of the conduction channel. The constant of proportionality is the conductance G, defined analogously to the electrical conductance (inverse resistance) in Ohm's Law. The conductance of a nanopore is thus the main characteristic that we will study in our exploration of the physics of flow within

confined nanochannels.

4.3.1 Experimental Cell

The simplest strategy to detect mass flow in a single channel can be inspired by the electrical circuit analogy. A pressure differential must be applied between a *source* and a *drain* reservoirs positioned on either side of the conduction channel. This pressure differential induces a flow through the channel. In this design, it is critical that the particles in the upper reservoir, the source, can only go to the lower reservoir, the drain, via the nanosized channel, otherwise a secondary transport path would potentially dominate the signal. This is because the conductances of parallel transport paths are summed in transport measurements. In other words, the wafer holding the nanopore of interest must be perfectly sealed between the source and drain reservoirs.

Many versions of an experimental cell were designed and built throughout the course of this work, but only two are presented here. One key constraint limiting the design is that many samples should be easily substituted in the same cell without requiring too many repairs. This rules out, for example, using epoxy to seal a membrane directly inside an experimental cell. The whole cell should also remain leak-tight at all temperatures below that of the laboratory, and hold for internal pressures from approximately a hundred atmospheres down to vacuum. Other than permanent solutions like welding or *viton*® o-rings that lose elasticity at low temperatures, the best strategy to adopt here is to use a compressible wire made of soft metal, such as indium, as a non-permanent sealant. Indium wires with diameters smaller than $\sim$700

μm can be compressed between two flat surfaces and make a joint that will withstand multiple temperature cycles from room temperatures to cryogenic temperatures and remain leak-tight.

First Generation Experimental Cell

The first generation of experimental cells that we built were similar to the one shown in figure 4.5 and the photograph in figure 4.9B. The experimental cell is composed of three main parts: a top flange, a membrane support in the middle (piece T on figure 4.5), and the main cell body. The membrane support piece is easily removable and many copies were fabricated to allow for multiple samples to be prepared in parallel and thus allow faster turnaround between experiments. The body of the cell is made from high thermal conductivity *coin* silver (10%Cu,90%Ag) to ensure the best possible thermal equilibrium between the cell and the helium fluid inside it. The membrane support piece is made of Invar 42®(42%Ni) because of its very low thermal contraction coefficient that closely matches that of the Si wafer. Stainless steel capillaries are soldered to the top flange and to the body of the cell to bring helium in and out, respectively. These capillaries are then connected to a gas handling system that will be described in section 4.3.2.

A $\sim$1 mm diameter indium o-ring compressed between the top flange and the cell body ensures that the inside of the cell is completely sealed from the outside. A similar seal, albeit smaller, is also made between the membrane support and the cell body to prevent helium above the sample from reaching the bottom volume. Otherwise, this would generate an unwanted secondary

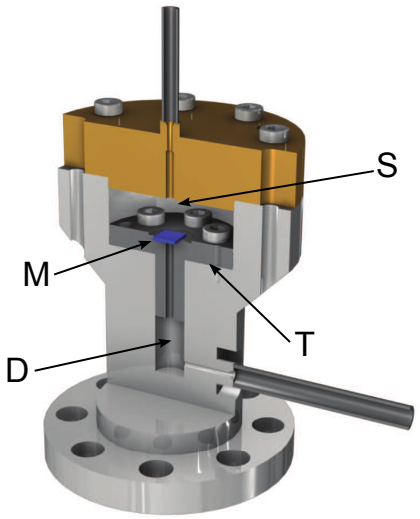

Fig. 4.5 Three-dimensional model of an experimental cell designed for mass transport measurements on a nanopore (purple wafer in the middle of the model). A top flange (brass colored) and a silver body are sealed together enclosing the wafer with the nanopore of interest. The upper reservoir, *source* (S), is separated from the lower reservoir, *drain* (D), by the leak-tight membrane (M) such that transfer of gas can only happen through the nanopore. The wafer is mounted on a support piece (T) that is screwed and sealed to the body of the cell (silver colored). Pressure in the source (inlet) reservoir can be increased while the drain (outlet) reservoir is kept under vacuum. The capillaries leading in and out of the experimental cell are connected to a gas handling system. The flat bottom of the cell can be securely fastened to a metallic surface to ensure a strong thermal link.

flow channel. The space between the Si wafer and the Invar support is the last location to seal in order for the top and bottom reservoirs to be unconnected. This seal is prepared in advance and is achieved using either one of two epoxies: Stycast 2850 or Armstrong A-12 epoxy.

The use of epoxy has a major disadvantage compared to an all-metal joint: helium can diffuse through it. This diffusion is however not detectable at liquid nitrogen temperatures, yet it can be as high as 10^{-16} kg/s at room tempera-

ture. Importantly, it is not possible to reliably correct for this diffusion signal because it is not reproducible and fluctuates in time. All data presented in the thesis is therefore either taken at 77 K, or for mass flows several orders of magnitude larger than the diffusion in the case of room temperature measurements. A second disadvantage of epoxies is that they are at risk of producing volatile compounds that can contaminate the surface of the sample and possibly cover the nanopore. Finally, epoxies need to be cured for extended periods, typically hours, which limits the rapidity of sample preparation. These issues with epoxies have influenced the design of an all-metal experimental cell.

Second Generation Experimental Cell

The second generation of experimental cell was developed with the goal of removing all non-metallic content from the experimental cell. Figure 4.6 shows a cross section of the central region of the second generation experimental cells used to take measurements of mass flow in nanopores. This design is characterized by the removal of the support piece and the use of an indium ring seal located directly under the silicon wafer. A thin Invar disk is used to apply even compression on the wafer, which then compresses the indium underneath it. Once compressed, the indium wire can remain leak-tight over any temperature range attained in our experiments and has the added advantage of requiring only a few minutes of preparation. Additionally, the removal of a compressed indium wire is much simpler than for glues or epoxy sealants since it can be pealed off the surface by applying a gentle upward force.

Both the silver and Invar surfaces touching the wafer are milled flat to

avoid damaging the fragile silicon; rough surfaces can easily lead to cleavage of the whole wafer when some compression is applied. Care must be taken when aligning the free-standing window with the hole in the silver bottom part since the SiN membrane can withstand virtually no physical contact.

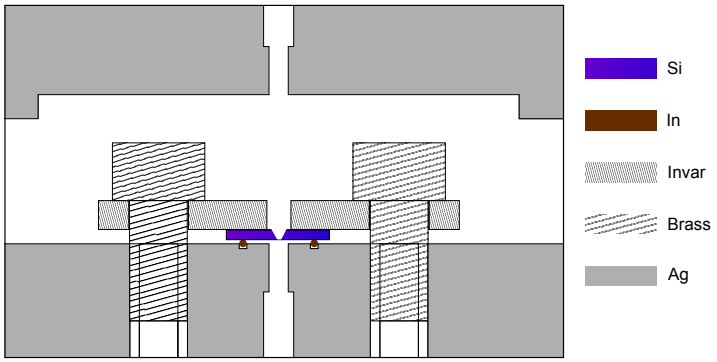

Fig. 4.6 Schematics of a cross section of the central region of the second generation of experimental cells. The top flange and body are made of coin silver ($Ag_{90\%}Cu_{10\%}$), the silicon wafer is compressing an indium o-ring to provide the seal between top and bottom reservoirs and an INVAR 42 disk is used to clamp the wafer. All dimensions are to scale except for the pit of etched silicon. The screws are made of a brass alloy that will contract slightly at lower temperatures to ensure the indium seal remains tight during thermal cycles. A second indium seal (outside of visible area), compressed between the coin silver top and bottom flanges, is used to seal the inside helium from a leak to the outside environment.

The volume above the membrane is designed to be large in order for the helium fluid to thermalize properly with the silver surfaces. A thermometer and a heating coil can be secured directly to the silver parts on the outside of the cell. The helium inlet and oulet capillaries are connected to the cell using adapters screwed on either side of the cell with indium o-rings joints. For low temperature experiments, the inlet capillaries go through multiple stages of heat thermalization as will be explained in section 4.4.

4.3.2 Gas Handling System

The flow of helium through the nanopore is created by the difference in pressure between the top (source reservoir) and bottom (drain reservoir) of the cell. A precise control of the pressure applied above the sample is therefore very important, and this is achieved using a gas handling system (GHS). Figure 4.7 shows a photograph of the GHS. As can be seen from the photograph, multiple pressure gauges are required at specific points in the GHS to monitor processes such as filtration, storage or pressure increase/decrease. All valves and capillaries in the GHS are made of stainless steel with all-metal joints, and all are designed to withstand internal pressure up to 15000 psi ($\sim$1000 atm). The capillaries have an internal diameter of 0.000761 m, which is small enough to ensure that the total volume in the capillaries does not dwarf the experimental cell volume during experiments, but still large enough to have a low impedance to flow compared to the nanopore.

Using helium as the test gas for mass transport experiments has the great advantage that it can be passed through filters at liquid nitrogen temperatures and fine-meshed molecular sieves. Five such filters were used to prevent contamination from air introduced in the cell during sample preparation as well as filter the gas during transfers between components of the GHS. Two of the filters are canisters filled with activated charcoal granules that have a very large surface area because of their natural porosity. The adsorption potential of the surfaces is highly dependent on temperature and keeping this filter immersed in a bath at 77 K can help trap contaminants while letting helium gas through. As long as the filter is kept cold, the molecules will remain trapped.

While helium is conveniently not stopped by the filters, it will be adsorbed by activated charcoal if the temperature is reduced further. This is the principle used in the operation of a helium gas dipstick. A small vessel filled with charcoal is designed such that it can be transferred between a liquid helium bath and a liquid nitrogen one. In the colder environment, the charcoal surfaces adsorb much more helium gas and the pressure in the vessel decreases. Two such dipsticks are part of the GHS and if the valve leading to them is opened, the decrease in pressure can also be used to pump sections of the GHS.

The second important use of the dipsticks is to access large pressures. This pressurization can be achieved once a large quantity of helium gas has been accumulated in the charcoal and the dipstick vessel is returned to the liquid nitrogen bath. The higher temperature induces an instantaneous desorption that creates a pressure build-up. A large gas tank of approximately 0.003 m^3, seen at the bottom of figure 4.7, is filled to an internal pressure of several atmospheres and contains sufficient gas to pressurize the experimental cell well above 100 atm using the thermal cycling of the charcoal dipsticks. This pressurized helium can then be directed towards the experimental cell in order to change the applied pressure on the nanopore. The cycle can be repeated by returning the dipstick to the liquid helium bath and the pressure in the cell can thus be decreased. The whole operation remains in a closed loop cycle.

4.3.3 Electrical Circuit Analogy

As already mentioned, a pressure differential can create a mass current through nanopores. Figure 4.8 shows a simplified representation of the experimental

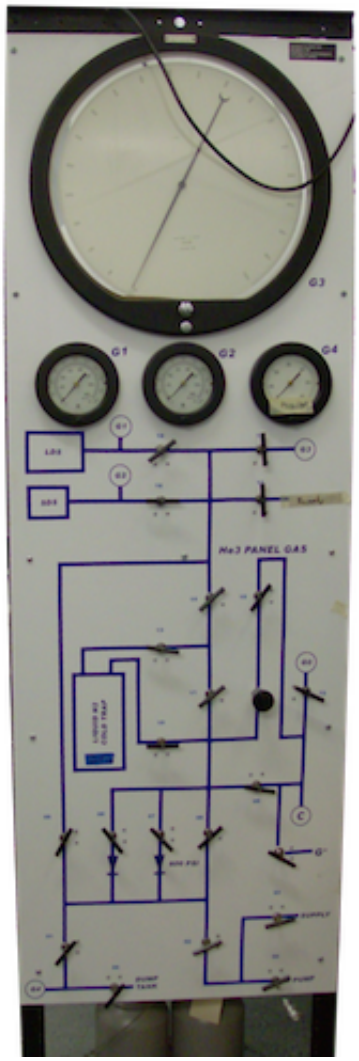

Fig. 4.7 Photograph of a portion of the gas handling system used to control the helium gas. Visible near the top are several pressure gauge displays, high pressure valves connected by stainless steel capillaries and the icons showing the location of other filters, gauges and the experimental cell. A storage tank of ∼3 liters sits at the bottom of the panel. Not shown are the digital pressure gauge, the liquid nitrogen dewar and pressurization dipsticks.

setup to measure a mass current through a linear system like the one proposed here, as well as its electrical circuit equivalent. Figure 4.8A shows an exploded view of the experimental cell with the conductance of the capillaries explicitly

indicated. This finite conductance is in practice positioned in series with the conductance of the nanopore and it should therefore be estimated.

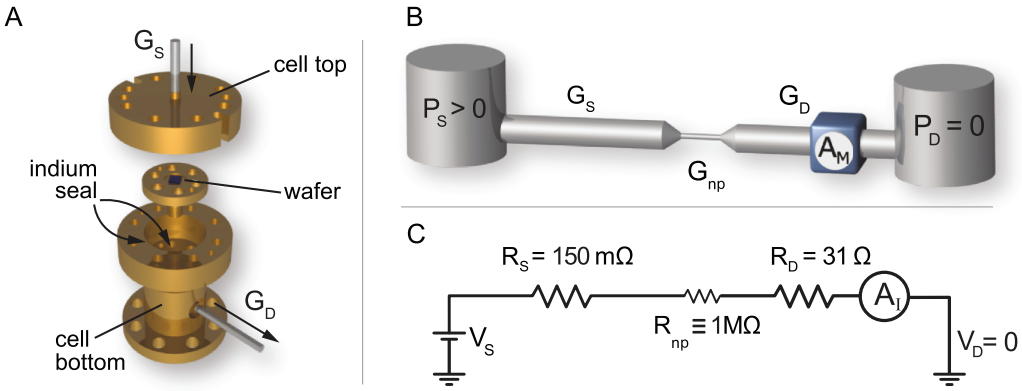

Fig. 4.8 (A) Exploded view of the experimental cell with capillaries leading in and out having respective conductances G_S and G_D. (B) Cartoon diagram (not to scale) of the whole experimental circuit where a reservoir on the left contains pressurized helium traveling in a capillary with a very high conductance estimated using hydrodynamics laminar flow theory. In the middle is a smaller tube representing the nanopore and finally the tubes to the right lead to the mass spectrometer (A_I) that counts atoms. This latter section of the circuit has a high conductance given by the theory of diffusion in tubes under vacuum. (C) An electric circuit equivalent where resistances are shown with proper value relative to one another. Electric current is measured in a similar way to the proposed mass current measurement.

From figure 4.8C, it is clear that the equivalent electrical circuit has many resistances effectively in series and the total resistance of the system is thus the sum of all resistances. The capillaries leading in and out of the experimental cell must have sufficiently small resistances R_{cap} for the nanopore resistance R_{np} to be approximated by the total resistance R_{tot}. In other words,

$$R_{tot} = \sum R_i = R_n \text{ and } R_{np} \gg R_{cap}.$$

Conversely, the conductance of the nanopore must be significantly smaller than the conductance of the other components in the GHS if the measured mass flow is to be attributed only to the nanopore.

The mass flow measured at the mass spectrometer is determined by the total conductance $G_{tot}^{-1} = G_S^{-1} + G_D^{-1} + G_{np}^{-1}$ of the circuit, where $G_{S,D}$ are the source and drain conductances. A calculation of the conductance of the capillaries can be done using the infinite length approximation for Poiseuille flow (equation 3.7) ($G_S \approx 10^{-11}$ m·s at $\sim$1 bar) and Knudsen free-molecular diffusion ($G_D \approx 10^{-13}$ m·s at 10^{-3} mbar) respectively for the inlet and outlet capillaries. In comparison, the typical nanopore conductance is $G_{np} \approx 10^{-18}$ m·s. A more intuitive perspective emerges by completing the analogy with the electrical circuit. As shown in figure 4.8C, setting the nanopore resistance to 1 MΩ and scaling the other elements properly, the resistance of the GHS capillaries are found to be negligible. This comparison makes it clear that the total flow rate measured by the mass spectrometer is attributed only to the nanopore and the effects of the macroscopic capillaries can be neglected.

4.4 Cryogenics and Thermometry

Conducting gas flow experiments at low temperature has a few advantages compared to experiments at room temperature. The first difference is in the proclivity of cold surfaces to adsorb contaminants. In the same way that the cold traps and filters operate, cold surfaces along the path of the helium have an increased potential to capture some of the contaminants that might be present within the gas. In fact, a corollary to this is that desorption off

surfaces is reduced at lower temperatures. Keeping the experimental cell cold can thus help reduce the risk that organic compounds become volatile and block the nanopore. Contamination of the wafer surface has also been observed several times and the nanopores have indeed been blocked on several occasions, especially for smaller diameter nanopores. Most measurements presented in this thesis were taken at temperatures equal to, or below the liquid nitrogen boiling point. The second advantage of working at lower temperatures is the larger signal, which is approximately a factor of two larger because of the $\sqrt{T}$ dependence of Knudsen effusion (equation 3.6) and the density dependence in the viscous flow (equation 3.10). In fact, the next chapter will discuss this temperature dependence in more detail.

The most important advantage of having access to low temperatures is the ability to make clean transport measurements in the liquid state, and more interestingly in the superfluid phase of ^{4}He. To achieve liquefaction of helium and observe the transition to superfluidity, temperatures below 2.17 K are necessary, and this is conveniently well within the reach of a ^{3}He cryostat. Results from experiment using the ^{3}He cryostat will be presented in chapter 6.

4.4.1 The ^{3}He Cryostat

A cryostat consists of a multi-stage cooling apparatus that is inserted into a large dewar designed to minimize transport of heat from the outside environment to the internal components. This dewar consists of several volumes kept either under vacuum or filled with cryogenic liquids. These act as barriers to heat conduction and help reduce the unavoidable heat leaks in the cryostat.

Figure 4.9 presents a simple diagram of the different stages of the "insert" of the ^{3}He cryostat. The main cooling components of the cryostat are the charcoal sorption pump, the 1K-pot, the ^{3}He-pot and the sample stage. All these are kept in a vacuum chamber, which is immersed in the liquid helium bath. The core components of the cryostat were purchased from a commercial supplier (Janis), whereas all experiment specific parts were manufactured and designed by our group. The details of operation of the cryostat follow.

The ^{3}He Cryostat Operation

The ^{3}He cryostat uses a simple evaporative cooling technique to reduce the temperature sequentially from the temperature of a helium bath at saturated vapor pressure, to the temperature of a helium bath at low pressure, and then to the final *base* temperature of a ^{3}He bath at low pressure. The sample stage is in thermal contact with the ^{3}He bath in order to take advantage of the coldest location. The base temperature is between 260 mK and 340 mK depending on the thermal leaks caused by capillaries and conducting wires anchored above at higher temperatures.

The first stage of the cooling procedure is to thermalize all the insert components with the helium bath. This is achieved by introducing helium gas inside the vacuum chamber such that heat from the insert is conducted to the vacuum chamber walls that are in direct contact with the helium bath. Once the temperature of all elements on the insert reaches 4.2 K, the exchange gas is removed such that the vacuum chamber acts as insulation between the chamber wall and the insert components. This is a necessary step in order to reach

colder temperatures.

The next step is to let some liquid helium from the helium bath enter the chamber called the "1 K pot", through the needle valve seen on figure 4.9. If the vapor pressure of the liquid helium inside the 1 K stage is reduced by pumping on it, the thermodynamic equilibrium shifts and the temperature decreases as more helium evaporates to replace the atoms removed by pumping. This situation can be stabilized by supplying warm liquid helium at ∼4 K to balance the evaporated gas being pumped away. In this manner, a temperature of ∼1 K can be maintained under optimal conditions. If the balance is slightly shifted, for example by increasing the pumping rate of the gas or reducing the influx of liquid, the overall temperature will decrease, albeit for a limited period. This unbalanced situation would slowly reduce the ratio of liquid to gas and once all the liquid is evaporated, the cooling would stop and the ever present heat leaks would cause the temperature to increase sharply. A more desirable solution for sustained operation is to keep a balanced pumping rate versus liquid injection. This balance can be achieved in practice for extended periods and temperature remains stable within a few millikelvins.

Cooling to base temperature is achieved in the ^{3}He chamber with the same evaporative cooling technique described above. The scarcity of ^{3}He gas makes it impractical to have a continuous supply of atoms and the design is therefore made for closed-cycle operation. It would be too costly[1] to pump away the ^{3}He gas. Only a few liters of gaseous ^{3}He is therefore kept in a storage container at room temperature. This storage container is welded to a tube that passes

[1]Current prices can be as high as ∼$8000 per liter of gaseous ^{3}He at STP.

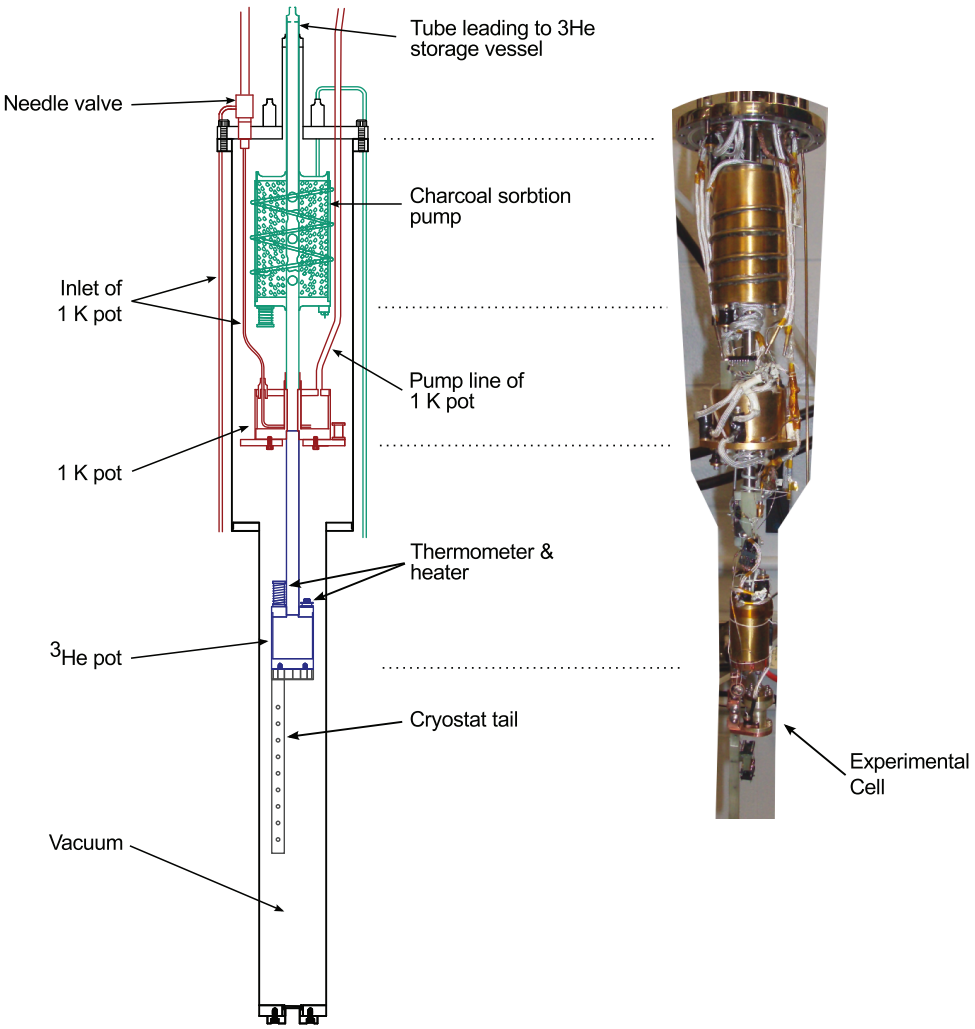

Fig. 4.9 Diagram of the principal ^{3}He cryostat components. (In black) The vacuum chamber immersed in the helium bath of the external dewar. (In teal) Charcoal sorption pump parts. The central tube leads to a storage vessel above (not visible) and, below, connects to the ^{3}He pot (in green). (In red) The liquid helium inlet letting liquid into the 1 K pot, passing through the needle valve. On the opposite side is a pumping line. (In grey) The coldest point of the insert and the volume dedicated for samples. On the right side is a photograph of the insert matching the schematics on the left. The diagram is modified from CAD drawings by the manufacturers, Janis Research Company, LLC.

through the center of the cryostat insert and ends in the ^{3}He chamber where the evaporative cooling can occur. As shown in figure 4.9, a charcoal-filled chamber is also present in the middle of this closed system such that ^{3}He atoms are always free to move between the room temperature storage vessel, the charcoal filled canister, and the ^{3}He pot.

At this point in the cooldown procedure of the cryostat, all components are at 4 K except the 1 K pot where evaporative cooling of ^{4}He is taking place. As explained in the case of the pressure building dipsticks, activated charcoal becomes very efficient at adsorbing atoms when cooled down to liquid helium temperatures. Having a chamber filled with charcoal directly connected to the stored ^{3}He from the storage container, which remains at room temperature at all times, most of the ^{3}He gas will get adsorbed by the charcoal. This means that the charcoal chamber acts as a temperature-controlled pump and is the reason why this component is also called a charcoal sorption pump.

A section of the tube leading from the charcoal sorption pump to the ^{3}He pot passes through the 1 K pot such that some ^{3}He gas can condense on the inner walls of the tube if the 1 K pot temperature is reduced below approximately 1.8 K. By raising the temperature of the charcoal chamber above $\sim$37 K, it is possible to reduce the adsorption potential in a way that ^{3}He gas will desorb and fill the whole closed system volume. The resulting increased pressure induces liquefaction of some ^{3}He atoms when coming in contact with the tube region cooled by the 1 K pot. The gas will continue to condense and fill the bottom reservoir with liquid ^{3}He. It should be clear that no mixing of the two isotopes occurs throughout this procedure, unlike

in the case of the dilution refrigerator cryostats. Heat transfer is exclusively by diffusion through the metallic structure.

Once all available atoms are condensed, the temperature of the charcoal can be lowered by pumping on the liquid ^{3}He. This will lower the temperature of the ^{3}He bath and the samples in thermal contact with it. The colder the charcoal is, the more ^{3}He can be adsorbed and the more pumping power is available to increase evaporation of ^{3}He atoms and reduce the temperature of the remaining liquid in the ^{3}He pot. In practice, this pumping-dependent temperature control only offers a coarse modulation of the sample temperature, and usually has to be supplemented with one or several heating elements that can be fine-tuned to balance the power input (heating) to the cooling power of the cryostat and regulate temperature with millikelvin temperatures. This fine-tuning is achieved through a feedback loop between a thermometer and a heating element.

Temperature Control

A Lakeshore temperature controller model 340 was used to control a PID loop between a 25 Ω heater and a ruthenium oxide thermometer, both affixed to the experimental cell. The P, I and D coefficients where adjusted manually in each temperature range for efficient temperature modulation compared to the set-points chosen.

Given that the cooling power of the cryostat at base temperature is on the order of milliwatts, the 25 Ω resistor used for heating the sample can easily raise the temperature sharply and the proportional (P) coefficient was

therefore kept low (<5) to avoid uncontrolled warming that could potentially induce boiling of the liquid helium inside the cell. This is especially relevant in the superfluid transport experiments where temperature changes of a few milli-Kelvin where often desired. The "I" coefficient was simply chosen to avoid underdamped/overdamped oscillations of the temperature with respect to the temperature set-point. The experiments I performed with the cryostat never required the setpoints to depend on time ($\partial T_{set}/\partial t = 0$) so D = 0 was the *de facto* value for the derivative component in all PID loop operation.

It is worth noting that the temperature control loop is only effective if the temperature is measured accurately. This means a thermometer with high precision must be used and the thermometer must be securely fastened to the component of interest so that a possible temperature gradient does not affect the accuracy of the reading. These two requirements are covered in the next subsection.

4.4.2 Thermometry and Thermal Anchoring

The helium used in the experiments is stored in the GHS at room temperature, so efficient cooling of the gas is necessary in order for transport measurements to be realized at low temperatures and in the liquid phase. Reducing the temperature of the gas can be achieved by letting it go through a volume with cold surfaces, as was explained in section 4.3.2. The simplest option for this cooling is to have the experimental cell submerged in a cryo-liquid, along with a section of the capillary, such that gas from the inlet capillary is cooled and thermalizes within the cell. This is the method that was used for most

measurements in chapter 5 and was shown to be effective for temperatures at and above the liquid nitrogen boiling point.

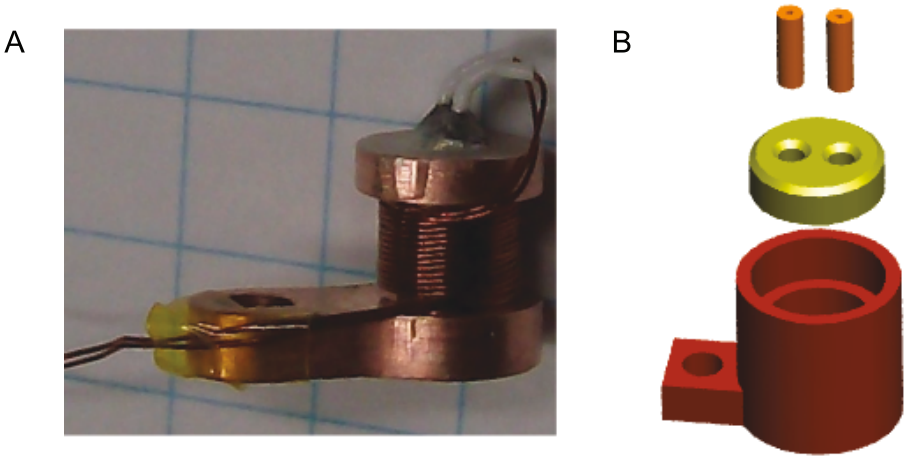

Fig. 4.10 (A) Thermometer inside an OFHC copper piece milled in a bobbin shape so that the electrical leads can be wound around the post to ensure that the whole unit is well thermalized. The ruthenium oxide resistive element is (hidden from view) inside the bobbin within a protective canister. (B) Exploded view of a heat exchanger where the bottom part is filled with pressure-sintered silver powder and capillaries are soldered to the two posts. These posts are brazed to the top of the small container. Superfluid helium entering from one capillary into the heat exchanger will rapidly fill the silver powder's crevices and be in thermal contact with the whole unit.

The second option is to use multiple cooling stages called thermal anchors (figure 4.10B). This method of cooling is required for experiments in the cryostat where the energy from the warm gas could easily overwhelm the cooling power of the ^{3}He pot and prevent proper operation. The strategy is therefore to force the gas from room temperature through increasingly cold thermal anchors to remove as much energy as possible before letting the gas thermalize with the cell. Specifically, I used a thermal anchor on the vacuum can at 4.2

K, another on the 1 K pot and a last one on the ^{3}He pot. It should be noted that the capillary from the outlet of the experimental cell was kept insulated all the way to the vacuum can's thermal anchor. This capillary was made of an alloy of copper and nickel with a thermal conductivity on the order of $\mathcal{O}(10)^{-4}$ W/cmK, on par with Teflon and manganin, and an order of magnitude lower than standard metals. Since this tube is $\sim$60 cm long, it does not represent a serious heat leak to the bottom of the cell. As mentioned in section 4.3.1, we chose coin-silver as the material for the experimental cell because of its large thermal conductivity, which allows the helium to quickly thermalize. The cell's thermal conductivity is also necessary to measure the temperature with thermometers affixed to the body of the cell. It is a good practice to securely fasten thermometers and heaters directly on the experimental cell to minimize the risk of temperature gradients.

Several thermometers (figure 4.10A) are monitored continuously during operation of the cryostat and all of them use a 4-point measurement technique to avoid the effects of the change in lead resistance as a function of temperature. Both the sorption pump and the 1 K pot where monitored with silicon diode thermometers and both the ^{3}He pot and the cell had ruthenium-oxide ones. The latter thermometers where calibrated at NIST and all temperatures quoted in the thesis where converted from Ohms to Kelvin using this calibration.

Finally, I built heaters using a design similar to that seen for the thermometer in figure 4.10A. Specifically, I wound a length of highly resistive 0.1 mm manganin wire tightly around a post, such that driving a current through the

wire would warm it up via Joule heating, $P = R_{heater} \cdot I^2$. The voltage used to produce heat in these bobbins can be precisely controlled with the PID loop, as long as a thermometer is positioned nearby.

Chapter 5

Flow Conductance of a Single Nanopore

5.1 Mass Flow in a Single Nanopore

The first mass transport experiments I present in this chapter were performed to test our experimental scheme and determine whether a quantitative measurement could be achieved with a mass spectrometer. This proof-of-concept [91] set the foundation for the analysis of all subsequent mass transport measurements. The first sample for which the mass flow was investigated (shown in figure 4.2B) had a diameter of 101±2 nm as measured from the TEM image, and a membrane thickness of 50 nm. These measurements were conducted in a first-generation experimental cell similar to the one shown in figure 4.5. As explained in detail in chapter 4, the conductance G of a channel can be determined from the mass flow Q measured as a function of the pressure applied across both sides of that channel, $\Delta P = P^{top} - P^{bottom}$. Keeping the bottom

reservoir of the experimental cell at zero pressure, $P^{bottom} \approx 0$ ensures that the pressure differential is in practice equal to the pressure of the inlet (source) reservoir above the membrane, $\Delta P \equiv P^{top} - P^{bottom} \approx P^{top}$. Varying P^{top} then induces a change in the mass flow, *i.e.* $P_1^{top} \rightarrow P_2^{top} \Rightarrow Q_1 \rightarrow Q_2$ that we can detect with the Smart Test leak detector.

5.1.1 Measurement of Helium Gas Flow

Using the measurement scheme described in the previous chapter, I measured the mass flow through the 101 nm nanopore for a series of pressure differential applied across the sample at temperatures between liquid nitrogen and room temperature. When changing the pressure in discrete steps from one set-point to another, the signal measured changes asymptotically towards the next stable value. In other words, the mass flow signal has a transient time of equilibration before the system stabilizes, leading to an inverse exponential (equation 5.1) behavior after the pressure is increased in a single finite step.

$$Q(t, P) = Q_i(P_i) + A_i \cdot e^{-t/\tau} \tag{5.1}$$

The equilibrium time constant τ varies between a few seconds to almost 2000 s depending on the experimental configuration used. For example, the equilibration time constant of the results in figure 5.1 was 17.5 ± 0.8 s. The addition of cold filters and longer capillaries in recent modifications to our apparatus increased the impedance to the flow of gas going towards the leak detector. This resulted in much longer equilibration times for each flow measurements, and thus reduced the total number of data points that could be obtained.

Typically, after a duration equivalent to $\sim 2\tau$, the mass flow Q_i corresponding to the applied pressure P_i can be determined by applying a non-linear fit to the time-dependent signal. An example of this is shown in figure 5.1, where the red line is a portion of the exponential decay curve fitted to the mass flow data (dots). In this example, the data show stepwise decreases in pressure leading to descending stair-like mass flow signal as a function of time. This procedure can be repeated multiple times, either in ascending or descending pressure steps.

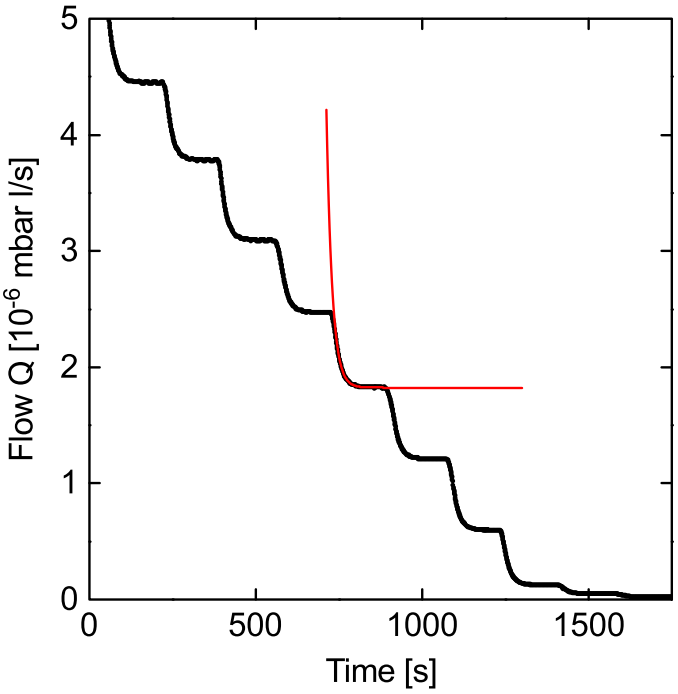

Fig. 5.1 Volumetric flow through a single 101 nm nanopore during an experiment as the pressure differential is decreased in stepwise fashion. When the pressure is decreased and left at a stable value, the response of the flow signal exponentially approaches a new equilibrium value. In red is the non-linear fit of equation 5.1 used to extract the equilibrium value at a given pressure.

Once all data points $Q(P_i)$ are extracted from the time-dependent signal,

the mass flow as a function of applied pressure is explicitly obtained (see figure 5.2). These measurements are, however, subject to a systematic uncertainty caused by a residual "background signal" in the mass spectrometer. This signal offset is corrected by subtracting a constant to all flow signal and, in effect, enforces the condition $Q(P = 0) \equiv 0$. In general, the absolute value of the offset depends on the state of the leak detector, but is normally $<5{\cdot}10^{-10}$ mbar·l/s (using the same units as in figures 5.2 and 5.3A). This systematic error is always corrected, even if it is typically, at most, a few percent of the smallest flow measured. Indeed, the majority of flow measurements are several orders of magnitude larger than this correction. The final error in the conductance is usually dominated by the propagated uncertainty from the leak detector signal, the error in the pressure, and the temperature reading.

One clear observation that can be made regarding the data in figure 5.2 is that they deviate from the linear relationship shown by the red line. This indicates that the nanopore conductance changes throughout the experiment as the internal pressure of the gas above the nanopore increases.

5.1.2 Conductance of a Single 101 nm Nanopore

Using the definition of conductance $G \equiv Q/\Delta P$, we can plot the nanopore conductance as a function of the pressure applied, or equivalently as a function of the Knudsen number Kn= λ/D. Figure 5.3 shows the conductance of the nanopore at 77 K for pressures up to 38 bar. The variation in mean-free-path λ of nearly four orders of magnitude induces a clear change in the flow regime through the sample. The three smaller graphs of figure 5.3A contain

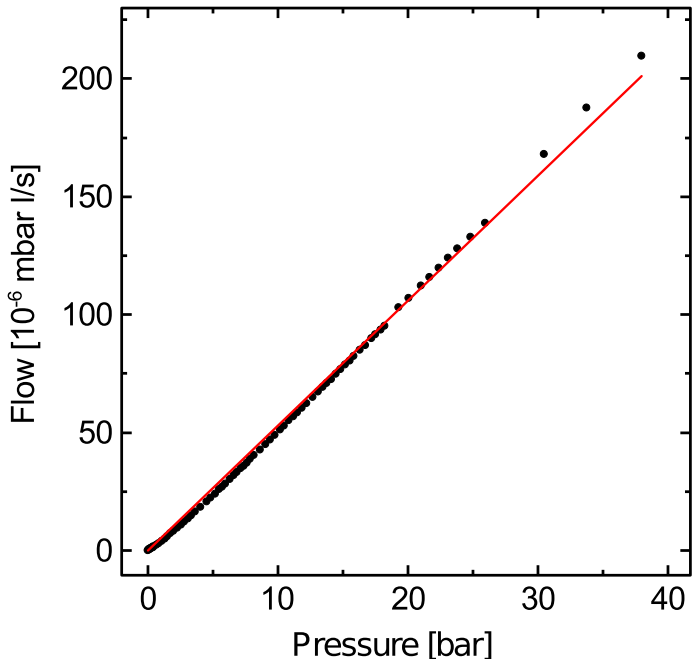

Fig. 5.2 Mass flow as a function of the pressure applied on a 101 nm diameter pore. The red straight line is a guide to the eye to accentuate the non-linearity of the data.

the same mass flow data as in figure 5.2, but segmented to better illustrate the flow behavior. The first distinct pressure range P $\approx 0 - 55$ mbar (green background) shows very good linearity whereas the range P $\approx 0.69 - 5$ bar (beige background) and P > 6.2 bar (blue background) show strong and weak departure from linearity, respectively. Easy comparison to the conductance data of figure 5.3B can be done using the background color corresponding to each flow regime. The first observation one can make regarding the conductance data in figure 5.3B is that it is indeed non-constant as the properties of the gas change. A constant conductance leads to a linear relationship between pressure and flow as can be seen, for example, in the low pressure points on the bottom left graph of Fig. 5.3A. This linearity is then broken for flows at

larger pressure differentials. The detailed dependence of flow on the pressure is easier to visualize if we further analyze the conductance of the pore.

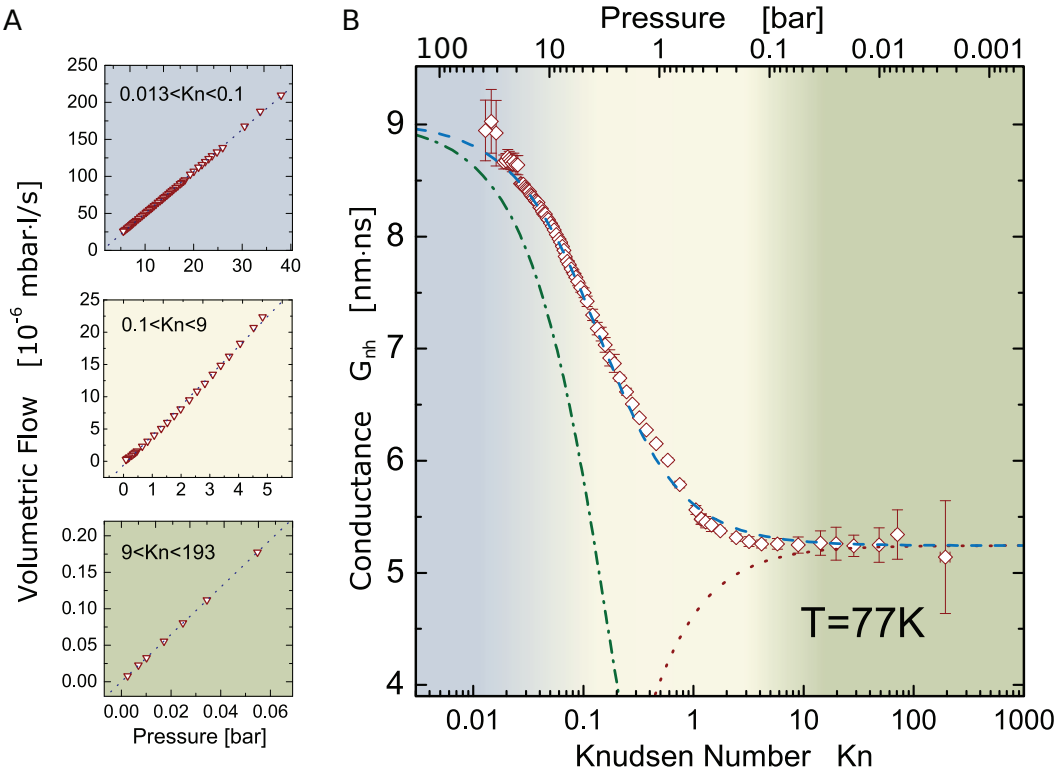

Fig. 5.3 (A) Volumetric mass flow of helium gas for three different ranges of pressure. The color of the background corresponds between figure A and B to distinguish between flow regimes. In green is the Knudsen effusion region, in blue is the continuum hydrodynamics viscous flow region and in between (beige) is the transition region. (B) Conductance as a function of Knudsen number applied on a 101 nm diameter pore. The dotted red line is the Knudsen effusion contribution, the green dash-dotted line is the viscous short-pipe laminar flow contribution and the dashed blue line is the total flow fitted to the data.

Extracting an Effective Radius

The constant conductance observed at high Knudsen number is consistent with the Knudsen effusion for finite-length channels. As noted in chapter 3, the short pipe conductance in the Knudsen regime is given by equation 3.6 and fitting it to the data above Kn = 10 with L = 50 nm gives a radius of 50.0±0.2 nm. This is within 1% of the radius extracted from the TEM image of the nanopore and is within its uncertainty. The high precision of the radius one can extract by modeling the conductance of a single nanopore in the free-molecular regime thus gives an *in situ* tool to confirm the status of nanopores during experiments. Indeed, as I will show in subsequent sections, this same fitting procedure can be used to quantitatively determine the nanopore dimension and could alleviate the need for TEM imaging.

Modeling of the Transition Flow

Given the accuracy of the Knudsen effusion fit to determine the radius of the nanopore, we attempted to model the conductance over the whole transitional region. In order to do this, we used a method similar to the one presented in references [92] and [93]. The authors of these works developed a model for channel flows when the Knudsen number is in the transitional region. When this is the case, the continuum assumptions begin to break down close to the walls, in the so-called Knudsen layer. Within this layer, interactions at the walls are affected by rarefaction effects and the "no-slip" assumption on the walls can no longer apply. The emergence of a Knudsen layer as the fluid approaches Kn $\approx 10^{-2}$ has an effect equivalent to allowing a finite slip at the

wall-fluid interface and a correction must be applied to the continuum equation. This correction is expected to scale with the Knudsen number throughout the transitional region until the flow is completely dominated by the rarefaction effects.

The authors in [92] have derived the channel flow rate expected in pipes and ducts,

$$Q = \frac{\pi R^4 \bar{P}}{8\eta_0 k_B T}\frac{\Delta P}{L}(1 + aKn)\left(1 + \frac{4}{1 - bKn}\right), \tag{5.2}$$

where $\bar{P}$ is the average pressure in the channel and η_0 is the dynamic viscosity of the fluid in the bulk. The first term outside the parenthesis is essentially the continuum pipe flow found in equation 3.7. The second parenthesis is a correction to the diffusion (*i.e.* acting on the viscosity η) for the generalized slip model. In theory, the breakdown of the continuum hypothesis, *i.e.* the rise of a slip boundary condition, acts as a reduction of the effective viscosity μ and an increase in the flow rate predicted with respect to the non-corrected viscous flow model. The parameter b has been found to best fit molecular dynamics simulations for a value of $b = -1$. The remaining term, within the first parenthesis, is a rarefaction correction $C_r = (1 + a\mathrm{Kn})$, where a must transition "from zero in the slip flow regime to its asymptotic constant value in the free molecular flow regime"[92]. Equation 5.2 can thus be re-written in terms of a viscous flow rate in the slip regime Q^{slip},

$$Q^{total} = Q^{slip} \cdot C_r(\mathrm{Kn}). \tag{5.3}$$

Beskok *et al.* [92] have chosen a definition of the correction C_r such that Q^{total} remains valid throughout the transitional region. Specifically, the parameter a acts as a smoothly increasing function of Kn of the form

$$a = a_0 \frac{2}{\pi} atan(a_1 \mathrm{Kn}^{\beta}),$$

such that the total flow remains equal to Q^{slip} at $\mathrm{Kn} \ll 1$ and reaches the molecular free flow asymptotically with Kn increasing. The two free parameters, a_1 and β are fit parameters defining the curvature of the transition between the two regimes and a_0 can be chosen as the value of the free-molecular flow rate.

While we can use the same arguments to model the flow in our nanopores, as explained above, the aspect ratio of our nanopores is too close to unity to warrant the use of the long pipe approximation (Eq. 3.7). A better model in the continuum regime, for short-pipes, is given by equation 3.10. Equivalently, at the other limit of large Kn, we know the total flow must be equal to the Knudsen effusion of equation 3.6. The smooth cross-over between the two limiting flows can be accomplished with a correction similar to C_r. We define

$$G_{total} = G_{continuum}^{short-pipe} + \frac{2}{\pi} \mathrm{atan}(\sigma \mathrm{Kn}) \cdot G_{Knudsen}^{short-pipe}, \tag{5.4}$$

as the nanopore conductance over the whole transitional region ($0.01<\mathrm{Kn}<10$). Here, the normalization of the arc-tangent ensures an asymptotic conductance of the nanopore at large Kn and the fit parameter σ smoothly modulates the emergence of rarefaction effects in the nanopores. The first term on the

right-hand side is the conductance of a pore described by equation 3.10. The term $G_{continuum}^{short-pipe}$ also contains the parameter α, which can thus be treated as a phenomenological constant specific to the solid-state nanoholes used in our experiments.

Using equation 5.4 to fit the whole dataset shown in figure 5.3, we found parameters $\alpha = 4.69 \pm 0.06$ and $\sigma = 5.3 \pm 0.1$. In this case, α is larger than what was predicted in macroscopic apertures [56], which may indicate that more important corrections from the end effects are required. The second parameter (σ) defines a smooth cut-off point where rarefaction effects dissipate. A larger value in σ translates into a larger contribution from effusion in the transition region. The dotted red line in figure 5.3 is the Knudsen component ($G_{Knudsen}^{short-pipe}$) of the total conductance. For completeness, the green dashed line shows the viscous hydrodynamics-type component $G_{continuum}^{short-pipe}$.

Our data are limited by the maximum pressure that can be applied before inelastic deformations of the membrane occur. With this sample, the lowest Knudsen number we could attain was Kn = 0.013. Strictly speaking, this is not yet within the purely viscous laminar flow region and this limits the accuracy of α. In principle, to reach the laminar viscous flow regime with no-slip boundary condition, we need Kn $\leq$ 0.001, which means a pressure approximately 13 times higher than that which was used in the present experiment. This is currently not possible with the solid-state membranes, it however represents an alternative avenue for investigation if sufficiently sturdy membranes were fabricated. Strickly speaking, the other option to reach Kn $\leq$ 0.001 is to increase the diameter of the pores, but this is contrary to our stated goal of

investigating nanofluidics.

5.1.3 Temperature Dependence of Conductance

In order to deepen our understanding of the crossover between the hydrodynamics of viscous flow and the free-molecular Knudsen effusion, we conducted a thorough investigation of the temperature dependence of the gas flow between 77 K and 295 K. To achieve this, we slowly varied the temperature of the experimental cell by exposing it to cold nitrogen gas above a liquid nitrogen bath. The decrease in temperature of the gas within the cell induced a drop in pressure that could be monitored with a 0.001psi precision. Since the gas handling panel supplying the gas remains at room temperature, one can view this system as two volumes V_{GHS} and V_{cell} that are at different temperatures but connected by a negligibly small capillary allowing particles through such that at equilibrium, pressure is the same in each volume. This is in fact the very basis of a gas thermometer [94, 95].

Fixing the initial pressure applied on the nanopore, the flow was measured continuously as the cell was cooled down and warmed back up. The conductance was calculated for the whole temperature range such that the temperature dependence could be characterized. Two examples of these datasets are shown in the inset to figure 5.4. Seen with log-log axes, one can visualize the linear relationship characteristic of a power-law dependence on temperature $G \propto T^{-n}$. A single exponent "n" was extracted from each similar dataset.

As noted above, the equilibrated pressure of the whole system decreases monotonically with the temperature of the cell. Taking the specific example of

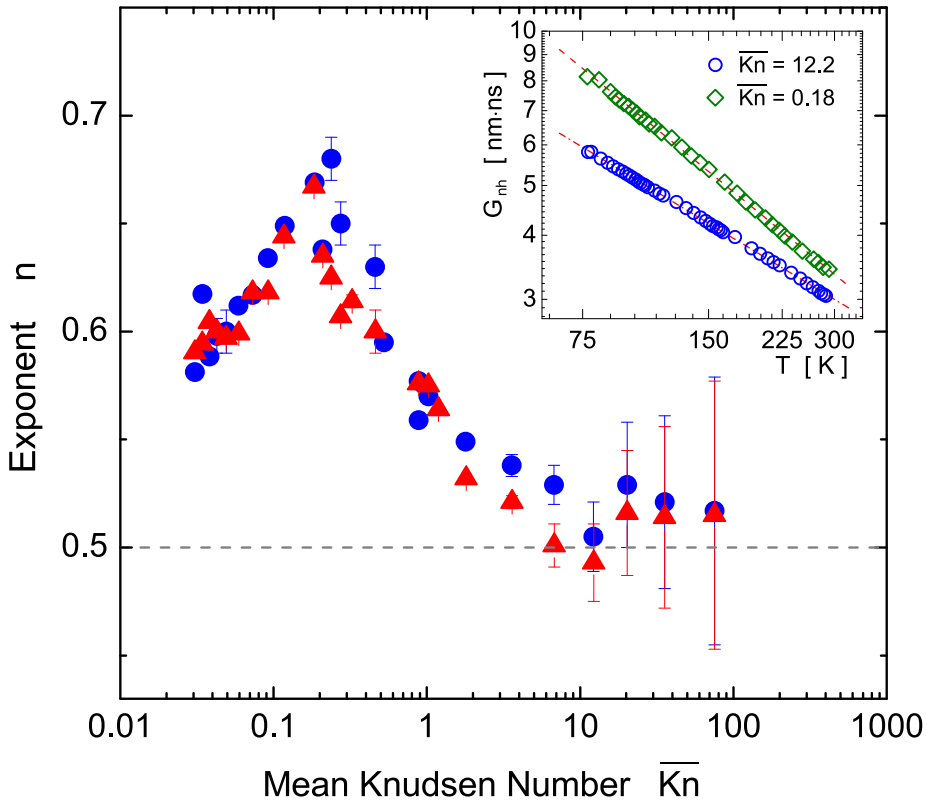

Fig. 5.4 The power law exponent of the temperature dependence of conductance in a single 101 nm nanopore. The mean Knudsen number $\overline{\mathrm{Kn}}$ is used to position the points on the Knudsen scale. The inset shows a log-log plot of the conductance for temperatures between the liquid nitrogen boiling point and room temperature. The slope of these points gives the power law exponent shown in the main figure. A dashed line is shown at 0.5 as a guide to the eye for the $1/\sqrt{T}$ relationship expected for Knudsen effusion.

the data with green diamonds (Fig. 5.4 inset), the initial pressure, in the case where the whole system was at room temperature, was 6.60 bar decreasing to 6.08 bar after cooling the cell to 77 K. These two pressures each have an associated Knudsen number, Kn = 0.286 at T = 295 K and Kn = 0.083 at T = 77 K. We chose to take the mean value $\overline{\mathrm{Kn}}$ to plot the exponent n as a function of Knudsen number. In effect, this means the dataset with green

diamonds in the inset of figure 5.4 gives a point at $\overline{\mathrm{Kn}} = 0.18$ and the one with blue circles has $\overline{\mathrm{Kn}} = 12.2$. A series of similar curves was measured for initial conditions spanning the whole transition region. The exponent in the power-law dependence on temperature of conductance for all available gas pressures are shown in figure 5.4. In the Knudsen effusion regime, a $G \propto 1/\sqrt{T}$ is explicitly present and the corresponding exponent $n = 0.5$ is shown with a dashed line on the graph.

The exponent extracted from the dependence on temperature shows clear departure from a purely inverse square root behavior at $\overline{\mathrm{Kn}} \lesssim 10$. The exponent increases slowly until it peaks to $n \simeq 0.67$ at $\overline{\mathrm{Kn}} \simeq 0.2$ and then starts falling off to $n \sim 0.58$ for the highest pressure attainable in the experiment. The fall-off behavior observed below $\overline{\mathrm{Kn}} \simeq 0.2$ can be interpreted as the crossover towards a conductance dominated by finite-sized viscous flow. Indeed, taking the large pressure limit of the conductance in the short-pipe viscous flow (equation 3.10) and expanding the density of helium gas into its dependence on pressure and temperature, we obtain a short-pipe conductance limit at high pressure of $G_{viscous}^{\Delta P \to \infty} = \pi R^2 \sqrt{\frac{m}{\alpha k_B T}}$. This asymptotic limit of the conductance in short pipe has the inverse square root dependence on temperature that figure 5.4 hints at. The lack of a pressure dependence in the latter equation is expected to lead to a plateau for the conductance, unfortunately our data did not quite reach this regime, as can be seen in the low Knudsen number data points of figure 5.3.

5.2 Knudsen Effusion in Smaller Pores

The positive results obtained with the ∼100 nm pore constitute a foundation for measurements in smaller pores. We have subsequently measured the mass flow in dozens of nanopores with progressively smaller diameters and selected a few to demonstrate the applicability of our method as we move towards the 1D limit. The conductance of each of these samples was obtained and then fitted with the model of section 5.1.2. Several of these results are presented in the remainder of chapter 5. The selected fit and conductances are shown in a way such that each graph illustrates a different aspect of the model, as well as demonstrates the repeatability of our measurements. Whenever possible, measurements were performed at both room and liquid nitrogen temperature, and a fit with equation 5.4 was computed when the diffusion through the epoxy was negligible. Whether measurements were achieved with increasing or decreasing steps in pressure across the nanopores did not yield different results and the direction of the pressure change is therefore not distinguished in the following sections.

5.2.1 Applicability of the Method in Smaller Nanopores

Figure 5.5 shows the conductance of two nanopore samples with diameters of 77 ± 1 nm and 46.5 ± 1 nm, as measured from TEM images. Each sample has its associated picture inset in the graph of the conductance. Both wafers used to produce these nanopores had a thickness of 50 nm.

For the sample shown in A, the mass flow was measured at pressures between 4.7 mbar and 17.7 bar. The conductance inferred from that flow mea-

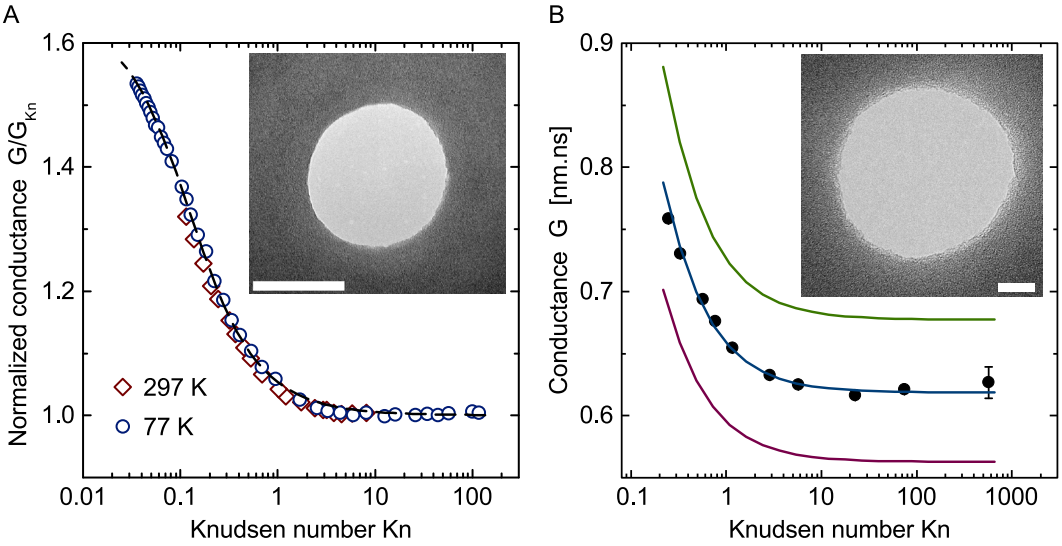

Fig. 5.5 (A) Normalized conductance of a 77 nm diameter nanopore for 297 and 77 K. The conductance data are normalized with the experimental conductance in the Knudsen regime in each data set. The dashed line is computed with equation 5.4 fitted to the 77 K conductance data. (B) Conductance at room temperature for the sample seen in the inset. The diameter from TEM is measured to be 46.5 ± 1 nm. Overlaid on the data are the phenomenological model equations with radii equal to the TEM dimension (blue) and ± 1 nm for green and magenta curves, respectively. The white bar on the TEM image is 50 nm for A and 10 nm for B.

surement was then normalized with the experimental conductance in the Knudsen effusion regime $G^{Kn}_{exp.}$ =3.78·10^{-18} m·s (1.91·10^{-18} m·s) for 77 K (295 K). The two curves are qualitatively very similar and this demonstrates that our modeling of the flow is not dependent on the temperature at which the gas flow measurements were performed.

The fit to the conductance in 5.5A is shown with a dashed line. Here, the blue circles are data at low temperature (77 K) and red diamonds at ambient temperature (295 K). The Knudsen effusion predicted by equation 3.6 for a cylindrical channel with a diameter of 77 nm is lower than the experimental

conductance (for $Kn > 10$). We attribute this discrepancy to the fact that our samples are not perfect cylinders and, as explained in section 3.2.1, the opening angle of nanopores affects the Clausing factor, thus changing the conductance. Using the opening angle as a fit parameter, we find an 11° angle for the sample in figure 5.5A. Once this correction to the Knudsen effusion model is applied, the conductance over the whole transition region can be fit with equation 5.4. The parameters $\alpha = 3.1 \pm 0.1$ and $\sigma = 13 \pm 2$ were found for the two datasets of figure 5.5A. For technical reasons,related to the protection of the sample, the dataset at low temperature spans a much broader region of the Knudsen scale and only the fit to this data is shown.

The same procedure was applied on the sample shown in figure 5.5B where only the room temperature data are available (because of the type of sealant that was used to prepare the SiN wafer). The fit to the high Knudsen number conductance had to be corrected again for the pore geometry and an angle of 11.5° was required to fit the experimental flow. The green and magenta curves in figure 5.5B are produced using equation 5.4 with a radius modified by ±1 nm, which corresponds to the uncertainty from the dimensions measured on the TEM image. This comparison of slightly different radii demonstrates the sensitivity of our measurement scheme. Specifically, a reduction in the diameter of a nanopore by either contaminants or structural deformation of the SiN membrane can have easily detectable changes in the conductance.

5.2.2 Evidence of Nanopore Deformation

In order to further investigate the sensitivity of the mass flow on the dimensions of the pore, we have repeatedly measured the flow through samples of various length-to-radius (L/R) ratio and over extended periods of time. Specifically, we have extracted the conductance of a given sample for a series of time intervals following initial drilling, and correlated these measurements with TEM imaging. A summary of the results of this series of experiments is available in appendix A and a selection of two samples is shown here to demonstrate the main findings.

Figure 5.6A shows the conductance of a 41 ± 2 nm nanopore, while figure 5.6B shows a 25 ± 1 nm diameter pore, as measured from TEM imaging directly after fabrication. The thicknesses of these samples are 50 nm and 75 nm, corresponding to L/R ratios of 2.4 and 3.0, respectively. As has been observed elsewhere [96], the larger this ratio, the more likely it is that a deformation of the nanopore will occur over extended periods of time. For the sample shown in the inset of 5.6A, the conductance was measured at 77 K for two consecutive days. The measurement shows a slight offset between the first day (teal circles) and the second day (blue diamonds). This illustrates that the typical amplitude shift of the conductance can be observed in the first few days after fabrication for nanopores with comparable geometries.

The fitting of data at high Knudsen number yields a radius of 20.43 nm and 20.36 nm for the teal and blue data, respectively. This radius is within the uncertainty from the TEM imaging and the small shift is within our expectations for a local deformation of the nanopore walls. Monitoring the Knudsen effusion

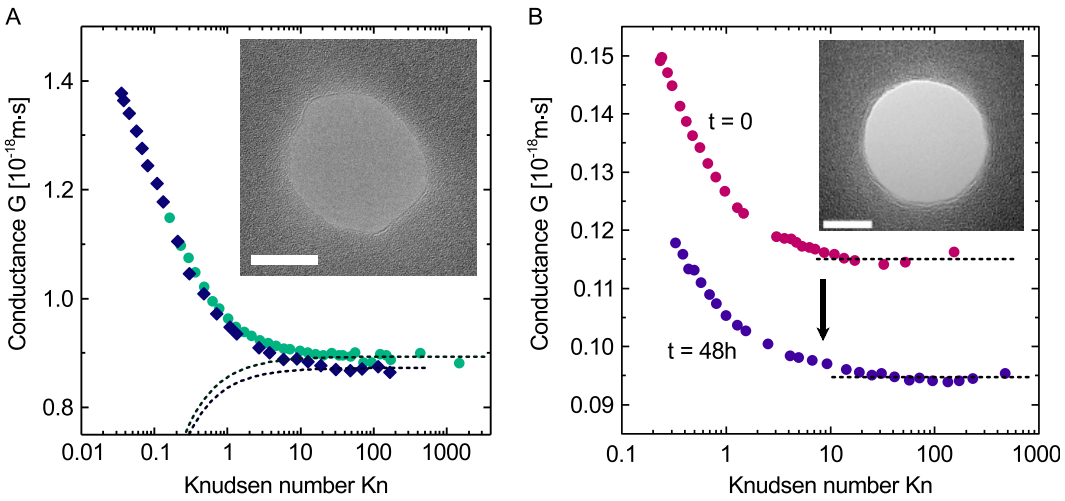

Fig. 5.6 Conductance of 41 nm (A) and 25 nm (B) diameter nanopores as a function of the Knudsen number. Dotted lines are Knudsen effusion contribution to total conductance in A and a constant function fit the data at high Knudsen number. In both cases, a slight shift in the conductance is detected between measurements made several hours apart. The white bar on the TEM image is 20 nm long in A and 10 nm in B.

in nanopores over time can thus be used to determine when the pore dimensions become stable. When this is the case, subsequent experiments can be performed reliably. This is important, since I have once observed a nanopore gradually being blocked by contaminants and become fully obstructed during a continuous measurement of mass flow in the Knudsen regime.

A more dramatic change was observed in the sample shown in the inset of figure 5.6B (also shown in figure 4.2E) and whose room temperature conductance in the Knudsen regime was found to drop by ∼21% over 48 hours. These conductance data are shown in figure 5.6B, where the dotted lines are fit for Kn >10 of $1.15 \cdot 10^{-19}$ m·s and $0.94 \cdot 10^{-19}$ m·s. This corresponds to a decrease in fitted radius from 12.7 to 11.7 nm with a constant opening angle

of 5°. The observation of such a sharp decrease in conductance for samples with similar L/R led us to investigate the correlation between the nanopore dimensions at the initial drilling and the structural stability of nanopores over time (see appendix A). The most relevant conclusion to the current line of experiments is that, in order to obtain stable nanopores with much smaller diameters, we needed to use thinner membranes to keep the L/R ratio as low as possible.

5.2.3 Conductance of the Smallest Single Nanopores

Once these new constraints in our fabrication protocol were better defined, we were able to achieve gas flow measurements in much smaller nanopores. To our knowledge, these are the smallest single nanopores characterized to date using direct gas transport measurement. Figure 5.7 shows the conductance of the sample shown earlier in figure 4.2F with a diameter ∼21 nm. An explicit demonstration of the stability of this pore is visible in the inset, and these measurements were taken at three and twelve days interval. The data was taken at 77 K using the same procedure as was described earlier. The first two datasets (red and blue dots of figure 5.7B) were obtained quickly as initial verification of the pore dimensions. These datasets were also limited to high Knudsen numbers in order to restrain the duration of the experimental runs. The last series of points (black dots) were taken more carefully and for applied pressures up to 56.8 bar. The data from this last set were measured over two consecutive days and a slight vertical shift is observed around Kn = 0.12; this is between the left-most points from the second day and the first day's data

extending to high Knudsen numbers.

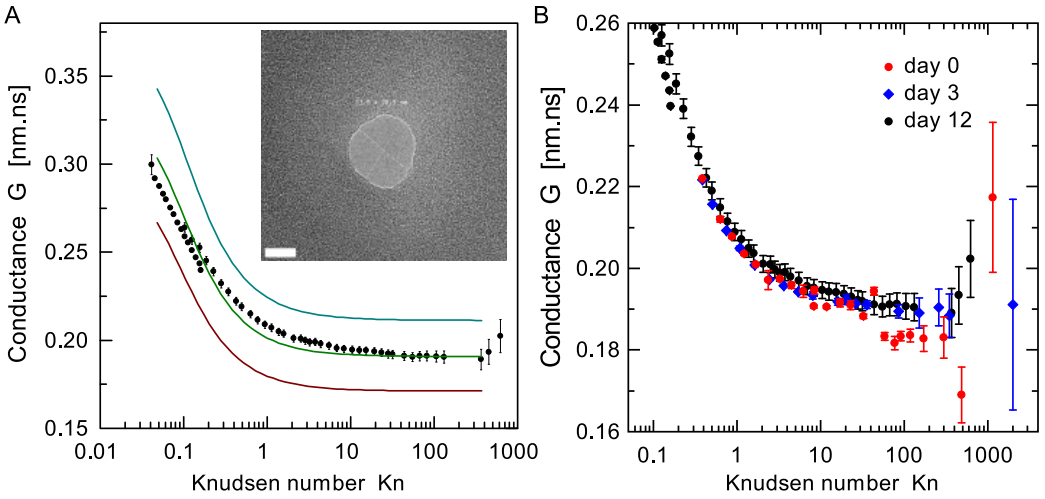

Fig. 5.7 Conductance, at 77 K, of a nanopore with a 21 nm diameter. The inset shows the TEM image of the pore. (B) Similar measurements were taken 12 days (red) and 9 days (blue) prior the conductance shown with black dots. The black dots are the same data for A and B. The stability over time is evident from the repeatability of the measurement. The white bar is 10 nm long and the TEM image is also shown in 4.2F.

The middle curve (green) in figure 5.7A is the total conductance function fit to the data and it is also reproduced with a radius 5 Å larger (teal curve) and smaller (crimson curve). Comparing to the effect predicted from a shift of a few Angström, the slight offset observed during the second day of measurements is not considered to be caused by a significant deformation of the nanopore. Figure 5.7B shows the measurements are repeatable.

The parameters of the fits shown in figure 5.7A are $\sigma = 18$ and $\alpha = 9.0$ for a radius of $R = 10.6$ nm and an opening angle of 7°. Comparing samples of different sizes, we find a general trend that these parameters increase as the nanopore samples decrease in size. However, a direct physical interpretation cannot be easily attributed to this observation because of the limiting phe-

nomenological nature of the model. Figures 5.7 and 5.8 both show deviations from the conductance equation over the transition region, however more samples need to be measured, over the full range of available pressures, before the applicability of the short-pipe flow model can be assessed in greater detail.

The smallest sample I was able to measure is shown in the inset of figure 5.8. The TEM image shows that the nanopore is slightly elongated and the length measured along the longest axis is 15.6 nm and 14.2 nm along the shortest. The wafer for this sample was 30 nm thick.

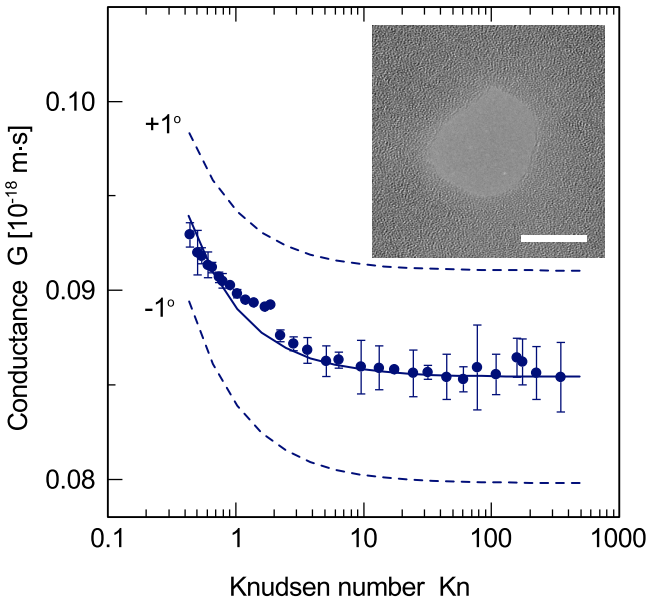

Fig. 5.8 Conductance of a nanopore 15 nm in diameter. The solid blue line is the total conductance equation fit to the data and the dotted lines on either side are computed from the same equation with angles $\pm 1°$. The inset shows the TEM image with a 10 nm long white bar for calibration.

The mass flow through this sample was measured from 9.0 mbar to 7.2 bar and in a liquid nitrogen bath at 77 K. The solid line overlaid on the data points is the total flow equation with $\alpha = 8.5$ and $\sigma = 7.0$ for radius of $R = 7.8$ nm

with an angle of 2.7°. The two dotted lines show the effect of varying the opening angle by 1°. These results confirm that a short-pipe Knudsen effusion model can quantitatively predict the conductance in single nanopores as small as ∼15 nm in diameter.

However, the feature seen around Kn = 1.5 could not be explained by a specific experimental event and its origin remains unexplained. I attempted to repeat the mass flow measurements using the same experimental conditions and the plateau feature was observed again at the same pressure, returning to the smooth curve towards higher Knudsen numbers. Unfortunately, this is not sufficient evidence to attribute a physical origin to this irregularity, since such a deviation was not observed in the course of measurements of other samples.

5.3 Conclusions from Gas Flow Measurements

We have measured the mass transport of helium gas through single nanopores fabricated in free-standing SiN membranes. The conductance of the nanopores was calculated from the observed flow for a wide range of pressures and temperatures. A clear transition was observed as the system transitioned from free-molecular effusion at low pressure to viscous laminar flow described by the hydrodynamics of continuous media. This transition was characterized in nanopores with diameters as small as 15 nm. The conductance in the Knudsen regime was found to be highly sensitive to changes in the dimensions of the nanopores as well as structural deformations of its walls. Prolonged monitoring of the conductance of a nanopore has been used to detect when the nanopore becomes structurally stable. Using our mass spectrometry measure-

ment scheme has also allowed us to successfully detect the mass transport in a single 15 nm diameter nanopore, which is the smallest nanopore to date where such a measurement has been achieved. Furthermore, the characterization of the flow in single nanopores establishes a foundation for the quantum fluid flow experiments presented in the next chapter.

Chapter 6

Hydrodynamics of Superfluid Helium in a Single Nanohole

This chapter presents the results we obtained by extending our measurement scheme to temperatures near the absolute zero. The measurement of mass flow was achieved in an experimental cell mounted inside a cryostat, as described in section 4.4. All mass flow measurements were performed with a Pfeiffer Smart Test mass spectrometer and the flow rate was calibrated before every experiment with an external calibrated leak with a constant leak rate of $4.5{\cdot}10^{-3} \pm 10\%$ ng/s.

The first sample in which superfluid flow was observed is shown in figure 4.2D. It had a nearly circular cross-section with dimensions of 42.7 and 45.6 nm along the shortest and longest axis, respectively. As with previous samples, the wafer was etched to leave a square free-standing silicon nitride window of $\sim$30 μm wide and has a thickness of 50 nm. This sample is very similar

to the one presented in figure 5.5B, albeit with a slightly smaller diameter. Using the Knudsen effusion in the gas phase, we verified that the sample dimensions remained the same throughout the experiments with superfluid. This first sample was measured in an experimental cell of the first generation (see section 4.3.1) and our results with this sample were published in *Physical Review Letters* [97].

The clean helium gas coming from the gas handling system was delivered into the cryostat where it passed through several thermal anchors with decremental temperature stages. Under normal operation, the temperature of these stages was set below the liquefaction point such that the liquid-gas boundary remains outside the experimental cell. The source side of the cell could therefore be kept full of liquid helium during the experiments. The sintered silver powder inside the thermal anchors offered the large surface area required for good thermal contact between the superfluid and the metallic surfaces of the enclosures. Details on the thermometry and temperature control have been given in chapter 4. The equilibrium time constant for the stabilization of each flow measurement in the cryostat increased to approximately 600 to 1200 seconds. This limited the number of points that could be obtained during each experimental run, but was sufficiently short for a careful measurement to be achieved.

6.1 Knudsen Effusion Below 20 Kelvin

The first gas flow measurement made on this sample were completed at room temperature on two separate days for low and high pressure ranges respec-

tively. The first day of measurement was performed over the range 30 to 790 mbar pressure, and the second day covered pressures up to 22.8 bar. Figure 6.1A shows the conductance of the sample at 295 K with the usual fit of the phenomenological model for the conductance in the transition region. Sister curves were also added for radii of ±1 nm. The parameters of this fit are $\alpha = 4.7$ and $\sigma = 11$ for a radius of 22.1 nm with an opening angle of 9°. The inset shows the TEM image taken during fabrication.

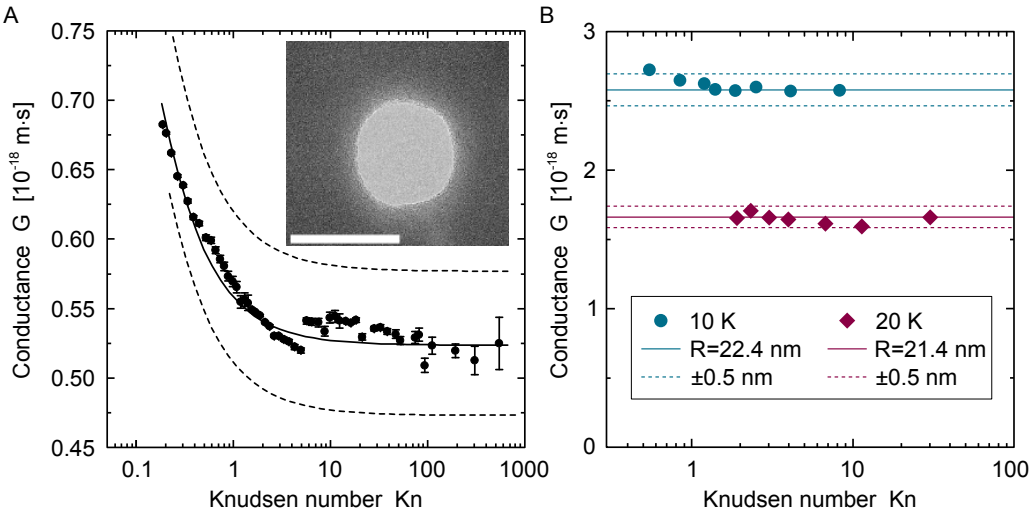

Fig. 6.1 (A) Conductance at room temperature of a single nanopore with a 45 nm diameter. The solid line is a fit of the total conductance equation with radius R = 22.1 nm. The two dotted lines represent the same function, but with radius larger and smaller by 1 nanometer. The white bar is 50 nm. (B) Similar conductance data taken at 20 K (teal dots) and 10 K (magenta diamonds). The lines over these datasets are from the Knudsen effusion conductance with R = 21.4 nm and R = 22.4 nm for 20 K and 10 K. In this case, the dotted lines are for a radius ± 0.5 nm.

Figure 6.1B shows conductance measurements at much lower temperatures, specifically at 10 K and 20 K. This data was obtained after all of the superfluid experiments were performed and demonstrates that the nanopore re-

mained structurally stable throughout the several months of operation. The fit of Knudsen effusion conductance to the data at low temperature give radii of R = 22.4±0.3 nm and R = 21.4±0.4 nm for the 10 K and 20 K data respectively. Additional dotted lines are shown for expected conductance using radii ±0.5 nm.

6.2 Liquid Helium Mass Transport

The typical procedure to determine the superfluid mass flow is as follows. First, both sides of the experimental cell are emptied at a temperature higher than the helium boiling point. Then, the apparatus is cooled below the superfluid transition such that the introduction of helium gas, via the gas handling system, forces condensation within the heat exchangers. This liquefaction is a slow process and only once all of the volume is filled with liquid helium does the data collection really begin. The helium atoms that pass through the nanopore are pumped out of the cryostat by the mass spectrometer, where they are detected. Keeping the applied pressure constant, the mass flow through the nanopore was monitored as the temperature was increased incrementally from 1.6 K to 2.5 K or more. Several such data sweeps are shown in figure 6.2.

6.2.1 Viscous Fluid Flow

In figure 6.2, the dotted line labeled T_λ is the bulk superfluid transition temperature. On the right-hand side of this line, there is no superfluidity expected to occur and only "normal" liquid helium should be present in the cell. In this portion of the graph, the data from each set show a clear increase in mass flow

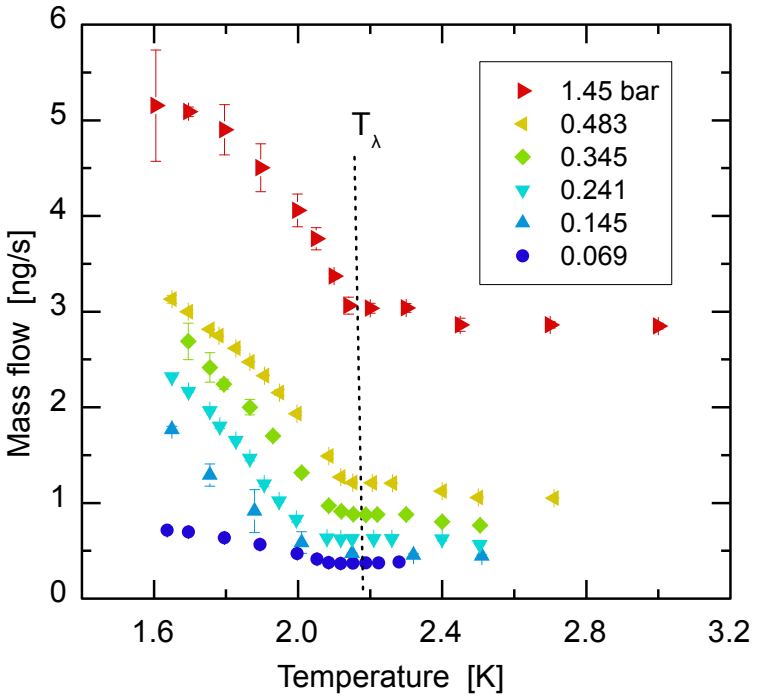

Fig. 6.2 Mass flow of liquid helium through a single 45 nm nanopore. Each symbol corresponds to a distinct temperature sweep at a fixed pressure of 0.069, 0.145, 0.241, 0.345 and 1.45 bar going from bottom to top. The dashed line shows the superfluid transition temperature for bulk helium (T_λ).

in response to an applied pressure gradient. This pressure-dependent mass transport demonstrates that the viscous fluid flow of liquid helium is not negligible, and it indicates the normal component of helium, below the superfluid transition, should also be taken into account. This is counter-intuitive and we initially had made the naive assumption that this would not be the case. Well known experiments showed decades ago that the normal component can be filtered-out in channels with dimensions of the order of 10^{-7} m, and the signals from the superfluid component could be measured exclusively. The conductance of the nanopore used in this experiment is however large enough

that the normal component remains a significant portion of the total flow. We believe the normal component was able to flow because of the relatively small length of the pore (L = 50 nm, D = 45 nm).

The theoretical framework used to treat the viscous component of the mass transport was developed in chapter 3. This model made use of the short-pipe viscous equation (Eq. 3.10) to determine the liquid helium flow through a nanopore. This equation was used to fit the data at temperatures above T_λ. The average of the radii found from fitting each dataset of figure 6.2 was $\overline{R} = 20 \pm 2$ nm, and an example of this fit is shown in figure 6.3 for clarity. This average radius is in excellent agreement with the gas flow measurements and the TEM imaging. The viscosity and density of liquid helium were taken from the literature [61, 98, 99], and the length of the pore taken as the membrane thickness of 50 nm. The α parameter for the end effects in the nanopore was set to $\alpha = 4.7$ as found in our earlier experiments with gas flows (see figure 6.1). The modeling of the viscous flow was then used to determine the superfluid component, as will be described below.

6.2.2 Superfluid Flow Through the 45 nm Nanopore

The data of figure 6.2 shows a clear increase of the mass flow when the temperature decreases below the superfluid transition, and this is observed for all pressures investigated. To better illustrate this increase, we focus our attention on a single temperature sweep shown in figure 6.2. Taking the curve for 483 mbar and reproducing it in figure 6.3, we easily notice the different flow regimes on either side of T_λ. Here, the temperature axis was offset for clar-

ity in an attempt to alleviate the small shift in the superflow onset observed in some of the data sets. We suspect that the temperature recorded by the thermometer during the lower pressure experimental runs could have suffered from a small gradient in the temperature across the experimental cell, which in turn could have offsetted the temperature scale. The largest offset we recorded was 84 mK for the 241 mbar series and, for the other datasets, an average of 32 mK shift. This correction to absolute temperature was applied before any subsequent modeling and determination of the superfluid component.

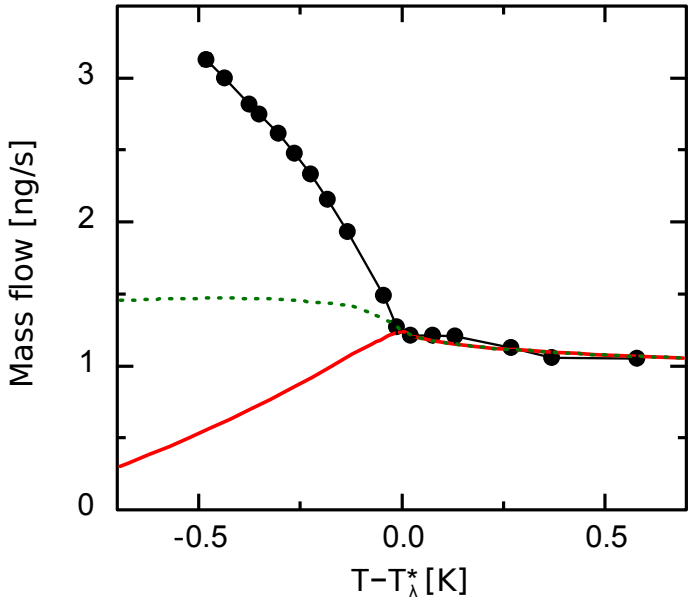

Fig. 6.3 Mass flow measured at a constant pressure of 483 mbar. The connecting line is a guide to the eye. The green dotted line is the flow computed by the short-pipe equation of viscous flow, using the total helium density ρ over the whole temperature range. This assumption effectively treats both He I and He II as classical fluids. The red solid line is built from the same equation, but using the density of the normal component only. The temperature axis is defined with respect to the superfluid transition temperature (T_λ).

Total Flow

The equation for the two-fluid flux (equation 3.12) can be used to understand the flow in the single nanopore. Assuming an average velocity in the pore, we consider the total mass flow given by $Q_m^{total} = J_{total}\pi R^2$ and the normal component of He II described by a viscous short-pipe flow, as discussed before (Eq. 3.10). The total mass flow is therefore given by

$$Q_m^{total} = \pi R^2 \rho_s v_s + \frac{8\pi\eta L}{\alpha}\left(\sqrt{1+\frac{\alpha\rho_n R^4}{32\eta^2 L^2}\Delta P}-1\right), \tag{6.1}$$

and it can be compared to the mass flow measured experimentally. The only unknown remaining in this equation is the superfluid velocity v_s, which is expected to be limited only by an upper-bound critical velocity.

In an effort to describe the observed mass flow through the 45 nm nanopore, the right-hand side term of equation 6.1 was fit to each data series shown in figure 6.2. Again focusing on the data in figure 6.3, we produced two curves using the viscous short-pipe flow model (Eq. 3.10). The dotted green line was computed using the total helium density for the whole temperature range, thus working under a "no superfluid" assumption. Above T_λ this model agrees well with the data, as expected for a purely "classical" viscous fluid. Below T_λ, the observed flow is approximately twice as much as that which a simple fluid would produce. We attribute this excess to a superfluid contribution to the total flow. In contrast, the solid red line was computed using the tabulated density from the normal component of the two-fluid model. This normal density is similar to the values shown in figure 3.4 for bulk helium at saturated vapor pressure. In effect, this red curve is the second term of

equation 6.1.

The superfluid flow was then extracted by subtracting the normal component from the total flow. As mentioned in chapter 3, superfluid flow takes place at a critical velocity beyond which it cannot cross because of the onset of energy dissipation. The critical velocity in other flow experiments is usually reached at pressure heads of ∼O(1) Pa and so we therefore assumed that the large pressure differential used in our experiments were sufficient for the superfluid to reach the critical velocity. From the superfluid mass flow, we can isolate the effective velocity of the superfluid at each point since the cross sectional area and density are known. This velocity is interpreted as the superfluid critical velocity and is discussed further in the following section.

6.2.3 Critical Velocity in a Nanopore

The critical velocity data inferred from the total mass flow is shown in figure 6.4. We note a clear dependence on the temperature and a nearly linear regime for the points at lowest temperature. In figure 6.4, the critical velocities were normalized with v_{c0}, the extrapolated critical velocity at T = 0 K. This extrapolation is accomplished using a linear fit of the critical velocity data. The normalization makes it easier to compare to data from Zimmermann *et al.* [100, 101]. In their work, they found that the dependence on temperature of the critical velocity of superfluid in small channels follows a linear function of the form $v_c(T) = v_{c0}(1 - T/T_0)$ (see also the discussion of equation 3.14). In their experiments, v_{c0} was found to be of the order of 1 to 25 m/s [70, 100]. For the single nanopore flows shown in figure 6.2, this extrapolation to T= 0 K

gives values of v_{c0} between 8 and 45 m/s. It is worth mentioning that our experiments are for continuous flow, whereas most results from other groups are obtained with an oscillating membrane inducing an "AC" flow of very small amplitude. This qualitative difference is especially important with respect to the temporal resolution of the measurements; we observe long time averages of the signal, whereas they can detect milliseconds dynamics of the flow.

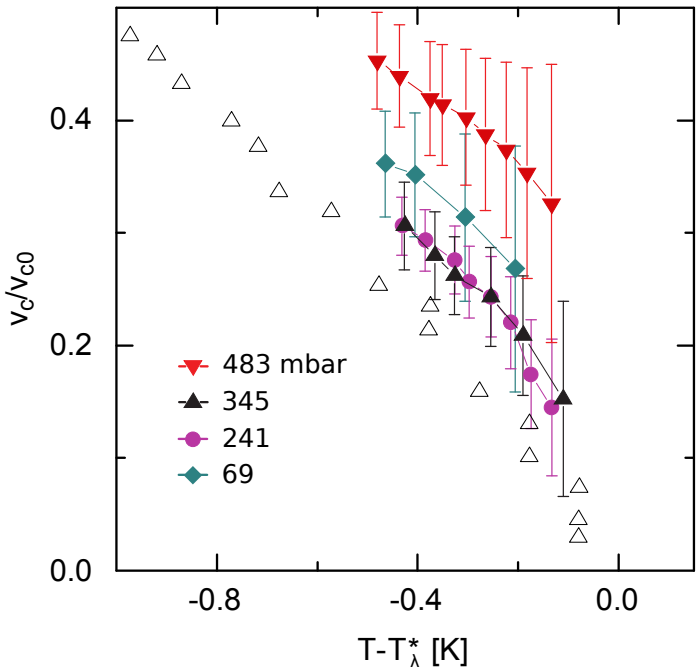

Fig. 6.4 Critical velocity of the 45 nm nanopore as a function of temperature. Each different symbol corresponds to the data of figure 6.2 and the connecting lines are guides-to-the-eye. Each dataset is normalized with v_{c0}, the critical velocity extrapolated to T= 0 K (see text). This was done in order to compare to data from [100, 101] (open triangles). The error bars are defined by the propagated uncertainty of the density, viscosity, flow and cross sectional area of the pore.

The error in the critical velocity is largest near T_λ because of the uncer-

tainty of the superfluid density. This large error prevents us from resolving the behavior of the critical velocity in the vicinity of the superfluid transition. We however clearly observe that the temperature dependence of the superfluid critical velocity shows similar behavior to what was found in larger channels by other experimental techniques. To our knowledge, the absolute value of the critical velocity inferred from our mass flow measurements is the largest ever measured in channel flow experiments.

6.3 Liquid Helium Mass Transport in 16 nm Nanopore

Based on the results obtained in the 45 nm sample of the previous section, we attempted to reproduce these measurements in smaller nanopores in order to map out the behavior of liquid helium as it approaches the 1D limit. The smallest sample that yielded a superfluid signal at low temperature is shown in figure 6.5. The picture in the left panel (A) was taken after the sample fabrication, which took place six months before the superfluid measurements were conducted. The picture on the right panel of figure 6.5 (B) was taken four months after the measurements, in order to demonstrate the long term structural stability of the sample. The TEM images show a decrease of the diameter from 17.3 ± 0.8 nm to 15.6 ± 0.7 nm; this nearly identical dimension is characteristic of a nanopore that has reached a fully stable configuration. The membrane in which this sample was drilled was 30 nm thick and with the usual free-standing surface of $\sim$30 μm by $\sim$30 μm.

The low temperature measurements with this sample were achieved in an experimental cell of the second generation, and additional precautions were

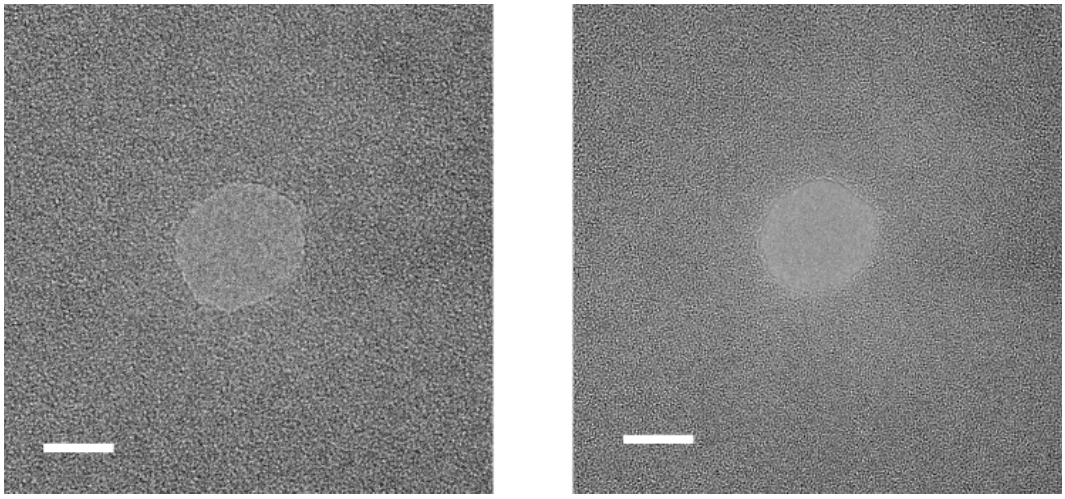

Fig. 6.5 (A)Image taken six months before the measurements of superfluid flow in this nanopore and (B) the TEM image of the same sample taken four months after the measurements. The white bar is 10 nm long.

taken to ensure ideal thermal anchoring and temperature monitoring. The experimental procedures for the superfluid measurements of this sample were replicated as closely as possible to what was described previously. The empty cell was kept below liquefaction temperature and filled slowly with helium gas until the condensation within all cold volumes was completed and an equilibrium was reached. At that point, the pressure applied above the membrane can easily be kept constant. Setting this pressure at a desired value, the temperature was then increased in a stepwise fashion in order to provide sufficient time for the mass flow signal to equilibrate at each step. While the experimental protocol was similar, the modifications to the apparatus caused a drastic increase in the typical time required for the signal to equilibrate. A single measurement of the flow was now on the order of 6000 seconds. As was the case with the larger 45 nm sample, a Knudsen effusion measurement was also

performed in order to confirm the nanopore dimensions *in situ*.

6.3.1 Knudsen Effusion Measurement to Confirm Nanopore Radius

Gas effusion measurements were taken with the experimental cell at a constant temperature of 20 K. Because of several changes to the apparatus implemented prior to our measurements with this sample, it was necessary to test whether the warm, low-density gas from the gas handling system was properly thermalizing in the newly installed thermal anchors. In effect, helium at room temperature was cooled to ∼4 K while passing through the anchors, then warmed back to 20 K immediately before entering the experimental cell. Specifically, the thermal anchor on the 1 K pot were first kept at $T < T_{boiling}$ (3.8 K) while the gas pressure was varied to take the Knudsen effusion data. In a second run, the thermal anchor was then kept at $T > T_{boiling}$ (∼5 K), thus preventing condensation of the helium gas. Two datasets of effusion at 20 K were thus taken, at a two-days interval, to test whether the gas was properly cooled before reaching the experimental cell.

The results of the two runs are shown in figure 6.6. These results are effectively identical and, qualitatively, the flow exhibits no difference between the two attempts. This indicates that the gas is indeed thermalized appropriately by the last thermal anchor and the temperature of previous components of the cryostat does not affect the measurement further down. The flow detected was also quantitatively consistent with the Knudsen effusion theory for flow in a single 16 nm nanopore, as is evident from the lines in figure 6.6. Because of operational constraints in the laboratory, these gas flow measurements could

not be achieved at 77 K, as was usually done with other samples. Nonetheless, a useful comparison can be done with the effusion data of the other 16 nm sample in the previous chapter (figure 5.8). By scaling-down the 20 K flow with the square-root dependence on temperature of Knudsen effusion, we confirm the two samples yield comparable conductances. This simple comparison quickly confirms our measurements are consistent between the two nanopores with a radius ∼16 nm.

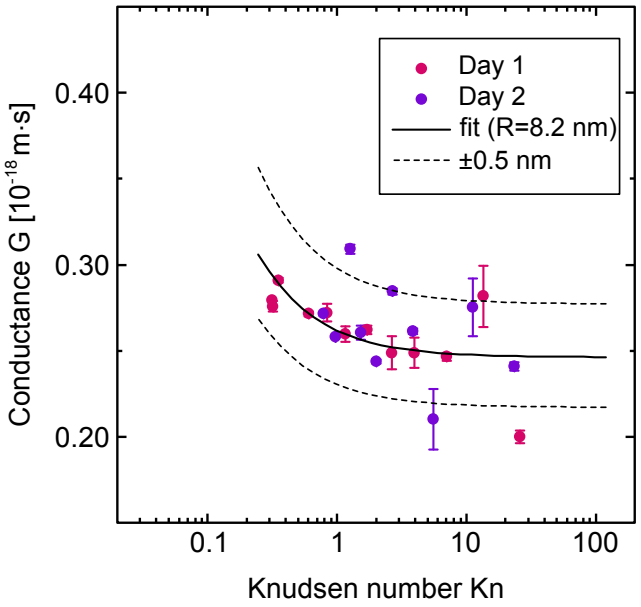

Fig. 6.6 Gas conductance at 20 K of a 16 nm diameter nanopore. The two data series are for identical experiments realized two days apart. The solid line is a fit to the data for the total conductance with a radius of 8.2(1) nm, $\alpha = 4.7(1)$ and an opening angle of 8°. The dashed lines are from the same equation computed with a radius set at 7.7 nm and 8.7 nm.

The solid line overlaid on the conductance data at 20 K is the equation 5.4 with radius of $R = 8.2 \pm 0.5$ nm and an 8° opening angle was included in the determination of the Clausing factor. The two dashed lines on either side of

the fit are computed using the same equation with radius larger or smaller by 0.5 nm. The confirmation of the radius from the conductance in the Knudsen effusion regime gives us confidence the experiments in the superfluid phase can be carried out, and that the sample dimensions can remain stable over time.

6.3.2 Superfluid Mass Flow in a 16 nm Nanopore

Measurements of liquid helium flow through the 16 nm sample are shown in figure 6.7, where each set of colored symbols represents a constant-pressure series of measurements. The solid lines between similar symbols are guides-to-the-eye. Starting near $T \simeq 1.55$ K, the cell was warmed incrementally with a given pressure head of 68.9, 145, 276, 345, 483 or 689 mbar. Sufficient time was allowed for the mass flow signal to reach its asymptotic equilibrium, as explained earlier in section 5.1.1. The signal from the mass spectrometer was calibrated with the same external calibrated leak of $4.5 \cdot 10^{-3}$ ng/s and the sample was kept below T = 5 K during all liquid helium experiments.

In figure 6.7 the error bars show the uncertainty associated with the precision of the mass flow signal, and are typically smaller than the symbol size. This is however not the largest source of uncertainty, as can be seen from the 689 mbar dataset. The few green triangles symbols not connected by the solid line were taken on a separate day and show a slight offset that we attribute to the uncertainty on the accuracy of the measurement set up. While this systematic error remains small relative to the overall flow, it is larger than other errors in several of the datasets. In order to keep the figure clear and be able to observe the trend of mass flow across T_λ, the error bars used did not

include this hard-to-estimate systematic uncertainty.

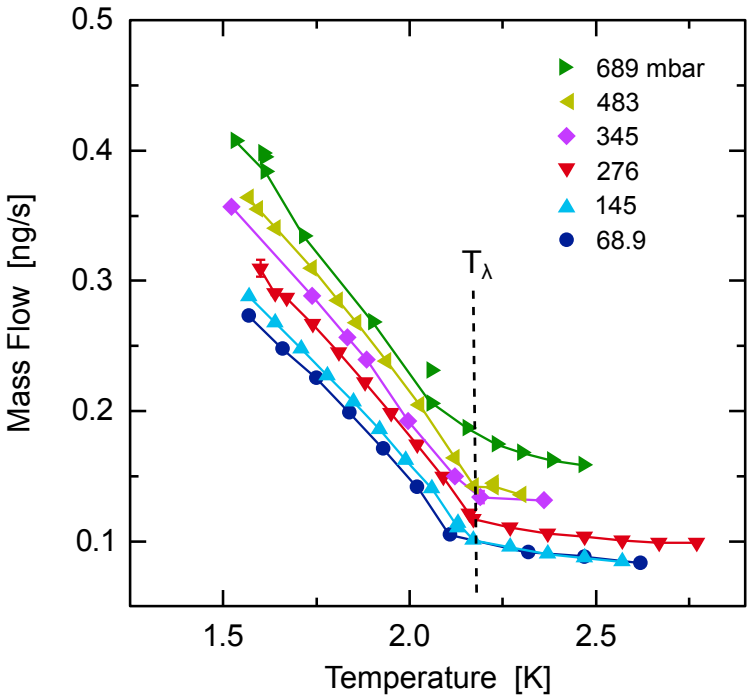

Fig. 6.7 Superfluid mass flow through a 16 nm sample. The dashed line is the superfluid transition temperature T_λ. The solid lines are guides-to-the-eyes.

A sharp change in flow regime is observed in the mass transport data at the T_λ line (dashed line). The flow transitions from a nearly constant value to a steadily increasing one when the temperature is lowered across T_λ. At the lowest temperatures we reached, the flow is nearly three times larger than at $T = T_\lambda$.

An important observation to make regarding these data series is that the small discrepancy between the expected superfluid transition temperature and the observed one is absent. This suggests that the small shifts observed with the previous sample (section 6.2) were likely thermometry artifacts and the

improvements to the apparatus, between the first and second generation of experimental cells, provided the required thermal contact between the liquid and the thermometry equipment.

The fitting procedure described earlier for the 45 nm sample has been duplicated on these datasets. The viscous helium contribution to the total flow was computed using the mass flow predicted from this equation, with the density and viscosity interpolated from isobaric curves [61, 98, 99]. As an example, the 483 mbar dataset was selected to show the result of the fit, as seen in figure 6.8. The radius found from this fit was 8.3 nm, which is within the 16 ± 1 nm diameter measured from TEM imaging. The α parameter used was 4.7, which was obtained from the gas conductance measurements shown in the previous section; this is also the value used for the larger 45 nm nanopore.

The fit of the short-pipe viscous flow model (Eq. 3.10) to the $T > T_\lambda$ data of the other datasets was also achieved. The radius found this way had a larger variance than expected, compared to the similar fits done with the 45 nm sample in the previous section. To be specific, for smaller pressures datasets, the fitted radius was too large, and in the worst case, for the 69 mbar dataset, the fit yielded a radius of 12 nm. This is well over the confidence interval of our TEM diameter measurement. Given that the equation used in the fit yielded worst results at low pressures, we examined the flow behavior as $P \to 0$. In order to directly investigate this discrepancy, we measured the flow as a function of the applied pressure for a fixed temperature of 2.25 K, well within the He II region. The data we obtained is shown with black dots in figure 6.9.

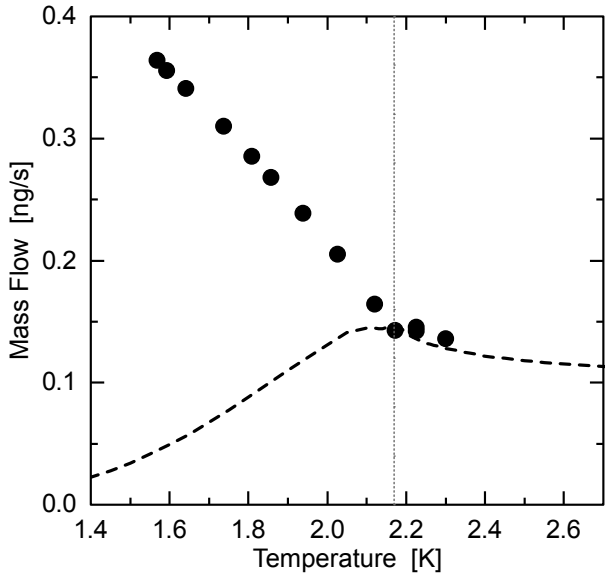

Fig. 6.8 Superfluid mass flow at 483 mbar in the 16 nm sample. Shown as a dashed line is the contribution from the normal component of liquid helium computed from the viscous short-pipe equation. The difference between the measured flow and the predicted flow is assigned to the superfluid component.

The first observation one can make looking at these data is that the flow appears to have a finite value as the pressure approaches zero. This is not the behavior our model predicts and explains why the fit yielded much larger radii for the lowest pressures. The red curve shows the viscous flow model of equation 3.10 with a radius of 8.1 nm. The distribution of the data over this curve is imbalanced, which indicates the equation might not describe the data as accurately as possible. The simplest hypothesis one can make to explain this discrepancy is to add a constant offset to the equation, which could account for the "supplemental" flow observed. This offset would imply that a secondary, parallel transport mechanism might be contributing to viscous flow. We fit this modified model to the data, and the black curves in figure 6.9 show the

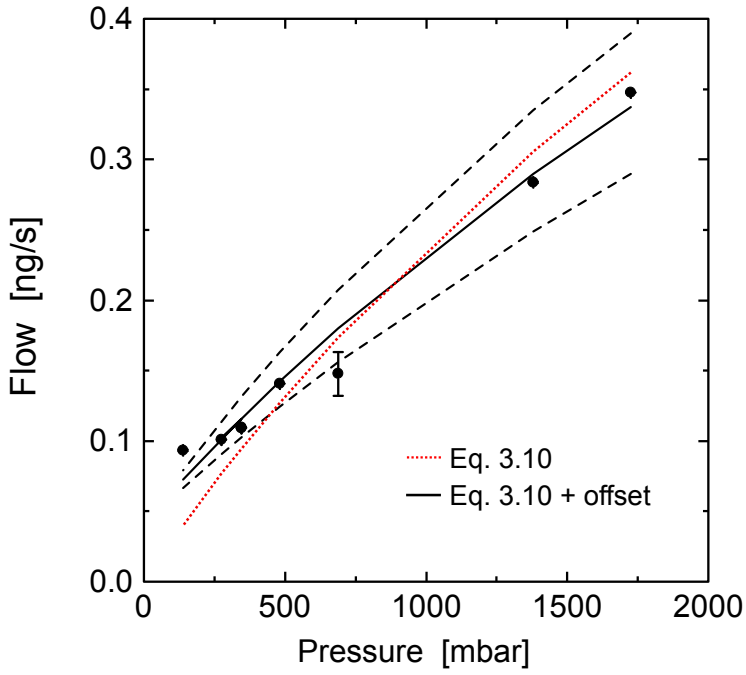

Fig. 6.9 Liquid mass flow through a 16 nm sample as a function of the applied pressure. The dots are the measured flow and the open circles show the former values with a constant subtracted to respect Q(P=0)=0. The solid line is a fit to the data with a radius of 7.7±0.4 nm.

result. The fitted radius was 7.7±0.4 nm, and the solid line shows the curve with R = 7.7 nm, whereas the dashed lines on either side were computed with R±0.4 nm. While it is interesting to note that a small offset can improve the fit to the data, we do not have sufficient information to conclude on the validity of this correction. This new radius fitted to the data remains consistent with the dimensions measured by microscopy.

In summary, the viscous helium flow $Q^{viscous}_{short-pipe}$ can be modeled with the short-pipe viscous equation. Here again, we attribute the difference between the observed flow and the flow predicted by this equation to a superfluid con-

tribution. As was done for the 45 nm nanopore, earlier in this chapter, the effective superfluid velocity was inferred from this superfluid mass flow. The superfluid contribution was extracted from the data in figure 6.7, and the velocities inferred from them are shown in figure 6.10. The first panel (A) shows the absolute velocities and the panel on the right (B) shows the results of the 483 mbar dataset normalized to the extrapolated T = 0 value v_{c0}. This normalization was performed to facilitate the comparison to data of [100] shown as open triangles. In the determination of a critical velocity, we again make the implicit assumption that the superfluid motion is limited by the emergence of energy dissipation mechanisms.

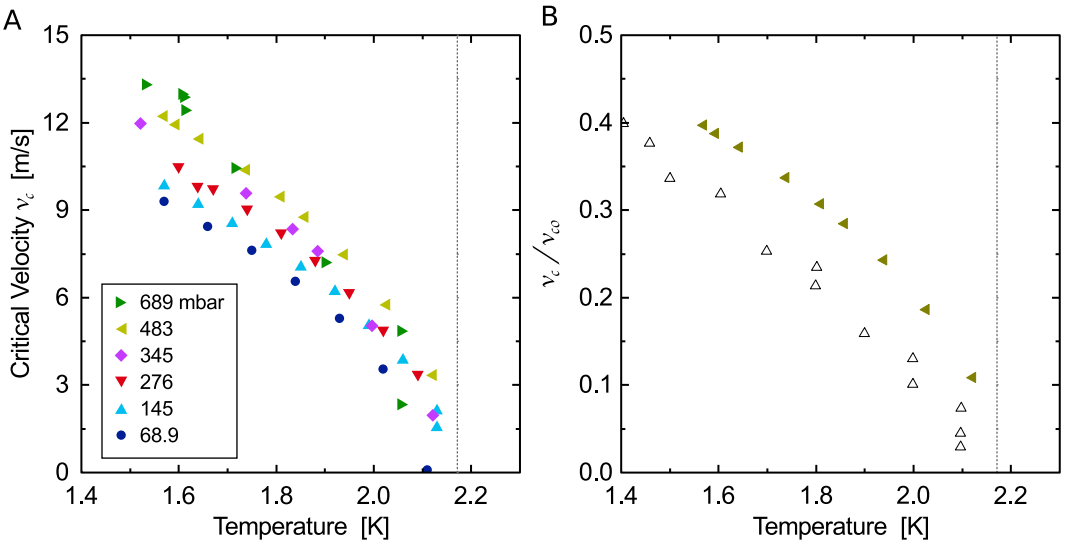

Fig. 6.10 Critical velocity of the superfluid component in the liquid helium transport through the 16 nm pore. The symbols are the same as in figure 6.7 and each corresponds to a given pressure head. The vertical dotted line is positioned at T = 2.17 K to show the superfluid transition temperature. (B) Critical velocity of the data at 483 mbar and normalized to the extrapolated velocity at T = 0 K. Open triangles are data reproduced from Zimmermann *et al.*[100].

These results are qualitatively similar to those found for the 45 nm sample. Qualitatively, the superfluid contribution continues to exhibit a linear dependence on temperature down to the lowest temperatures accessible with the modified apparatus. Specifically, the critical velocity of the superfluid in the 16 nm nanopore reaches this nearly linear regime below approximately 1.9 K. The behavior of v_c is is easily compared to the data of [100], (see figure 6.10B), where both datasets demonstrates a behavior consistent with each other. Quantitatively, the extrapolated critical velocity at zero temperature were found to extend from 27±1 to 39.5±1.6 m/s for the 68.9 to 689 mbar datasets respectively. Once again, in absolute values, these are larger than the ones measured in micropores.

6.4 Critical Velocities of Superfluids in Single Nanopores

The critical velocity inferred from the total flow of liquid helium in the two samples shown in this chapter can easily be compared to other experiments of superfluid flow. Figure 6.11 contains a compilation [64] of critical velocities found over several decades and in a multitude of experiments (open symbols). The red bars show the range of superfluid critical velocities found in our study (values at T = 1.7 K for each data set). Our results are positioned in channel sizes never before accessible and are the highest superfluid critical velocity observed yet in channel transport experiments. In other words, our experimental method has allowed us to determine the critical velocity of superfluid helium in the smallest channels yet.

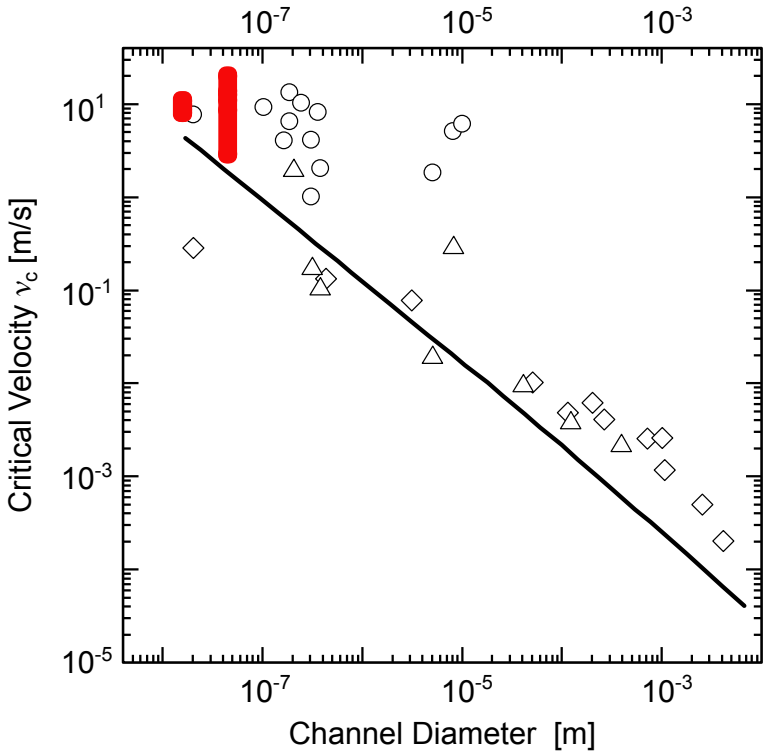

Fig. 6.11 Consolidated graph of critical velocities found by several groups over many years. The open circles are identified as intrinsic critical velocities, whereas the other symbols have the channel size dependent critical velocity closer in behavior to the Feynman model of quantized vortices (solid line). The red bars show the span of critical velocities obtained with the two samples presented in this chapter.

The open circle symbols are results of experiments where the superfluid critical velocity was found to be size-independent and linearly dependent on temperature. This class of critical velocities is quantitatively much larger than the second type observed, diamonds (for older data) and triangles, those being for critical velocities dependent on the dimensions of the flow channel. The two types of critical velocities are referenced to as internal or external, in reference to their dependence on the *internal* temperature or *external* pore geometry.

The physical phenomena driving the dissipation of energy is qualitatively different in both cases. For example, internal critical velocities have only been observed in smaller pores where the temperature dependence suggested a thermally activated process. This has been described as a stochastic nucleation of phase slip events removing quantized circulation units [64]. In larger channels, it is more frequent to encounter systems exhibiting external superfluid critical velocities that have an inverse dependence on the channel dimension. These follow, albeit loosely, the prediction of the Feynman model (solid line in figure 6.11) where a continuous shedding of energy is possible through vortices positioned across the (micro)pores.

The linear dependence on temperature and the large critical velocities found in our work are both consistent with a critical velocity of the internal type. Its qualitative behavior is also very similar to the extensive data of Zimmermann *et al.* [100]. The functional dependence of the critical velocity closer to zero temperature was not accessible in this work; the values reported on figure 6.11 would be even higher if the extrapolated critical velocities at lower temperatures were taken as an estimate. Access to data closer to T = 0 would have also allowed us to characterize the plateauing of v_c below T $\simeq$ 150 mK, indicating perhaps the transition from a thermally activated process to a quantum tunneling activation of the phase slip events [102, 103].

6.5 Summary

In summary, we have shown that measurements of liquid helium mass transport in single nanopores can be interpreted with a two-fluid model containing a

short-pipe viscous flow formalism. The extensive characterization of mass flow in our nanopores can account for the non-negligible contribution of the normal component of He-II. This has allowed us to infer the superfluid contribution to the total flow, as well as its critical velocity. The latter was found to be the largest ever observed in experiments of superfluid transport in channels.

Chapter 7

Conclusion

7.1 Summary

In this work, I have developed a novel measurement scheme for the characterization of mass flow in single nanopores. The sensitive detection of the mass flow was made possible by employing a mass spectrometer to count the atoms passing through a very thin silicon nitride membrane in which a single nanopore was drilled. The choice of a solid-state membrane was made to leverage technical innovations in the use of transmission electron microscopes that allow for the controlled ablation of material with their high-intensity electron beam. This technique makes it possible to fabricate nanopores of any desired dimension through thin solid-state membranes.

By designing a transport experiment where two reservoirs are separated by the wafer containing the thin membrane, very accurate measurements of mass transport between the two reservoirs were made possible. Several experimental cell designs were implemented in order to optimize the yield of the measure-

ment scheme and ensure that the wafer could remain completely sealed over a broad range of temperatures and pressure. I have found that the most efficient technique of sealing the wafers to the metal body of the experimental cell was to use small indium o-rings. This method was proven effective even after several thermal cycles between room temperature and typical cryostat temperatures.

The controlled introduction of helium in the source reservoir of the experimental cell allowed us to control the pressure gradient across the nanopore. The drain side of the experimental cell was continuously pumped such that any helium passing through a nanopore could be detected by the mass spectrometer. The combination of vacuum below and positive pressure above the membrane induced mass transport determined by the conductance of the nanopore. By measuring the mass flow and calculating that conductance under different thermodynamic conditions, the physics of confined fluids was studied.

The first experiments performed were designed to test whether the mass flow could be quantitatively understood. A large pore of $\sim$100 nm in diameter was exposed to a large range of pressure differentials and the conductance of the pore was monitored under these conditions. The conductance at low pressures was found to be very accurately modeled by Knudsen effusion in a short-pipe. A fit to the conductance data in this flow regime yielded an effective flow area with radius within 1% of the dimensions found using a TEM image. The agreement between the electronic imaging and the mass flow determination of the radius was sufficiently accurate to confirm the validity of the measurement scheme.

We further investigated the conductance of this sample at higher densities where the flow characteristics were expected to be understood with the theory of viscous transport in continuous media. From the conductance data over the whole transition region, we were able to develop a phenomenological model tailored for short-pipe channels where the effects of the geometry of solid-state nanopores could not be neglected. We then extended our investigation to pores well within the nanoscopic range. We presented results of direct measurement of the gas transport in the nanopores as small as 15 nm. This is to our knowledge the smallest dimension where such measurements were performed. These experiments demonstrated the need to correct the Clausing factor to account for the larger transmission probability caused by the tapered opening of the nanopores. The very accurate monitoring of the nanopore dimensions also allowed us to discover a slow structural deformation of the nanopores. Some of the results from this tangential line of investigation are presented in the appendix of this thesis.

Building on the results obtained with gas flow in single nanopores, we designed a second experimental cell such that measurements could be realized inside a ^{3}He cryostat, at low temperature. Our results indicate that the liquid helium flow through a nanopore is detectable with this technique. Furthermore, and as expected, we observed the mass transport below $T_\lambda \approx 2.17$ K to be much larger than in the viscous, normal flow of helium fluid. Using a two fluid model of He II, we interpreted the additional mass flow as originating from a superfluid component flowing with negligible viscosity. The effective flow of superfluid through the nanopore provided an average velocity that we

collected at several temperatures between ∼1.55 K and T_λ, for both a 45 nm and 15 nm diameter samples. These velocities were assumed to correspond to the critical velocity, *i.e.* the velocity defined by the onset of dissipation mechanisms inside the superfluid. Our results do show a clear linear dependence on temperature, and no significant difference between the two samples was consistently observed. These inferred critical velocities are the largest recorded to date in channel experiments. Our experiments of superflow in single channels have also extended the range of pore sizes available by nearly an order of magnitude.

7.2 Future Work: Towards the Luttinger Regime

The experimental scheme developed in this work has been shown to be very accurate for the determination of mass flow in nanopores as small as ∼15 nm. In fact, a scaling of the signal-to-noise ratio with current flow level indicates the technique can be extended to nanopores with a diameter as small as 1 nm. A quantitative determination of mass flow in the nanoscopic range offers opportunities for other fields of study. For example, experiments with biomolecules such as DNA translocated through nanopores [104] are very sensitive to the dimensions of the pores. In the transition from the microscopic world to the nanoscopic one, some groups have observed anomalous transport [105, 106, 107, 108] and surprising effects [109] suggesting that the physical hypothesis at the pore boundary conditions might need to be carefully considered.

Our ability to detect the signal from a single nanopore and the high precision offered by TEM drilling, are features of great interest for experiments

aimed at investigating corrections to hydrodynamics models. Currently, such experiments are realized in carbon nanotubes and recent, surprising results [110] will benefit from the availability of tailored channels like those presented in this thesis.

Apart from the impact to classical fluid transport studies, pushing the limit towards even smaller nanopores is greatly relevant for the ultimate goal of implementing the long sought-after Tomonaga-Luttinger liquid with neutral particles. With this in mind, future work will aim at mapping the characteristics of helium mass flow in nanopores of various sizes, all the way down to 1 nm. Preliminary results from our group with nanopores as small as 6 nm show how this work helps to bridge the gap towards the 1D limit; these pores are within a factor of $\sim$2 of the dimensions required to observe Luttinger liquid behavior, according to the quantum Monte Carlo simulations. In parallel to this objective, the low temperature experiments can in principle be reproduced using ^{3}He, either as a pure fermionic fluid or as a diluted medium (a ^{4}He-^{3}He mixture). These mixture offer interesting opportunities [111] that could be directly supplemented by our ability to work with nanometric apertures and could, in principle, demonstrate the quenching of quantum statistics in one-dimension.

Appendix A

Appendix: Nanopore Shrinking

A.1 Blockages of Nanopores

As we endeavored to reproduce our experiments within smaller nanopores, we regularly suffered blockage issues. Fabrication with the transmission electron microscope (TEM) allows for an image to be taken within a few minutes of the nanopore drilling. This helps to validate the dimensions of samples before making mass transport experiments with them. On several occasions however, the measurement of the mass flow through some samples would produce no signal, except for an unwanted diffusion through epoxy with the earlier designs of the experimental cell. Several attempts at thermal cycling theses blocked samples or applying very large pressure gradients across the pores have never been successful at re-opening those blocked pores. New images of these samples with the TEM would subsequently confirm their blocked state.

A.1.1 Two Types of Nanopore Blockages

It is interesting to note that blocked pores can be easily detected with the TEM imaging. This is in part because the silicon nitride membranes are manufactured very flat and small variations of thickness produce a different intensity of the electrons transmitted, which we observe as a varying saturation of the pixels in the image. Indeed, the ablation of material from the membrane in the area right around the nanopore makes the image appear lighter, and the area further away from the pore becomes darker because of an unavoidable accumulation of trapped charges on the surface of the membrane following the exposure to high fluxes of electrons. When we observe a blocked nanopore under the microscope, the position of the nanopores remains easily detectable because of these specific patterns in pixel saturation. This variation in the intensity of the image is easily observable by a trained eye and allows rapid localization of the nanopore, even when the whole surface of the wafer is coated with contaminants. Figure A.1 shows an example of a membrane coated with a film of contaminants and in panel B, a close-up of the blocked nanopore. As can be easily seen on this picture, contaminants cause a reduction of the intensity of transmitted electrons. The dark spots on this picture are droplets of a foreign substance.

Two distinct cases occurred when we imaged blocked nanopores. The first case was typically observed in conjunction with the presence of hundreds of droplets on the membrane surface (figure A.1A), usually several hundred nanometers wide, and easily noticeable because of their peculiar reaction under irradiation with the intense electron beam. Indeed, these droplets were

visibly affected by the exposure to the energetic electrons, in contrast to the immutability of solid substrates like the SiN and Si. A strong carbon signal was observed when we performed an EDX analysis centered on nanopores with this type of blockage, which led us to suspect a contamination from organic molecules. These membranes could not be re-drilled because the contaminants would typically flow back into the freshly drilled aperture, thus blocking the nanopore instantaneously.

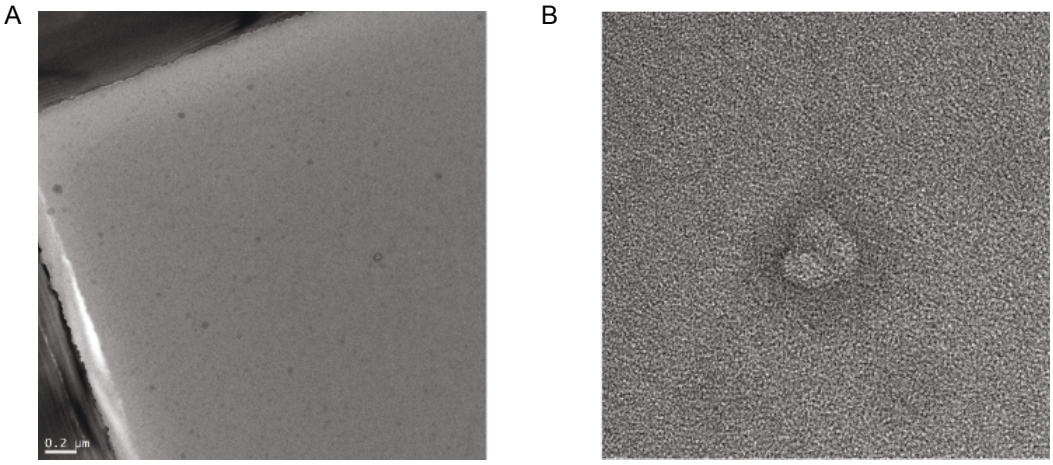

Fig. A.1 (A) Transmission electron microscope image of a free-standing membrane with droplets of contaminants. (B) Close-up of the nanopore coated with a thin film of contaminants. The irregular diffraction pattern over the whole surface of the image indicates the nanopore is not open.

The second type of blockage was characterized by a very different appearance of the SiN membrane. The TEM image would be almost identical to a freshly drilled nanopore except that, instead of a uniform pixel saturation, the area where the nanopore used to be would now display the typical diffraction pattern of amorphous materials. This led us to conclude that a thin layer of amorphous material blocked the aperture while the rest of the surface re-

mained unchanged. In order to compare to the first type of blockage, we again performed analysis of the element composition in and around the nanopore, and no organic compounds were detected, whereas large silicon and nitrogen signatures dominated the signal as expected.

Contamination Prevention

The presence of organic material on the surface of the membrane was an issue that we tackled by first designing filters and traps such that any gas sent to the experimental cell from the gas handling system (GHS) would be filtered. These filters were described earlier in chapter 4, and one such filter was positioned at every entry point of the GHS. The GHS was then flushed[1] several times, until a final filling was done with ultra-high-purity (99.999%) helium gas. This clean gas was then kept in the GHS and all operations were subsequently completed in a closed-cycle manner by using the pumping capacity of the dipstick.

The discovery of the contamination of samples also led to a new experimental cell design where no epoxies were needed and all joints were exclusively made with compressed metal rings. I found the most effective design for the experimental cell had all joints made with a compressed indium wire. These additional precautions and experimental features led to the resolution of the contamination issues.

[1] A process where a volume is emptied and partially refilled in order to remove foreign particles. This process is usually repeated several times.

A.2 Partial Nanopore Shrinking

As was noted earlier in chapter 5, we noticed that on occasions, the conductance of the nanopores studied would decrease between two similar measurements taken on two different days. In fact, the modeling of the conductance in the Knudsen regime allowed us to detect a significant decrease in the size of the nanopore over time. This decrease in diameter was, however not necessarily leading to full blockage of the apertures. As was demonstrated by the multiple samples with which we managed to observe mass flows, some nanopores could be sufficiently stable to remain open for several months without any detectable changes to their dimensions.

These results prompted us to further investigate the parameters leading to stable nanopores. We used TEM imaging of nanopores as a means to measure the evolution of the dimensions for samples of different thickness, from various manufacturers and in different storage conditions. Specifically, we imaged nanopores ranging in diameter from 5 to 50 nm over several days and weeks. Figure A.2 shows a typical time-dependent structural relaxation in nanopores with initial diameters of (A) 25 nm and (B) 12 nm. The observed decrease in diameter was of 35% in (A), and in (B), I show a case where the blockage was effectively complete. Both of these samples were fabricated in a 50 nm thick SiN membrane under similar conditions. The TEM imaging shows a clear decrease in the nanopore diameter over a time scale of the order of $\mathcal{O}(10^2)$ hours.

As explained in the section on sample fabrication, it is a common practice to expose nanopores to a mid-range intensity of electron bombardment to induce

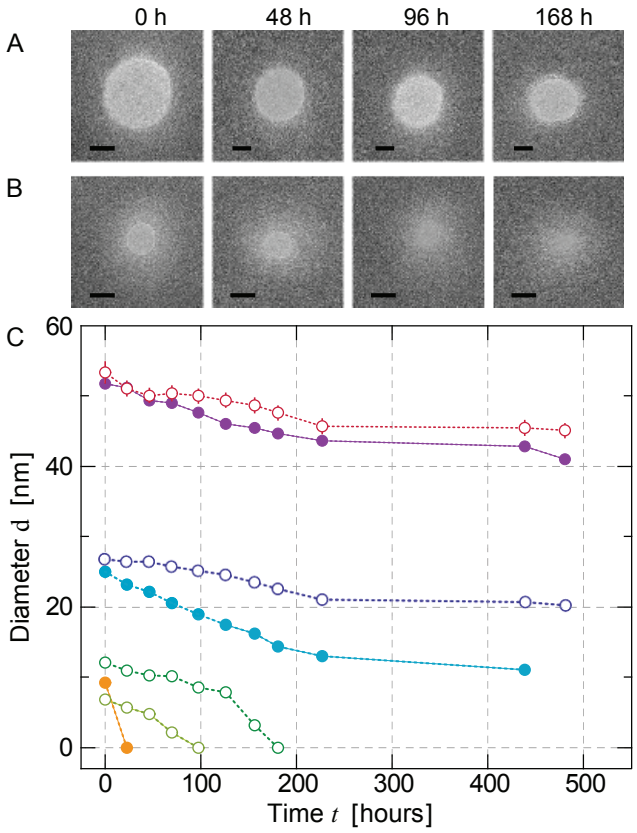

Fig. A.2 TEM images of a nanopore as a function of time. The nanopore diameter at fabrication was 25 nm in (A) and 12 nm in (B). The nanopores were drilled in 50 nm thick amorphous silicon nitride membranes and stored at 77 K between each imaging sessions. All scale bars are 10 nm long. (C):Diameter of several such nanopores as a function of time after fabrication. Open symbols are for samples stored at liquid nitrogen temperature and the filled symbols are for samples kept at room temperature. The symbols at zero diameter indicate nanopores that are completely blocked. The lines connecting the symbols are guides to the eye.

fluidization of the material around the pore and reshape them in the process. This is part of a normal drilling procedure. There is a legitimate question regarding the risk of affecting nanopores during imaging with the TEM. The decrease in diameter observed in figure A.2A,B could however not have been

caused by the exposure during imaging because the intensity of the electron beam required to image the pores was kept approximately 10 times lower than that required to reshape the surface. We specifically tested this hypothesis by exposing a 9 nm nanopore, for a total period of 40 minutes, to a beam intensity equivalent to that used during regular imaging of nanopores. No noticeable change in the dimensions of the pore were observed. The decrease in diameter observed in figure A.2 was thus caused by a slow structural relaxation of the amorphous silicon nitride independent of our measurements.

Figure A.2C shows the diameter of nanopores as a function of the time elapsed since their fabrication, for two distinct storage conditions. Specifically, we stored some wafers under vacuum at liquid nitrogen temperatures (open symbols) and others remained at room temperature (filled symbols). The samples at low temperature were only warmed up for the imaging sessions. All the nanopores shown in figure A.2C were fabricated in a 50 nm membrane, and the storage temperature is found to have a negative correlation with the rate of pore size decrease.

Two types of behavior are identifiable in the structural relaxation of the nanopores. The relaxation can either lead to a stable nanopore or a blocked one. The two distinct behaviors are easily distinguished in figure A.2C where the four higher datasets correspond to stable nanopores and the bottom ones show blocked pores. In order to characterize these two types of behavior, we fabricated several nanopores in membranes of different thickness between 10-100 nm. Figure A.3 shows the diameter of nanopores drilled originally with diameters between 25 and 50 nm and their time-dependence. These nanopores

were all opened, even after several hundred hours. The relaxation of these nanopores approaches an equilibrium point, and the dashed lines are fit to the data for a phenomenological equation with a simple exponential decay

$$d(t) = d_f + (d_0 - d_f)\left(\frac{\tau}{t}\right)\left(1 - e^{-\frac{t}{\tau}}\right),$$

where d_f is the final diameter, d_0 the initial diameter and τ a characteristic time. This equation can be used in the instances where the initial diameter is large enough that the nanopores approache a near steady-state equilibrium shape.

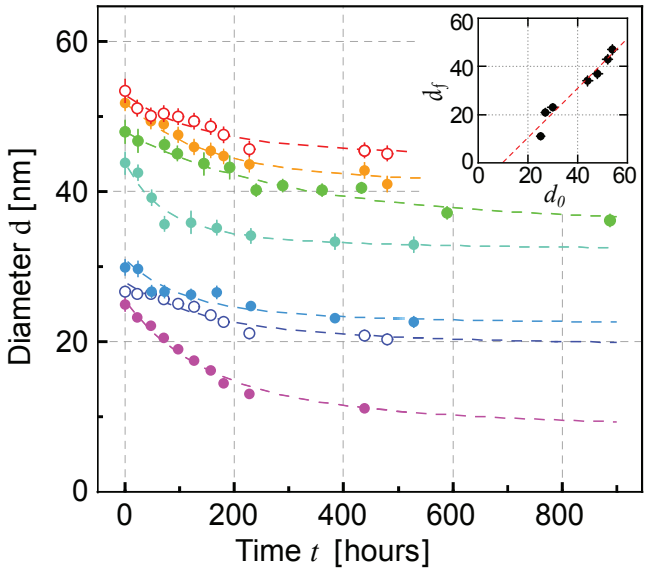

Fig. A.3 Diameter of nanopores as a function of the duration since fabrication. These nanopores asymptotically approach a near steady-state through a structural relaxation. The dashed lines are fit with an equation with a single exponential decay. The inset shows the final diameter as a function of the initial diameter immediately after drilling and linear fit through the data.

The characteristic time of relaxation was found to vary between ∼40-160

hours and this range was observed for pores of the same size drilled in membranes from different manufacturers, which suggests the process of amorphous silicon nitride deposition affects the structural stability of the nanopores. This also indicates the relaxation is closely linked to the microstructure of the material and how the electron beam exposure affected it during fabrication.

In practical terms, the final diameter of stable pores was found to depend nearly linearly on the initial pore size. The inset of figure A.3 shows the final diameter as a function of the initial one for several pores that reached an equilibrium shape.

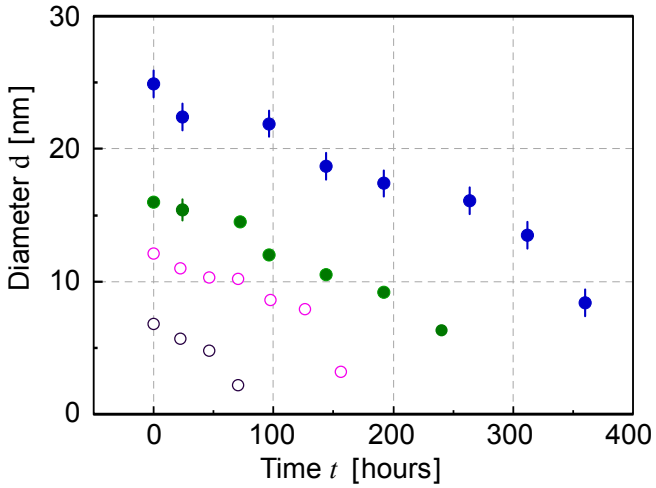

Fig. A.4 Diameter of nanopores as a function of the elapsed time from fabrication. The open symbols represent samples stored at low temperature, whereas the filled ones are for sample kept at room temperature.

As seen above in figure A.2C, the three smallest nanopores relaxed to a fully occluded state within the first 100 to 200 hours after fabrication. In these cases, the diameter has a distinctly different functional dependence on time. Figure A.4 shows the size of several nanopores <25 nm as a function of

time, exclusively for samples that eventually closed. Again the open symbols are for samples stored at 77 K and the filled symbols are for storage at room temperature. The length of the error bar through the dots shows the uncertainty on diameters measured from TEM images. The gradual and steady decrease in diameter for these samples was proportionally faster than in the case of larger pores.

A.3 Conditions for Stable Nanopore Fabrication

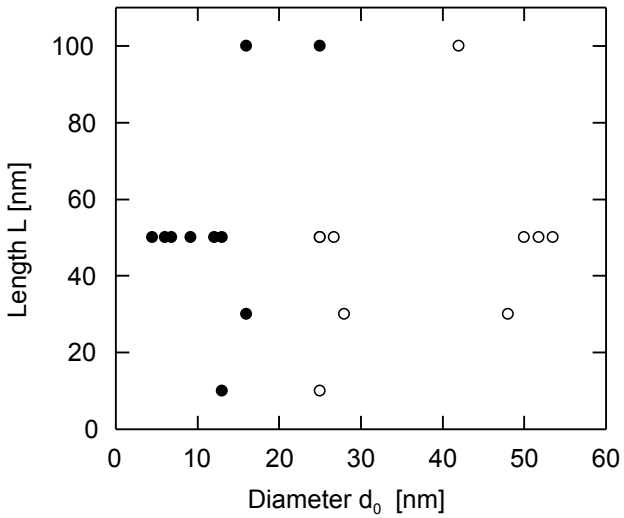

Fig. A.5 Phase diagram of the structural stability of nanopores as a function of the membrane thickness. The open symbols correspond to nanopores that remained open and the filled symbols correspond to nanopores that eventually became completely blocked.

From these results it became evident that the thickness of the membrane and the diameter of the nanopore could be used to determine a "boundary" across which the type of relaxation changed from a slow approach to an equilibrium, to a relatively fast shrinking of the aperture. We mapped the state

of several samples after hundreds of hours, and for several membrane thicknesses. Figure A.5 shows this phase diagram, where the open circles correspond to nanopores that remained open, and the filled ones to blocked nanopores.

This diagram shows the difficulty of keeping small nanopores open for extended periods of time. While we did not have many samples with thicknesses below 30 nm, we note that nanopores with initial dimensions between 15-20 nm are hard to keep open for extended periods of time. A corollary of this is that in order to make experiments with nanopores barely a few nanometers across, it is recommended that thinner membranes be used as substrates.

References

[1] Auslaender, O. M. *et al.*, Spin-charge separation and localization in one dimension, *Science* **308**, 88–92 (2005).

[2] Del Maestro, A., A Luttinger liquid core inside helium-4 filled nanopores, *Int. J. Mod. Phys. B* **26**, 1244002 (2012).

[3] Kulchytskyy, B., Gervais, G. & Del Maestro, A., Local superfluidity at the nanoscale, *Phys. Rev. B* **88**, 064512 (2013).

[4] Giamarchi, T., *Quantum physics in one dimension* (Clarendon ; Oxford University Press, Oxford; New York, 2004).

[5] Voit, J., One-dimensional Fermi liquids, *Rep. Prog. Phys.* **58**, 977 (1995).

[6] Tomonaga, S., Remarks on Bloch's method of sound waves applied to many-fermion problems, *Prog. Theor. Phys.* **5**, 544–569 (1950).

[7] Luttinger, J., An exactly soluble model of a many-fermion system, *J. Math. Phys.* **4**, 1154 (1963).

[8] Mattis, D. & Lieb, E., Exact solution of a many-fermion system and its associated boson field, *J. Math. Phys.* **6**, 304 (1965).

[9] Haldane, F., Luttinger liquid theory of one-dimensional quantum fluids: 1. properties of the Luttinger model and their extension to the general 1d interacting spinless fermi gas, *J. Phys. C - Solid State Phys.* **14**, 2585–2609 (1981).

[10] Cazalilla, M. A., Effect of suddenly turning on interactions in the Luttinger model, *Phys. Rev. Lett.* **97**, 156403 (2006).

[11] Cazalilla, M., Bosonizing one-dimensional cold atomic gases, *J. Phys. B* **37**, S1–S47 (2004).

[12] Cazalilla, M. A., Citro, R., Giamarchi, T., Orignac, E. & Rigol, M., One dimensional bosons: From condensed matter systems to ultracold gases, *Rev. Mod. Phys.* **83**, 1405–1466 (2011).

[13] Milliken, F., Umbach, C. & Webb, R., Indications of a Luttinger liquid in the fractional quantum Hall regime, *Solid State Commun.* **97**, 309–313 (1996).

[14] Chang, A., Pfeiffer, L. & West, K., Observation of chiral Luttinger behavior in electron tunneling into fractional quantum Hall edges, *Phys. Rev. Lett.* **77**, 2538–2541 (1996).

[15] Auslaender, O. *et al.*, Experimental evidence for resonant tunneling in a Luttinger liquid, *Phys. Rev. Lett.* **84**, 1764–1767 (2000).

[16] Auslaender, O. *et al.*, Tunneling spectroscopy of them elementary excitations in a one-dimensional wire, *Science* **295**, 825–828 (2002).

[17] Tserkovnyak, Y., Halperin, B., Auslaender, O. & Yacoby, A., Finite-size effects in tunneling between parallel quantum wires, *Phys. Rev. Lett.* **89**, 136805 (2002).

[18] Greiner, M., Bloch, I., Mandel, O., Hänsch, T. W. & Esslinger, T., Exploring Phase Coherence in a 2D Lattice of Bose-Einstein Condensates, *Phys. Rev. Lett.* **87**, 160405 (2001).

[19] Görlitz, A. *et al.*, Realization of Bose-Einstein Condensates in Lower Dimensions, *Phys. Rev. Lett.* **87**, 130402 (2001).

[20] Hansel, W., Hommelhoff, P., Hansch, T. & Reichel, J., Bose-Einstein condensation on a microelectronic chip, *Nature* **413**, 498–501 (2001).

[21] Schreck, F. *et al.*, Quasipure Bose-Einstein condensate immersed in a Fermi sea, *Phys. Rev. Lett.* **87**, 080403 (2001).

[22] Wada, N., Taniguchi, J., Ikegami, H., Inagaki, S. & Fukushima, Y., Helium-4 Bose fluids formed in one-dimensional 18 angstrom diameter pores, *Phys. Rev. Lett.* **86**, 4322–4325 (2001).

[23] Grayson, M., Tsui, D. C., Pfeiffer, L. N., West, K. W. & Chang, A. M., Continuum of chiral Luttinger liquids at the fractional quantum Hall edge, *Phys. Rev. Lett.* **80**, 1062–1065 (1998).

[24] Bockrath, M. *et al.*, Luttinger-liquid behaviour in carbon nanotubes, *Nature* **397**, 598–601 (1999).

[25] Ishii, H. *et al.*, Direct observation of Tomonaga-Luttinger-liquid state in carbon nanotubes at low temperatures, *Nature* **426**, 540–544 (2003).

[26] Laroche, D., Gervais, G., Lilly, M. P. & Reno, J. L., Positive and negative Coulomb drag in vertically integrated one-dimensional quantum wires, *Nat. Nano.* **6**, 793–797 (2011).

[27] Grayson, M., Tsui, D. C., Pfeiffer, L. N., West, K. W. & Chang, A. M., Resonant tunneling into a biased fractional quantum hall edge, *Phys. Rev. Lett.* **86**, 2645–2648 (2001).

[28] Yamamoto, M., Stopa, M., Tokura, Y., Hirayama, Y. & Tarucha, S., Negative Coulomb drag in a one-dimensional wire, *Science* **313**, 204–207 (2006).

[29] Laroche, D., Gervais, G., Lilly, M. P. & Reno, J. L., 1D-1D Coulomb drag signature of a Luttinger liquid, *Science* **343**, 631–634 (2014).

[30] Steinberg, H. *et al.*, Charge fractionalization in quantum wires, *Nat. Phys.* **4**, 116–119 (2008).

[31] Jompol, Y. *et al.*, Probing spin-charge separation in a Tomonaga-Luttinger liquid, *Science* **325**, 597–601 (2009).

[32] Laroche, D., *Coulomb Drag in Vertically-Integrated One-Dimensional Quantum Wires* (McGill University, Montreal, 2014).

[33] Kinoshita, T., Wenger, T. & Weiss, D., A quantum Newton's cradle, *Nature* **440**, 900–903 (2006).

[34] Paredes, B. *et al.*, Tonks-Girardeau gas of ultracold atoms in an optical lattice, *Nature* **429**, 277–281 (2004).

[35] Stoferle, T., Moritz, H., Schori, C., Kohl, M. & Esslinger, T., Transition from a strongly interacting 1D superfluid to a Mott insulator, *Phys. Rev. Lett.* **92**, 130403 (2004).

[36] Gunter, K., Stoferle, T., Moritz, H., Kohl, M. & Esslinger, T., p-Wave interactions in low-dimensional fermionic gases, *Phys. Rev. Lett.* **95**, 230401 (2005).

[37] Wada, N. & Cole, M. W., Low-Dimensional Helium Quantum Fluids Realized under Nano-Extreme Conditions, *J. Phys. Soc. Jpn.* **77**, 111012 (2008).

[38] Taniguchi, J., Aoki, Y. & Suzuki, M., Superfluidity of liquid He-4 confined to one-dimensional straight nanochannel structures, *Phys. Rev. B* **82**, 104509 (2010).

[39] Ikegami, H. *et al.*, Superfluidity of He-4 in nanosize channels, *Phys. Rev. B* **76**, 144503 (2007).

[40] Reppy, J. D., Superfluid-helium in porous-media, *J. Low Temp. Phys.* **87**, 205–245 (1992).

[41] Zassenhaus, G. M. & Reppy, J. D., Lambda point in the He-4-Vycor System: A test of hyperuniversality, *Phys. Rev. Lett.* **83**, 4800–4803 (1999).

[42] Yamamoto, K., Shibayama, Y. & Shirahama, K., Liquidsolid transition and phase diagram of 4he confined in nanoporous glass, *J. Phys. Soc. Jpn* **77**, 013601 (2008).

[43] Yoon, J., Sergatskov, D., Ma, J. A., Mulders, N. & Chan, M. H. W., Superfluid transition of He-4 in ultralight aerogel, *Phys. Rev. Lett.* **80**, 1461–1464 (1998).

[44] Toda, R. *et al.*, Superfluidity of He-4 in one and three dimensions realized in nanopores, *Phys. Rev. Lett.* **99**, 255301 (2007).

[45] Del Maestro, A., Boninsegni, M. & Affleck, I., He 4 Luttinger Liquid in Nanopores, *Phys. Rev. Lett.* **106**, 105303 (2011).

[46] Del Maestro, A. & Affleck, I., Interacting bosons in one dimension and the applicability of Luttinger-liquid theory as revealed by path-integral quantum Monte Carlo calculations, *Phys. Rev. B* **82**, 060515 (2010).

[47] Hirschfelder, J. O., *Molecular Theory of Gases and Liquids* (Wiley, New York, 1964).

[48] Lafferty, J. M., *Foundations of Vacuum Science and Technology* (Wiley, New York, 1998).

[49] Clausing, P., Flow of highly rarefied gases through tubes of arbitrary length, *Journal of Vacuum Science & Technology* **8**, 636 (1971).

[50] Berman, A., Free molecule transmission probabilities, *J. Appl. Phys.* **36**, 3356–3356 (1965).

[51] Cole, R., Transmission probability of free molecular flow through a tube, *Raref. Gas Dyn.* **I**, 261–72 (1977).

[52] Steckelmacher, W., The effect of cross-sectional shape on the molecular flow in long tubes, *Vacuum* **28**, 269 – 275 (1978).

[53] Iczkowski, R. P., Margrave, J. L. & Robinson, S. M., Effusion of gases through conical orifices, *J. Phys. Chem.* **67**, 229 (1963).

[54] Gomez-Goni, J. & Lobo, P., Comparison between Monte Carlo and analytical calculation of the conductance of cylindrical and conical tubes, *J. Vac. Sci. Technol. A* **21**, 1452–1457 (2003).

[55] Lobo, P., Becheri, F. & Gomez-Goni, J., Comparison between Monte Carlo and analytical calculation of Clausing functions of cylindrical and conical tubes, *Vacuum* **76**, 83–88 (2004).

[56] Langhaar, H. L., Steady flow in the transition length of a straight tube, *J. Appl. Mech.* **9**, A55–A58 (1942).

[57] Kapitza, P., Viscosity of liquid helium below the lambda-point, *Nature* **141**, 74 (1938).

[58] Keller, W., *Helium-3 and Helium-4.* The International cryogenics monograph series (Plenum Press, 1969).

[59] Tilley, D. & Tilley, J., *Superfluidity and Superconductivity.* Graduate Student Series in Physics (Taylor and Francis, 1990).

[60] Craig, P. P. & Pellam, J. R., Observation of perfect potential flow in superfluid, *Phys. Rev.* **108**, 1109–1112 (1957).

[61] Brooks, J. S. & Donnelly, R. J., Calculated thermodynamic properties of superfluid he-4, *J. Phys. and Chemical Reference Data* **6**, 51–104 (1977).

[62] Feynman, R. P., Atomic theory of the 2-fluid model of liquid helium, *Phys. Rev.* **94**, 262–277 (1954).

[63] Anderson, P. W., Considerations on the flow of superfluid helium, *Rev. Mod. Phys.* **38**, 298–310 (1966).

[64] Varoquaux, E., Critical velocities in superfluids and the nucleation of vortices, *C. Rend. Phys.* **7**, 1101–1120 (2006).

[65] Clow, J. R. & Reppy, J. D., Temperature dependence of superfluid critical velocities near tlambda, *Phys. Rev. Lett.* **19**, 291 (1967).

[66] Varoquaux, E., Meisel, M. W. & Avenel, O., Onset of the critical velocity regime in superfluid he-4 at low-temperature, *Phys. Rev. Lett.* **57**, 2291–2294 (1986).

[67] Steinhauer, J., Schwab, K., Mukharsky, Y., Davis, J. & Packard, R., Vortex nucleation in superfluid he-4, *Phys. Rev. Lett.* **74**, 5056–5059 (1995).

[68] Avenel, O., Bernard, M., Burkhart, S. & Varoquaux, E., Autopsy of superflow collapses and multiple phase slips, *Physica B* **210**, 215–233 (1995).

[69] Shifflett, G. M. & Hess, G. B., Intrinsic critical velocities in superfluid He-4 flow-through 12-mu-m diameter orifices near t-lambda - experiments on the effect of geometry, *J. Low Temp. Phys.* **98**, 591–629 (1995).

[70] Zimmermann Jr, W., The flow of superfluid 4He through submicron apertures: Phase slip and critical velocities due to quantum vortex motion, *Cont. Phys.* **37**, 219–234 (1996).

[71] Packard, R. E., The role of the Josephson-Anderson equation in superfluid helium, *Rev. Mod. Phys.* **70**, 641–651 (1998).

[72] Donnelly, R., *Quantized Vortices in Helium II.* No. v. 2 in Cambridge Studies in American Literature and Culture (Cambridge University Press, 1991).

[73] Krapf, D. *et al.*, Fabrication and characterization of nanopore-based electrodes with radii down to 2 nm, *Nano Lett.* **6**, 105–109 (2006).

[74] van den Hout, M. *et al.*, Controlling nanopore size, shape and stability, *Nanotechnology* **21**, 115304 (2010).

[75] Li, J., Gershow, M., Stein, D., Brandin, E. & Golovchenko, J., DNA molecules and configurations in a solid-state nanopore microscope, *Nature Mat.* **2**, 611–615 (2003).

[76] Branton, D. *et al.*, The potential and challenges of nanopore sequencing, *Nature Biotechnol.* **26**, 1146–1153 (2008).

[77] Timp, W. *et al.*, Nanopore sequencing: Electrical measurements of the code of life, *Ieee Trans. Nanotechnol.* **9**, 281–294 (2010).

[78] Li, J. *et al.*, Ion-beam sculpting at nanometre length scales, *Nature* **412**, 166–169 (2001).

[79] Storm, A. J., Chen, J. H., Ling, X. S., Zandbergen, H. W. & Dekker, C., Fabrication of solid-state nanopores with single-nanometre precision, *Nature Mat.* **2**, 537–540 (2003).

[80] Chang, H. *et al.*, Fabrication and characterization of solid-state nanopores using a field emission scanning electron microscope, *Appl. Phys. Lett.* **88**, 3 (2006).

[81] Vlassiouk, I., Apel, P. Y., Dmitriev, S. N., Healy, K. & Siwy, Z. S., Versatile ultrathin nanoporous silicon nitride membranes, *Proc. Nat. Acad. Sci.* **106**, 21039–21044 (2009).

[82] Dekker, C., Solid-state nanopores, *Nature Nano.* **2**, 209–215 (2007).

[83] Hinds, B. J. *et al.*, Aligned multiwalled carbon nanotube membranes, *Science* **303**, 62–65 (2004).

[84] Wu, M. Y. *et al.*, Control of shape and material composition of solid-state nanopores, *Nano Lett.* **9**, 479–484 (2009).

[85] Kim, M. J., McNally, B., Murata, K. & Meller, A., Characteristics of solid-state nanometre pores fabricated using a transmission electron microscope, *Nanotechnology* **18**, 205302 (2007).

[86] Prabhu, A. S. *et al.*, SEM-induced shrinking of solid-state nanopores for single molecule detection, *Nanotechnology* **22**, 425302 (2011).

[87] Wu, M. Y., Krapf, D., Zandbergen, M., Zandbergen, H. & Batson, P. E., Formation of nanopores in a SiN/SiO2 membrane with an electron beam, *Appl. Phys. Lett.* **87**, 113106 (2005).

[88] Kim, M., Wanunu, M., Bell, D. & Meller, A., Rapid fabrication of uniformly sized nanopores and nanopore arrays for parallel DNA analysis, *Adv. Mat.* **18**, 3149–3153 (2006).

[89] Gruener, S. & Huber, P., Knudsen diffusion in silicon nanochannels, *Phys. Rev. Lett.* **100**, 064502 (2008).

[90] Velasco, A. E., Friedman, S. G., Pevarnik, M., Siwy, Z. S. & Taborek, P., Pressure-driven flow through a single nanopore, *Phys. Rev. E* **86**, 025302 (2012).

[91] Savard, M., Tremblay-Darveau, C. & Gervais, G., Flow Conductance of a Single Nanohole, *Phys. Rev. Lett.* **103**, 104502 (2009).

[92] Beskok, A. & Karniadakis, G., A model for flows in channels, pipes, and ducts at micro and nano scales, *Microscale Thermophys. Eng.* **3**, 43–77 (1999).

[93] Unnikrishnan, S. *et al.*, Transition flow through an ultra-thin nanosieve, *Nanotechnology* **20**, 305304 (2009).

[94] White, G. & Meeson, P., *Experimental Techniques in Low-Temperature Physics: Fourth Edition*. Monographs on the Physics and Chemistry of Materials (OUP Oxford, 2002).

[95] Ventura, G. & Risegari, L., *The Art of Cryogenics: Low-Temperature Experimental Techniques* (Elsevier Science, 2010).

[96] Li, Q. *et al.*, Size evolution and surface characterization of solid-state nanopores in different aqueous solutions, *Nanoscale* **4**, 1572–1576 (2012).

[97] Savard, M., Dauphinais, G. & Gervais, G., Hydrodynamics of Superfluid Helium in a Single Nanohole, *Phys. Rev. Lett.* **107**, 254501 (2011).

[98] Goodwin, J., *Ph.D. Thesis*, Ph.D. thesis, University of Washington (1968).

[99] *NIST Standard Reference Data*, (http://webbook.nist.gov/chemistry/fluid/) edn. (2013).

[100] Zimmermann, W., Lindensmith, C. A. & Flaten, J. A., The interpretation of phase-slip and critical-velocity data from the flow of superfluid He-4 through a 2 mu m by 2 mu m aperture, *J. Low Temp. Phys.* **110**, 497–502 (1998).

[101] Lindensmith, C. A., *Critical Velocities and Vortices in Superfluid Helium-4 Flow Through a Small Aperture* (University of Minnesota, Minneapolis, 1996).

[102] Ihas, G. G., Avenel, O., Aarts, R., Salmelin, R. & Varoquaux, E., Quantum nucleation of vortices in the flow of superfluid He-4 through an orifice, *Phys. Rev. Lett.* **69**, 327–330 (1992).

[103] Davis, J. *et al.*, Evidence for quantum tunneling of phase-slip vortices in superfluid he-4, *Phys. Rev. Lett.* **69**, 323–326 (1992).

[104] Tsutsui, M., Taniguchi, M., Yokota, K. & Kawai, T., Identifying single nucleotides by tunnelling current, *Nat. Nano.* **5**, 286–290 (2010).

[105] Majumder, M., Chopra, N., Andrews, R. & Hinds, B. J., Nanoscale hydrodynamics: Enhanced flow in carbon nanotubes, *Nature* **438**, 44–44 (2005).

[106] Holt, J. K. *et al.*, Fast mass transport through sub-2-nanometer carbon nanotubes, *Science* **312**, 1034–1037 (2006).

[107] Verweij, H., Schillo, M. C. & Li, J., Fast mass transport through carbon nanotube membranes, *Small* **3**, 1996–2004 (2007).

[108] Majumder, M., Chopra, N. & Hinds, B. J., Mass transport through carbon nanotube membranes in three different regimes: ionic diffusion and gas and liquid flow, *ACS nano* **5**, 3867–3877 (2011).

[109] Norberg, P., Petersson, L. G. & Lundstrom, I., Characterization of gas-transport through micromachined submicron channels in silicon, *Vacuum* **45**, 139–144 (1994).

[110] Qin, X. C., Yuan, Q. Z., Zhao, Y. P., Xie, S. B. & Liu, Z. F., Measurement of the rate of water translocation through carbon nanotubes, *Nano Lett.* **11**, 2173–2177 (2011).

[111] Sawkey, D. & Harrison, J., Volume flow in liquid 3He in the Knudsen and Poiseuille regions, *Physica B* **329**, 112 – 113 (2003).